

**Utilization of FBRM in the Control of CSD  
in a Batch Cooled Crystallizer**

A thesis  
Presented to  
The academic faculty

By

Stéphanie Barthe

In partial fulfillment  
Of the Requirements for the Degree  
Master of Science in Chemical Engineering

Georgia Institute of Technology  
May, 2006

**UTILIZATION OF FBRM IN THE CONTROL OF CSD IN A BATCH COOLED  
CRYSTALLIZER**

Approved by:

Dr. Ronald W. Rousseau, Advisor  
School of Chemical & Biomolecular Engineering  
*Georgia Institute of Technology*

Dr. Aryn Teja  
School of Chemical & Biomolecular Engineering  
*Georgia Institute of Technology*

Dr. Martha Gallivan  
School of Chemical & Biomolecular Engineering  
*Georgia Institute of Technology*

Date Approved: May, 2006

## **ACKNOWLEDGEMENTS**

I first would like to acknowledge the importance of the funds provided through the Cecil J. "Pete" Silas Endowed Chair that allowed the completion of this research. I wish also to give my sincere thanks to my thesis advisor, Dr Ronald W. Rousseau, for his knowledge, his helpful advice and time he offered throughout this project. I am grateful to the committee members for all the useful suggestions and remarks made: Dr Aryn Teja, and Dr Martha Gallivan.

I also want to thank past and present members of this research group for their precious help, friendship and support: Hatem Alsyoury, Karsten Bartling, Cosmas Bayuadri, Krystle Chavez, George Dumont, Young-Soo Kim, Jennifer Luk, Jose Mendez del Rio, Laurent Nassif, Quinta Nwanosike and Apichit "Ov" Svang-Aryaskul.

I give my thanks to all the professors and staff I met at Georgia Tech for being so willingly helpful and sharing part of their knowledge with me.

And last but not least, I would like to express my thankfulness to all my friends and my family for their kindness and support. They shaped the person I am today.

## TABLE OF CONTENTS

ACKNOWLEDGEMENTS.....	iii
LIST OF TABLES.....	vii
LIST OF FIGURES.....	viii
NOMENCLATURE.....	xii
SUMMARY.....	xvii

### CHAPTERS

<b>I. INTRODUCTION.....</b>	<b>1</b>
1.1 Introduction.....	1
1.2 Objectives.....	2
<b>II. BACKGROUND.....</b>	<b>4</b>
2.1 Crystallization.....	4
2.2 Supersaturation and Metastable State.....	6
2.2.1 Supersaturation.....	6
2.2.2 Metastable Zone.....	7
2.2.3 Formation and Growth.....	8
2.3 Nucleation and growth kinetics.....	9
2.3.1 Nucleation.....	9
2.3.1.1 Primary Nucleation.....	10
2.3.1.2 Secondary Nucleation.....	11
2.3.2 Growth kinetics.....	12
2.4 Technique of Measurement: FBRM.....	13
2.4.1 Principle.....	13
2.4.2 Data collected: CLD.....	14
2.4.3 Relationship between CSD and CLD.....	14
2.5 Fines Removal.....	15
2.6 Chemicals used: Paracetamol/Ethanol.....	16

2.7	Population balance.....	18
2.8	Solubility data.....	19
<b>III.</b>	<b>METHODOLOGY.....</b>	<b>21</b>
3.1	Experimental design.....	21
3.2	Procedures.....	25
3.2.1	FBRM experiments.....	25
3.2.2	Washing & drying of paracetamol crystals.....	26
3.2.3	Sieving.....	27
3.2.4	Observation of the crystals.....	28
3.3	Solution used.....	29
3.4	Conversion of CLD to CSD.....	29
<b>IV.</b>	<b>MODEL.....</b>	<b>31</b>
4.1	Relationship between CLD and CSD.....	31
4.1.1.	General description of the procedure.....	32
4.1.2.	Step by step description of the process.....	37
4.2	Restoration of the CSD.....	55
<b>V.</b>	<b>RESULTS .....</b>	<b>60</b>
5.1	No fines removal.....	60
5.1.1	Cooling Rate -0.10 <sup>0</sup> C/min.....	48
5.1.2	Cooling Rate -0.20 <sup>0</sup> C/min .....	55
5.1.3	Cooling Rate -0.35 <sup>0</sup> C/min.....	62
5.1.4	Cooling Rate -0.50 <sup>0</sup> C/min.....	69
5.2	Fines removal.....	77
5.2.1	Cooling Rate - 0.10 <sup>0</sup> C/min.....	77
5.2.2	Cooling Rate - 0.20 <sup>0</sup> C/min.....	81
5.2.3	Cooling Rate - 0.35 <sup>0</sup> C/min.....	85
5.2.4	Cooling Rate - 0.50 <sup>0</sup> C/min.....	89
5.3	Analysis of the product.....	93
<b>VI.</b>	<b>DISCUSSION.....</b>	<b>101</b>
<b>VII.</b>	<b>CONCLUSION .....</b>	<b>106</b>

**APPENDICES**

**A. CALIBRATION CURVE OF THE MINI PERISTALTIC METERING PUMP....108**  
**B. IMPLEMENTATION OF THE FINES REMOVAL SYSTEM .....109**  
**C. PROGRAM USED TO RESTORE THE CSD.....111**

**REFERENCES.....116**

## LIST OF TABLES

Table 3.1	Experiments realized.....	25
Table 5.1	Sieving results from runs with a cooling rate of $-0.10$ °C/min without fines removal .....	62
Table 5.2	Sieving results from runs with a cooling rate of $-0.20$ °C/min without fines removal.....	67
Table 5.2	Sieving results from runs with a cooling rate of $-0.35$ °C/min without fines removal .....	71
Table 5.3	Sieving results from runs with a cooling rate of $-0.50$ °C/min without fines removal .....	75
Table 5.4	Sieving results from runs with a cooling rate of $-0.10$ °C/min with fines removal .....	79
Table 5.6	Sieving results from runs with a cooling rate of $-0.20$ °C/min with fines removal.....	83
Table 5.7	Sieving results from runs with a cooling rate of $-0.35$ °C/min with fines removal.....	87
Table 5.8	Sieving results from runs with a cooling rate of $-0.50$ °C/min with fines removal.....	91
Table 6.1	Summary of the results.....	84

## LIST OF FIGURES

Figure 2.1	Different Type of Faces .....	6
Figure 2.2	Example of a possible evolution of the crystallization, X-axis: Temperature; Y-axis: Concentration.....	8
Figure 2.3	Free Energy & Nucleation .....	11
Figure 2.4	Tip of the Lasentec probe and schematic drawing of the chords scanned. .....	13
Figure 2.5	Orthorhombic lattice.....	17
Figure 2.6	Monoclinic lattice.....	17
Figure 2.7	Solubility of Paracetamol in Ethanol (prediction of the model).....	20
Figure 3.1	Schematic diagram of the experimental apparatus .....	22
Figure 3.2	Chord Length Distribution, Paracetamol-Ethanol, Cooling rate $-0.10$ $^{\circ}\text{C}/\text{min}$ (end of the run) .....	24
Figure 3.3	Filtration of the Solution .....	26
Figure 3.4	Ro-Tap .....	27
Figure 3.5	Picture of a Crystal of Paracetamol – Octahedral Shape .....	29
Figure 3.6	Scheme of the computation of the matrix .....	29
Figure 4.1	Masking and Shadowing effect.....	34
Figure 4.2	Discretization of the population density.....	36
Figure 4.3	Representation of an octahedron in 3D space .....	38
Figure 4.4	Rotation of an object by an angle $\alpha$ and around the x-axis .....	40
Figure 4.5	Chord length measured by FBRM .....	43

Figure 4.6	On the left, various possible orientations of the particle -- On the right, what is measured by the FBRM (orthogonal 2D-projection of the particles located on the left). The laser beam is normal to the plane constituted by the paper. ....	43
Figure 4.7	Projection of a 2D shape onto the x-y plane from a 3D object in a specific orientation.....	44
Figure 4.8	Projection on the x-z plane .....	45
Figure 4.9	Computation of the CLD for a random orientation projected on the plane .....	47
Figure 4.10	Influence of the size of the particle.....	48
Figure 4.11	Height of particle for different orientations.....	49
Figure 4.12	Probable CLD $-q_{p,d}(s,L=630)$ - for an octahedron such as $L=630 \mu\text{m}$ .....	50
Figure 4.13.	Chord length distribution $q_{p,d}(s, L)$ for a sphere of diameter $L=200 \mu\text{m}$ ..	51
Figure 4.14	Population considered in the example, $n_d(L)$ .....	52
Figure 4.15	$q_{p,d}(s,L)$ for a single particle of dimension $10 \mu\text{m}$ and of dimension $100 \mu\text{m}$ .....	53
Figure 4.16	CLD - $q_d(s)$ - for the population of octahedron considered in the example .....	54
Figure 4.17	Comparison, initial population and CSD, $n_d(L)$ restored according to the procedure described in this chapter .....	58
Figure 4.18	Comparison between recalculated CLD and initial CLD.....	59
Figure 5.2	Evolution of the chord counts and the temperature for a cooling rate of $-0.10 \text{ }^\circ\text{C/min}$ without fines removal .....	61
Figure 5.2	Sieving data from runs 1.1, 1.2 and 1.3 for a cooling rate of $-0.10 \text{ }^\circ\text{C/min}$ , without fines removal.....	63
Figure 5.3	Restored and Experimental distribution for a cooling rate $-0.10 \text{ }^\circ\text{C/min}$ , without fines removal .....	64
Figure 5.4	Experimental and restored normalized chord length distributions for a cooling rate of $-0.10 \text{ }^\circ\text{C/min}$ , without fines removal .....	65

Figure 5.5	Evolution of the chord counts and the temperature for a cooling rate of – 0.20 °C/min without fines removal .....	66
Figure 5.6	Sieving data from runs 2.1, 2.2 and 2.3 for a cooling rate of – 0.20 °C/min, without fines removal .....	68
Figure 5.7	Restored and Experimental distribution for a cooling rate – 0.20 °C/min, without fines removal .....	69
Figure 5.8	Evolution of the chord counts and the temperature for a cooling rate of – 0.35 °C/min without fines removal .....	70
Figure 5.9	Sieving data from runs 3.1, 3.2 and 3.3 for a cooling rate of – 0.35 °C/min, without fines removal .....	72
Figure 5.10	Restored and Experimental distribution for a cooling rate – 0.35 °C/min, without fines removal .....	73
Figure 5.11	Evolution of the chord counts and the temperature for a cooling rate of – 0.50 °C/min without fines removal .....	74
Figure 5.12	Sieving data from runs 4.1, 4.2 and 4.3 for a cooling rate of – 0.50 °C/min, without fines removal .....	76
Figure 5.13	Restored and Experimental distribution for a cooling rate – 0.50 °C/min, without fines removal .....	77
Figure 5.14	Evolution of the chord counts and the temperature for a cooling rate of – 0.10 °C/min with fines removal .....	78
Figure 5.15	Sieving data from runs 1.4, 1.5 and 1.6 for a cooling rate of – 0.10 °C/min, with fines removal .....	80
Figure 5.16	Restored and Experimental distribution for a cooling rate – 0.10 °C/min, with fines removal .....	81
Figure 5.17	Evolution of the chord counts and the temperature for a cooling rate of – 0.20 °C/min with fines removal .....	82
Figure 5.18	Sieving data from runs 2.4, 2.5 and 2.6 for a cooling rate of – 0.20 °C/min, with fines removal .....	84

Figure 5.19	Restored and Experimental distribution for a cooling rate – 0.20 °C/min, with fines removal .....	85
Figure 5.20	Evolution of the chord counts and the temperature for a cooling rate of – 0.35 °C/min with fines removal .....	86
Figure 5.21	Sieving data from runs 3.4, 3.5 and 3.6 for a cooling rate of – 0.35 °C/min, with fines removal .....	88
Figure 5.22	Restored and Experimental distribution for a cooling rate – 0.35 °C/min, with fines removal .....	89
Figure 5.23	Evolution of the chord counts and the temperature for a cooling rate of – 0.50 °C/min with fines removal .....	90
Figure 5.24	Sieving data from runs 4.4, 4.5 and 4.6 for a cooling rate of – 0.50 °C/min, with fines removal .....	92
Figure 5.25	Restored and Experimental distribution for a cooling rate – 0.50 °C/min, with fines removal .....	93
Figure 5.26	X-ray diffraction, experimental result .....	94
Figure 5.27	Powder diffraction pattern obtained for paracetamol trihydrate (upper plot) compared with the one of monoclinic paracetamol (lower plot) (Journal of pharmaceutical sciences, vol 91, no 5, may 2002) .....	95
Figure 5.28	IR spectroscopy, experimental spectrum, KBr disc .....	97
Figure 5.29	IR spectroscopy, theoretical spectrum, KBr disc (NIST Webbook) .....	98
Figure 5.30	Microscope pictures of paracetamol crystals (*4) .....	99
Figure 5.31	Zoom on a paracetamol crystal (*10) .....	100
Figure 6.1	Sieve analyses of product size distributions at two cooling rates and no fines removal .....	102
Figure 6.2	Evolution of the mean and the width in function of the condition of operations.....	104
Figure A.1	Calibration curve of the mini peristaltic pump .....	108
Figure B.1	Modelization of the trap .....	109

## NOMENCLATURE

$A$	crystalline area [ $\text{m}^2$ ]
$\mathcal{A}$	conversion matrix
$a, b, c$	lengths of the unit cell [m]
$a_i$	activity coefficient
$B$	matrix
$B^\circ$	secondary nucleation [crystals/ $\text{m}^3$ ]
$C$	concentration [mol/L]
$C^*$	concentration at saturation [mol/L]
CLD	chord length distribution
CLSM	constrained least square minimization
CSD	crystal size distribution
DDO	double draw off crystallizer
$D_i$	diameter of the impeller [m]
$E$	energy [J/mol]
$E_a$	activation energy [J/mol]
$F$	flat face
FBRM	focused beam reflectance measurement
$g$	order of the growth kinetic
$G$	growth rate [ $\text{m}\cdot\text{s}^{-1}$ ]
$G_0$	growth kinetic constant [ $\text{m}\cdot\text{s}^{-1}$ ]

$G_{12}, G_{21}$	coefficients NRTL model
$G_f$	Gibbs energy [J/mol]
$h$	height [m]
$J$	frequency of nucleation [ $m^{-3}.s^{-1}$ ]
$J_n$	rate of nucleation [ $kg.s^{-1}$ ]
$k$	coefficient
$K$	kinked face
$k_g$	growth kinetic constant
$k_n$	nucleation kinetic constant
$k_v$	volumetric shape factor
$L_{ave}$	average length [m]
$L_f$	limit size of fines removal [m]
$L$	crystal size [m]
$M$	inverse of rotation matrix R
MC	Monte-Carlo Simulation
$m_j$	$j^{th}$ moment of the distribution
$M_i$	mass of compound i [g]
$N$	number of iteration
$n^o$	nuclei population density
$n(L)$	population density
$n_d(L)$	discrete normalized counts per bin
$N_{Re}$	Reynolds number
$N_s$	speed of impeller [rpm]

$Q(L)$	flow rate of the fine removal [ $\text{m}^3 \cdot \text{s}^{-1}$ ]
$q(s)$	chord length density
$q_d(s, L)$	normalized discrete chord counts per bin for a single particle of size L
$q_d(s)$	normalized discrete chord counts per bin
$R$	gas constant
$r_c$	critical nuclei size [m]
$R_g$	massic growth rate [ $\text{kg} \cdot \text{m}^{-2} \cdot \text{s}^{-1}$ ]
$R_{x,y,z}$	Rotation matrix
$S$	entropy [ $\text{J} \cdot \text{mol}^{-1} \cdot ^\circ\text{C}^{-1}$ ]
$S_f$	stepped face
$S_u$	supersaturation ratio
$T$	temperature [ $^\circ\text{C}$ ]
$t$	time [s]
$T_m$	melting point [ $^\circ\text{C}$ ]
$V_s$	volume of the slurry [L]
$w$	weight fraction
$x$	molar fraction
$x, y, z$	coordinates
$X, Y, Z$	rotation matrices
$x', y', z'$	coordinates after rotation
$\Delta C_{\max}$	maximum $\Delta C$ measured for a given T
$\Delta g_{12}, \Delta g_{21}$	NRTL constants
$\Delta G_c$	critical free enthalpy [J/mol]

$\Delta L$	variation in size [m]
$\Delta M$	mass of crystal retained by each sieve [g]
$\Delta_m h$	heat of fusion [J/mol]

### ***Greek symbols***

$\alpha, \beta, \gamma$	Rotation angles [rad]
$\alpha_0$	coefficient
$\alpha_v$	volumetric shape factor
$\beta_s$	surface shape factor
$\gamma_0$	coefficient
$\gamma_c$	interfacial energy crystal-solution [J/mol]
$\Delta\chi = \chi_s - \chi_c$	difference in chemical potential
$\chi_0$	standard potential
$\chi_c$	chemical potential in the crystal
$\chi_s$	chemical potential in solution
$\mu$	viscosity [P]
$\Phi$	driving force
$\varphi, \psi, \theta$	Euler's angle [rad]
$\alpha_n$	constant NRTL
$\lambda$	parameter
$\rho$	density [g.cm <sup>3</sup> ]

$\sigma^-$	Width of the distribution [m]
$\sigma_s$	Relative supersaturation
$\tau_{12}, \tau_{21}$	Constant for NRTL model

### **Superscripts**

Ave	average
Nuc	nucleation
*, Sat	saturation

## SUMMARY

Controlling crystal size distribution (CSD) is important to downstream processing and to product quality. It is well-recognized that selective removal of segments of the crystal population can be used to influence CSD, for example by manufacturing a product with a larger dominant size or narrower distribution. Early work on the use of feedback control to manipulate the residence time distribution functions of fines in a continuous crystallizer demonstrated the utility of such an approach in handling process upsets or in reducing cycling that resulted from system instabilities. These efforts were extended to batch crystallization, although there remained significant difficulty associated with on-line analysis of the size distribution.

The development of new technologies, such as Focused Beam Reflectance Measurement (FBRM), provides a methodology for on-line monitoring of a representation of the CSD in either batch or continuous systems. Properly installed, the FBRM allows on-line determination of the chord length distribution (CLD), which is statistically related to the CSD and depends on the geometry of the crystal.

In the present work, we develop a statistical relationship between chord-length measurements and CSDs. The approach has been implemented for the batch cooling crystallization of paracetamol from solutions in ethanol. In supporting experiments, the FBRM has been used to monitor the evolution of CLDs, which were then used to estimate the CSDs of the corresponding crystal populations. The results demonstrate how the selective dissolution of fine particles and how the variation of the cooling rates

influences the size distribution of the crystalline products and they lay the foundation for implementation of methodologies that moves the CSD in preferred directions.

# CHAPTER I

## INTRODUCTION

### 1.1 Introduction

Crystallization is used widely in the production of pharmaceutical and many other specialty chemicals where it is often a key step in product recovery and / or purification. Control of this operation is essential as it determines the purity, crystal size distribution (CSD), morphology, and yield of the product. The CSD is a key factor in the design and operating conditions of downstream processes, and it also has a large influence on product characteristics and quality (Fachaux 1995).

It is well recognized that selective removal functions can be used to influence CSD, for example by producing a product with a larger dominant size or narrower distribution. Early work on the use of feedback control to manipulate the residence time distribution functions of fines in a continuous crystallizer demonstrated the utility of such an approach in handling process upsets and cycling that resulted from system instability (Rousseau & Howell 1982). These efforts were extended to batch crystallization, although there remained significant difficulty associated with on-line analysis of the size distribution (Cerreta 2000).

The development of new Process Analytical Technologies (PAT), such as Focused Beam Reflectance Measurement (FBRM), provides a methodology for on-line monitoring of a representation of the crystal population in either batch or continuous crystallization systems (Verbraeken 2001, Wood-Kaczmar 2001). The FBRM

technology is based on laser light scattering; properly installed, it allows on-line determination of the chord length distribution (CLD), which is statistically related to the CSD and also depends on the geometry of the crystal (Ruf 2000, Shi 2002, Li 2005). Several publications deal with the relationship between CSD and CLD, more particularly the recovery of the CSD from the CLD (Ruf 2000, Li 2005, and Shi 2002). For the FBRM technology to be used quantitatively, the geometry of the crystal must be well known and a 3D model of the crystal needs to be established in order to implement the time-consuming calculations.

The purpose of the present study was to use FBRM to monitor the evolution of CSD characteristics produced in a cooling batch crystallizer. Cooling batch crystallization of paracetamol from ethanol solutions was chosen as the model system. The work showed how fines removal and varying cooling rates provided reliable and practical control of the crystal size distribution.

## **1.2 Objectives**

The control of batch cooling crystallization is not trouble-free, and models of such a process can be complex when compared to the models applied to plug flow reactors and seeded crystallizations. The quality of the product generated by crystallization is linked to cost, flow, and downstream processes (Fachaux 1995). The point is to observe how some key and easily reachable factors, such as the cooling rate and the presence of a fines removal system, influence the characteristics of the crystalline matter produced. Such knowledge would facilitate a better control of the CSD, and in particular the mean size, and the width of the distribution. The main goal is to describe how simply by acting in a precise and pre-determined manner on the cooling rate and/or the fine removal flow one can directly affect these characteristics, thus manipulating the CSD at will.

Knowledge of the crystal population density function is especially useful as it is easily related to the mass density function, which gives direct and valuable information on the product. It is this distribution that is most often taken as a measure of crystal quality for industrial products. Thus this knowledge is precious when it comes to the control of the crystallization process.

In the present work, the evolution of the crystal population is monitored with an FBRM probe carefully positioned in the slurry. The main data recorded is the evolution of the CLD over time. This distribution results from the measurement of thousands of chord lengths per second. Considering that the CSD is more commonly used and, as described above gives direct information on crystal quality, it is essential to build up an efficient model for the restoration of the CSD from the CLD. The model presented by M. Mazzotti provides a valuable guideline but few details on this method are available in the literature (Ruf 2000). Most of the available publications (Li 2005, Worlitschek 2003, Shi 2002, Ruf 2000 and Jones 1984) focus on the restoration of the CSD for particles possessing a sphere like geometry, leaving the process obscure for systems possessing different and more complex geometric shapes. The present study proposes a similar and fully described general model to explain and illustrate the process of the computation of the CSD from the CLD. Due to the statistical nature of the relationship between the CSD and the CLD, a Monte-Carlo method is used as the simulation algorithm.

## CHAPTER II

### BACKGROUND

Useful information about the major concepts and theories associated with this research, such as crystallization principles and FBRM measurements, are developed in this chapter.

#### **2.1 Crystallization**

Crystallization is one of the oldest and most important solid-liquid separation techniques. It is the process of formation of crystalline matter from a homogeneous solution, for example crystallization of salt from evaporation of seawater. Crystallization processes are widely used in industry as a purification or a separation technique. This operation constitutes a fundamental step in the production of a wide range of chemicals as it often relates to the quality of the product, and also influences all the subsequent processes. Therefore, there are great potential benefits to controlling this crucial operation.

Crystallization occurs via diverse mechanisms; those most common in industry are cooling, evaporation, 'drowning out' (addition of an anti-solvent), chemical reaction (generation of solute), vacuum (cooling, flashing evaporation), crystallization from melts, vapors or solutions. This research principally focuses on cooling batch crystallization from clear solutions.

There are two main approaches to crystallization:

- 1- Physical: the physicochemical transformation of a pure compound whose state (gas  $\rightarrow$  liquid  $\rightarrow$  solid) is modified until there is formation of a crystalline

solid. For example, the solidification of gold (liquid at 2000<sup>0</sup>C, solidifies by cooling around 1064.2<sup>0</sup>C). The initial state can be solid (rearrangement of the atoms/molecules), liquid (solidification) or gas.

- 2- Chemical: dissolution of a solute, modification of the condition until supersaturation is reached and provocation of the nucleation/growth (crystallization of salt from sea water). The super-saturation and the metastable zone width are essential to this type of crystallization. These concepts will be detailed further in this chapter.

Cooling crystallization of paracetamol from ethanol solutions is used as the model system in the present study. The cooling process of such a solution, which is not a pure compound, is thus considered to be a chemical crystallization.

In general, crystal growth is based on both physical principles that allow crystallization, and physicochemical conditions, for example the temperature, that determine the development of the crystals. The growth of the crystal is a physical process; the molecules are arranged according to one of the classic Bravais Lattices. They are defined as the arrangement of the atoms in the whole space of a crystalline structure; there are 5 distinct Bravais lattices in 2D, while there are 14 in 3D (Artoli et al. 2002, and McPherson 2002).

The key repeating constituent in a crystal is the unit cell, which determines all the properties of a crystal. The unit cells repeat themselves in the three dimensions of space to form the crystal lattice, which is a regular arrangement of the atoms or molecules within a crystal.

There are three different types of face for a crystal: F (flat face), S<sub>f</sub> (stepped face) and K (kinked face). The mechanism and the rate of growth depend on the face in which it occurs (Growth rate on face K > rate on face S<sub>f</sub> > rate on face F). The morphology of a growing crystal is determined by the slowest growing crystallographic surfaces.

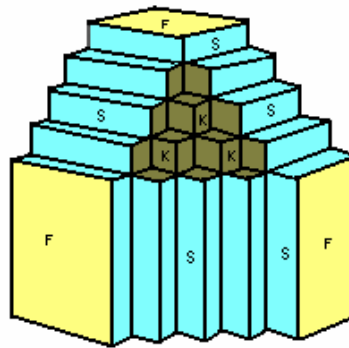


**Figure 2.1. Different Type of Faces**

We will here focus on the cooling crystallization of saturated solution. This kind of crystallization as we previously saw is based on the supersaturation and the metastable zone width.

## **2.2 Supersaturation and Metastable State**

### **2.2.1. Supersaturation**

When the amount of solute dissolved in solution exceeds the amount that the solvent is capable of sustaining, the solution is said to be supersaturated. Crystallization kinetic is a function of the supersaturation of the solution. The absolute supersaturation  $S_u$  (also called the supersaturation ratio) is linked to the driving force  $\phi$  of the process. It is a function of the concentration  $C$  of the compound of interest in the solution, as well as its concentration at equilibrium  $C^*$  which depends on temperature (Mullin 2001).

$$\Delta C = C - C^* \quad (2.1)$$

$$S_u = C / C^* \quad (2.2)$$

The fundamental driving force  $\phi$  is the difference between chemical potentials of the given substance in solution  $\chi_s$  and in the crystal  $\chi_c$  and can be expressed in terms of relative supersaturation  $\sigma$  (Mullin 2001):

$$\Delta\chi = \chi_s - \chi_c \quad (2.3)$$

$$\sigma_s = \frac{\Delta C}{C^*} = S_u - 1 \quad (2.4)$$

The chemical potential is expressed as a function of the activity  $a_i$  and of the standard potential  $\chi_0$ .

$$\chi = \chi_0 + RT \ln(a_i) \quad (2.5)$$

so for non-electrolyte solutions (no ions formed in solution) we have:

$$\frac{\Delta\chi}{RT} = \ln S_u = \ln(1 + \sigma_s) \quad (2.6)$$

Forming a supersaturated solution is a preliminary step to nucleation and growth of crystals.

### 2.2.2. Metastable Zone

Crystal growth is based on the existence of a metastable region when the supersaturation is reached and where spontaneous formation of nuclei is impossible, thus only growth takes place. This zone can be experimentally determined. It is a function of the nucleation temperature, the concentration of the solution and the cooling rate. The width of the metastable zone is basically the difference between the saturation and the nucleation temperature (see Figure 2.2). The FBRM allows a reliable on-line measure of both the metastable zone width and the solubility for a given solution (*Liotta 2001*).

The metastable zone width increases as the cooling rate increases and so solute concentration decreases. The interdependence of the metastable zone width and the

cooling rate, among other factors, was investigated by Nývlt (Nývlt 1971). Models have been established to predict the evolution of the width with temperature for example Kashchiev developed a relationship between the critical supersaturation ratio and the temperature of the solution (Kashchiev 2000).

### 2.2.3. Formation and Growth

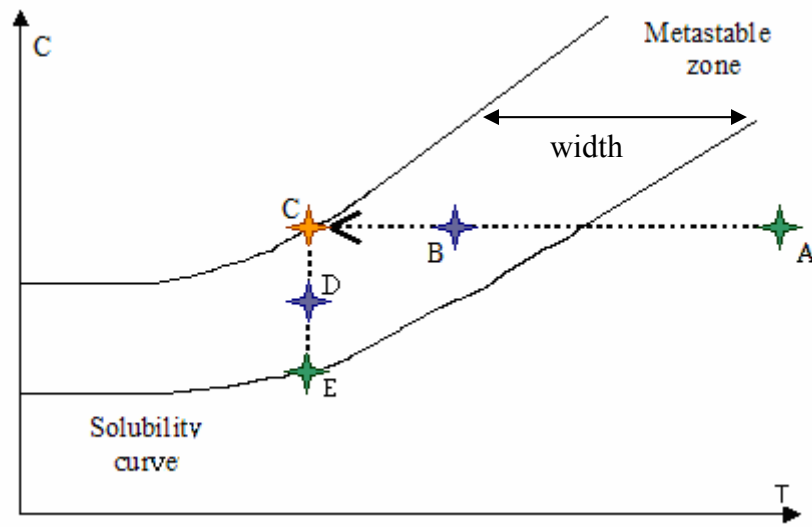


**Figure 2.2. Example of a possible evolution of the crystallization, X-axis: Temperature; Y-axis: Concentration**

Figure 2.2 shows an example of a solubility curve and a metastable zone. An unsaturated solution A, via cooling, goes through the solubility limit to become a supersaturated solution B. This solution is within the metastable zone, thus no primary nucleation is occurring. If the solution is cooled past the metastable zone limit, at C, nucleation occurs. After nucleation, the concentration is lowered by crystal growth,

perhaps to point D. Since this point is within the metastable zone, growth of the nuclei formed will occur until the solubility curve is reached at point E and equilibrium is reached.

If the cooling rate is high, the solution A is taken very fast to C, which is located past its metastable limit, and, in this case, an uncontrolled crystallization will occur, thus favoring the generation of fines, which are in many cases, undesired in the final product. A constant supersaturation generates a narrower size distribution, which is often looked for. Seeding within the metastable zone is commonly done in order to insure a constant supersaturation and a better-controlled crystallization.

The experimental conditions of the crystallization thus influence the population distribution. The Crystal Size Distribution (CSD) characterizes the amount of crystals of a given size at a given time; it gives precise and useful information of the crystal population. Knowledge of the CSD is a major tool in the characterization of a crystallization product, and this distribution has a major influence on most of downstream processes, as well as the quality of the final product.

## **2.3 Nucleation and Growth Kinetics**

### **2.3.1 Nucleation**

Crystallization can be divided into primary and secondary nucleation. Simply defined, primary nucleation is the formation of a new crystal without the involvement of existing crystals. Secondary nucleation requires existing crystals to participate in the nucleation mechanism. It often dominates primary nucleation in continuous crystallizers and seeded batch crystallization.

Nucleation is the main topic of several publications (Georgevia 2003 and Gerstlauer 2002). The condition of supersaturation alone is not enough to cause the system to

crystallize. Nucleation might occur spontaneously or it can also be induced artificially. Many parameters influence the system behavior, such as agitation, mechanical shock, friction or pressure. Industrially, nucleation usually occurs by a mechanism of secondary nucleation or heterogeneous primary nucleation.

Seeded crystallization is also widely used in industry. It offers easier modeling and better control. In such systems, nucleation may be neglected and only the growth of the seeds taken into account.

### 2.3.1.1 Primary Nucleation

Primary nucleation is defined as occurring from a clear solution, which means that the system does not contain crystalline matter before the event. This type of nucleation can be classified as homogeneous (crystallization occurs spontaneously) or as heterogeneous (crystallization is induced by foreign particles or impurities already present or introduced in the system).

Nucleation lowers the Gibbs energy ( $G_f$ ) and the entropy (S), where the solid is an ordered state of matter (lowest S). As shown in the Figure 2.3, the free energy is decreasing after nucleation; the crystallized compound has lower energy than the solute in solution. Information on the nucleation can be obtained by calculating either the frequency of nucleation (equation 2.7) or the rate of nucleation (equation 2.8). The main difference being the variables used to express J or  $J_n$  (Temperature or Supersaturation) and the units in which they are stated.

$$\text{Frequency of nucleation (m}^{-3}\cdot\text{s}^{-1}\text{)} \quad J = k_n \exp\left(-\frac{\Delta G_c}{RT}\right) \quad (2.7)$$

$$\text{Rate of nucleation (kg}\cdot\text{s}^{-1}\text{)} \quad J_n = \frac{dM}{dt} = k_n \Delta C_{\max}^n \quad (2.8)$$

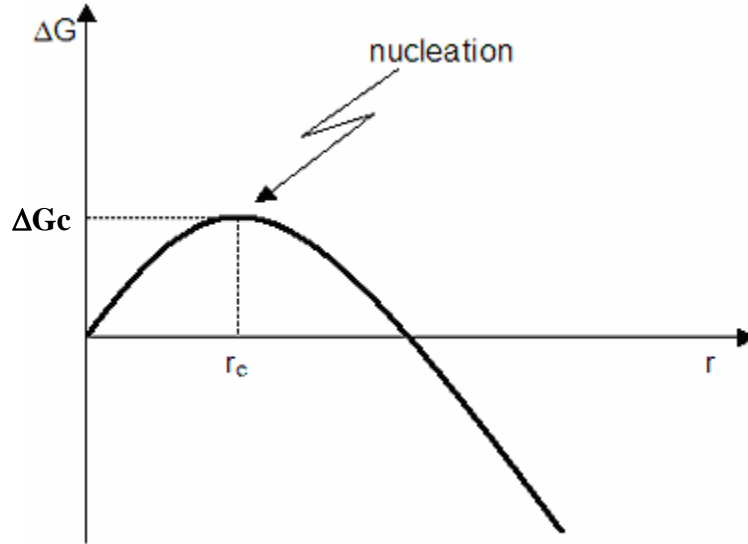


**Figure 2.3. Free Energy and Nucleation**

The value  $\Delta G_{critical}$  can be expressed as (Mullin 2001):

$$\Delta G_{critical} = \frac{4}{3} \pi \gamma_c r_c^2 \quad (2.9)$$

Once the critical nuclei size  $r_c$  is reached, nucleation occurs, thus the Gibbs energy decreases as the crystal grows. The nuclei becomes stable at  $r_c$

### 2.3.1.2 Secondary Nucleation

Nucleation can be induced by the presence of other crystals in the system; nuclei are often generated in the vicinity of crystals present in a supersaturated system. Usually, this kind of behavior is hard to model as it involves various factors difficult to incorporate in the model (Gerstlauer 2002, and Leubner 2002) and is thus often neglected in the calculations.

### 2.3.2. Growth Kinetics

Growth kinetic is essential to establish and solve the population balances (Mullin 1971, Randolph 1971, Randolph 1988, Nývlt 1985, and Žekić 2003). Growth rate may be defined in terms of a characteristic crystal dimension:

$$G = \frac{\beta_s}{3\alpha_v\rho} R_g = \frac{dL}{dt} \quad (2.10)$$

It can also be defined in term of crystal mass:

$$R_g = \frac{1}{A} \frac{dw_c}{dt} = k_{g,0} \exp\left(-\frac{E}{RT}\right) \Delta C^g \quad (2.11)$$

The growth rate is a function of temperature and supersaturation, thus the cooling rate of the crystallization has a major influence on the growth of the crystals. When incorporated into a population balance, the growth rate usually is assumed independent of crystal size or to follow a simple expression such as

$$G = G_0 (1 + \alpha_0 L)^{\gamma_0} \quad (2.12)$$

where the parameters  $G_0$ ,  $\alpha_0$  and  $\gamma_0$  are experimentally determined.

In order to have a better knowledge of the evolution of CSD many techniques have been developed, among them the new Process Analytical Technology (PAT). In this present study, we will use the recently developed technique: the FBRM.

## 2.4 Technique of Measurement: FBRM

### 2.4.1 Principle

Monitoring the evolution of population distribution has always been an issue. Recently, useful techniques have been developed. They are generally known under the name of Process Analytical Technologies (PAT) (Greenberg 2002; www.fda.gov), and these measurement techniques are spreading in laboratory and industrial applications where they provide reliable, in-situ, on-line information about the evolution of a reaction.

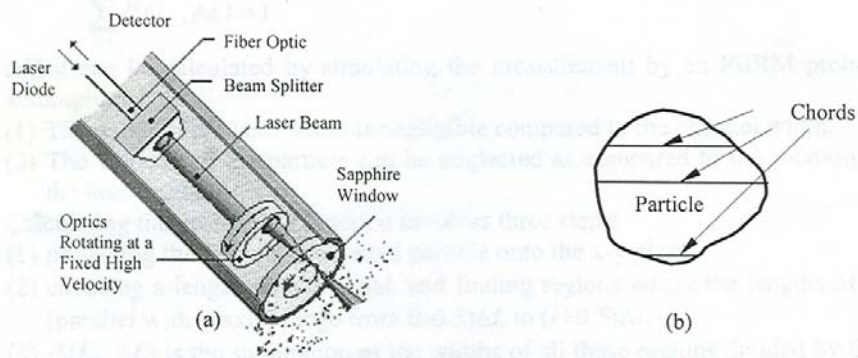


**Figure 2.4. Tip of the Lasentec probe and schematic drawing of the chords scanned.**

The FBRM used in this study is one of those newly developed techniques. It consists of a focused laser beam rotating at a constant velocity that scans the particles located in front of the probe's sapphire window. When the light emitted by the laser hits a crystal, and the sensors included in the probe record and analyze the backscattered signal. The collected data can be defined, as shown in the Figure 2.3, as the distance between two edges of the particle; the FBRM calculates this distance by multiplying the rotating speed of the laser by the time of the corresponding backscattering signal. The instrument can acquire thousands of chord lengths per second. The counts of the chords are organized in channels and expressed as a distribution, referred to as the chord length distribution (CLD). The data collected by the Lasentec® software are available for direct observation

on the computer screen and can be saved for further exploitation, the software is designed such as allowing the transfer of the data to an excel folder.

#### **2.4.2 Data Collected: CLD**

The distribution given by the FBRM measurement is an indication of the real population. The CLD is statistically related to the CSD but is not identical or even proportional to the CSD. A crystal of maximum size  $L$  cannot generate a chord length longer than this value, but it does generate chord lengths lower than this maximum dimension. However, the CSD is the description of the crystal population that allows meaningful characterization of a crystal product. Thus, it would be highly useful to be able to restore the CSD from a measured CLD.

#### **2.4.3 Relationship between CSD and CLD**

The calculation of the CSD from CLD data has been the subject of many publications (Ruf 2000, Worlitchek 2003, Shi 2002, Li 2005). This restoration calls upon probability functions where Monte-Carlo simulations are a useful tool as the relationship between the two distributions is mainly based on probabilities. A simple program to evaluate a conversion matrix  $A$ , key component to a simple relation between the CLD and the CSD, is proposed in *Appendix C*, a detailed explanation of the method is exposed in Chapter IV.

Being able to obtain the desired CSD has many advantages and leads to easier modelization and/or operation of downstream processes. In the case of pharmaceuticals a narrow CSD is desired usually to allow a more uniform dissolution rate of the drug. When a smaller mean size is desired, additional downstream processes, such as milling, are used to reduce it, but this adds to the time and money spent on the process.

## **2.5 Fines Removal**

Fines removal has been shown to have a large influence on the population distribution (Sutradhar 1993, Jones 1984 and Zipp 1989). In order to realize this removal, a fines trap can be used (Saeman 1961). It has been shown that the number of small crystals rapidly decreases, thus increasing the mean size of the population (Jones 1984). Several analyses of this effect of trapping the particles smaller than a pre-defined dimension have been published (Saeman 1961, Sutradhar 1993).

Classified product removal, (Randolph 1971) is another mean of utilizing selective removal of crystals. The CSD resulting from this generation has a narrower distribution and a reduced mean size. Févotte (Févotte 2002) also proposes slight heating of the slurry by a few degrees after nucleation, thus dissolving the smaller crystals and increasing the mean size. Modeling fines removal has been proposed in the literature (Kind 1995), as well as for the use of a classifier (West 2000). Destruction of the fines was described by Zipp (Zipp 1989). Crystallizers have been specifically designed in order to realize this operation such as the double draw off (DDO) crystallizers (White 1989).

All of those studies demonstrate that removing and dissolving the fines has a major influence on the population distribution. In this study, such a system was used to manipulate the population distribution. The dimension of the fines removed can be determined via simple equations (*see Appendix B*).

## **2.6 Chemicals Used: Paracetamol / Ethanol**

Many studies related to the use of paracetamol have been done. Parameters for the crystallization of paracetamol are thus easily accessible in the literature (Worlitchek

2003, MSDS, Al-Zoubi 2003, Beyer 2001 and Braun 2004). Both seeded and cooled crystallization can be realized. It has been shown that for high enough mean size, the crystal size distribution is bi-modal (Worlitchek 2003), a seeding or the use of a fine removal system can prevent it.

Paracetamol exists under 3 polymorphic forms (Beyer 2001), meaning that different solid state structures exist for this compound. There is a stable form: form I, a metastable one: form II and a less stable one: form III. The lattice describing the structure for form I is called monoclinic, while the structure for form II is described by an orthorhombic lattice as shown on the Figure 2.5.

The orthorhombic lattice is defined such that the three axes have different length ( $a \neq b \neq c$ ) and the three angles are equals to  $90^\circ$  ( $\alpha = \beta = \gamma = 90^\circ$ ). Figure 2.5 illustrates this arrangement.

Only form II is used to make tablets, as it is easier to compress and more stable under this form. The physical properties allow better dissolution and absorption in the body.

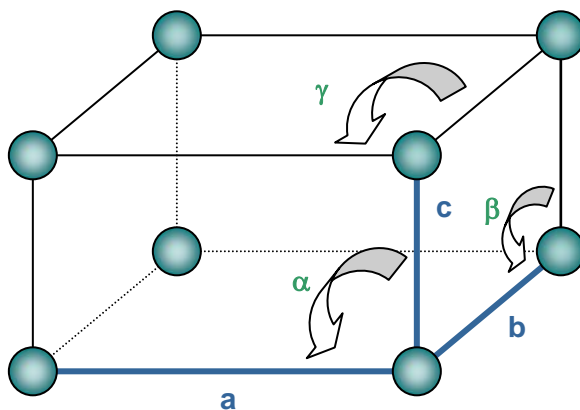


**Figure 2.5. Orthorhombic lattice**

The monoclinic lattice is defined such that the three axes have different lengths ( $a \neq b \neq c$ ), and only 2 angles are equal to  $90^\circ$  ( $\gamma = \beta = 90^\circ \neq \alpha$ ). Figure 2.6 illustrates this particular disposition of the molecules.

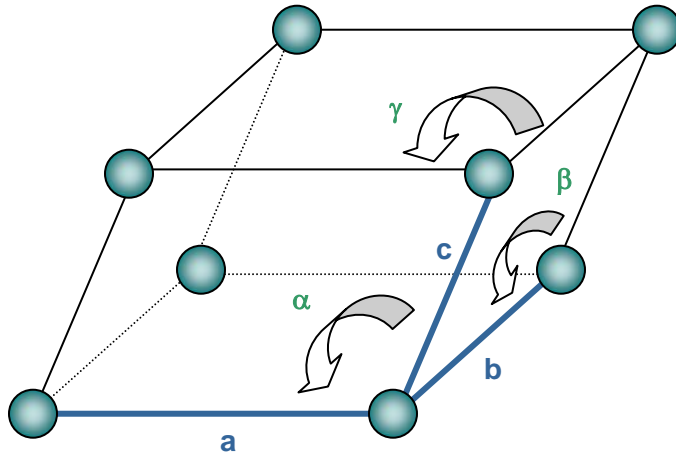


**Figure 2.6. Monoclinic lattice**

## 2.7 Population Balance

Growth kinetics can be expressed as a function of the supersaturation and the temperature according to equation 2.14.

$$G = k_g \exp(E_a / RT) \Delta C^g \quad (2.14)$$

In his work, Worlitschek proposes values for the constants thus determining fully the expression of the growth rate for crystallization of paracetamol in ethanol solutions (Worlitschek 2003).

For batch cooling crystallization (no fines removal), the population balance is given by:

$$\frac{\partial n}{\partial t} = \frac{\partial(nG)}{\partial L} \quad (2.15)$$

Randolph and Larson (Randolph & Larson 1988) developed a method to solve this equation by using the moments of the distribution. Assuming constant growth rate  $G_0$ , the equation then becomes:

$$m_j = \int_0^{\infty} n L^j dL \quad (2.16)$$

$$\frac{dm_j}{dt} = L(t=0)^j \cdot B^0 - jG_0 m_{j-1} \quad (2.17)$$

Initial condition:  $m_0 = \int_0^{\infty} n dL = 1 \quad (2.18)$

Thus the system is fully defined and the moments can be calculated step-by-step assuming the growth rate and the nucleation rate  $B^0$  are known. Simple methods described by Randolph and Larson allow the reconstitution of the population distribution.

When fines removal system is added, another term appear in the previous equation:

$$\frac{\partial n}{\partial t} = -\frac{\partial(nG)}{\partial L} - \frac{Q(L)n}{V} \quad (2.19)$$

Where  $Q(L) = Q_f$  if  $L < L_f$  and  $Q(L) = 0$  if  $L > L_f$

$L_f$  is set by the flow rate of the peristaltic pump in the fines removal system.

## 2.8 Solubility Data

Solubility of the considered solute in the considered solvent constitute a key information in the crystallization process as it gives information on the relative proportions needed to generate saturation of the solution. Knowing that the nucleation occurs when the solution is supersaturated, it is useful to know the metastable limit and the solubility curve.

This information can be obtained experimentally or it can also be calculated.

Schroeder-Van Laar equation:  $\ln(a_i x) = \frac{\Delta_m h(T_m)}{R} \left( \frac{1}{T_m} - \frac{1}{T} \right) \quad (2.20)$

Where  $x$  mole fraction,  $a_i$  activity coefficient

In order to calculate the activity we use a NRTL model due to the nature of the alcoholic solution (paracetamol + ethanol).

$$\ln(a_i) = (1-x)^2 \left[ \tau_{21} \left( \frac{G_{21}}{x + (1-x)G_{21}} \right)^2 + \frac{\tau_{12}G_{12}}{((1-x) + xG_{12})^2} \right] \quad (2.21)$$

$$G_{12} = \exp(-\alpha_n \tau_{12}) \quad \text{and} \quad G_{21} = \exp(-\alpha_n \tau_{21}) \quad (2.22)$$

$$\tau_{12} = \Delta g_{12} / RT \quad \text{and} \quad \tau_{21} = \Delta g_{21} / RT \quad (2.23)$$

Three independent parameters to characterize the behavior of the binary solution paracetamol-ethanol:  $\alpha_n = 22.3$ ,  $\Delta g_{12} = -427$ ,  $\Delta g_{21} = 2291$  (Worlitschek 2003)

$$T_m = 169.4^\circ\text{C}$$

$$\Delta_m h = 26030 \text{ J/mol}$$

Plot  $w_g$  in function of T

$$x = \frac{w_p / M_p}{w_p / M_p + (1-w_p) / M_e} \quad (2.24)$$

So

$$w_p = -\frac{M_e}{M_p} x \left/ \left( x * \left( 1 - \frac{M_p}{M_e} \right) - 1 \right) \right. \quad (2.25)$$

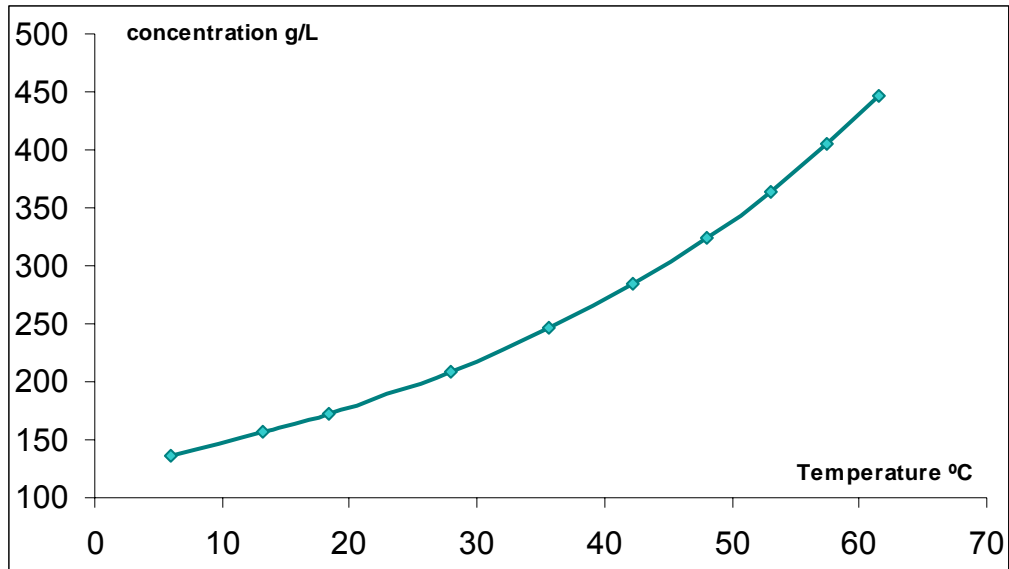


**Figure 2.7. Solubility of Paracetamol in Ethanol ( Prediction of the Model)**

Figure 2.7 shows the evolution of the solubility of paracetamol in ethanol solutions as the temperature decreases so does the amount of paracetamol soluble in this alcoholic solvent. The solubility varies greatly with the temperature thus justifying the use of a cooling crystallization, if the variation of the solubility with the temperature was minimum, another type of crystallization would have been more suitable, such as evaporative crystallization.

## CHAPTER III

### METHODOLOGY

Batch crystallization is widely used in the industry and its control constitutes a major concern. In order to better understand and implement a control scheme of the batch crystallization studied here, an experimental apparatus was designed. The experimental protocol used is developed further in this chapter.

#### 3.1 Experimental Design

A schematic diagram of the crystallization system used in the present study is shown in Figure 3.1. The primary unit was a 500-mL jacketed batch crystallizer. Mixing was provided by a 4-blade impeller rotating at a speed of 400 rpm; 3 baffles and the FBRM probe served to enhance the mixing. The Reynolds number for mixing ( $N_{RE} = D_i^2 N_s \rho / \mu$ ) was estimated to be 8,900, which was combined with visual observations to indicate good mixing. Insertion of a thermocouple into the slurry measured the temperature of the system, which was recorded through an Omega Daq 56 data acquisition system with a precision between 0.10 and 0.20 °C. A condenser on top of the crystallizer condensed any vapors of ethanol generated in the process, thereby eliminating solvent loss.

A Lasentec Focused Beam Reflectance Measurement (FBRM) D600 provided on-line monitoring of the evolution of the crystal population. The FBRM probe emits an infrared laser beam that is rotating at high velocities; when the laser beam hits a crystal, the light is backscattered to the probe, and the instrument software analyzes the signal and provides a chord length estimated from the time interval over which the signal was

received and the rotational velocity of the beam. The chord-length distribution (CLD) in the present work was obtained by averaging the set of such signals received over successive 10-s increments and was expressed in the form of counts/s vs. chord length.

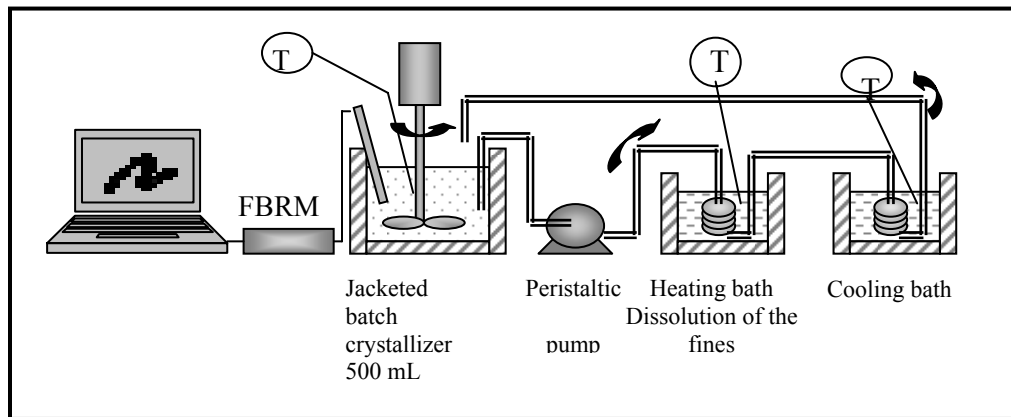


**Figure 3.1. Schematic diagram of the experimental apparatus**

In those experiments where preferential fines removal was implemented, the equipment that selectively removed small crystals from the well-mixed region of the crystallizer was an important part of the apparatus. Included were a clear tube with an inside diameter of  $\frac{1}{4}$  in. (6.4 mm), a peristaltic pump, and heating and cooling baths. The peristaltic pump drew a fines-rich stream upwards so that larger crystals, whose terminal velocity was greater than the upward liquid velocity, fell back into the well-mixed region of the crystallizer. The rate of removal of fines from the crystallizer was determined by the speed of the pump. The slurry, whose solids were dominated by fines, was pumped through a heating bath whose temperature was maintained at approximately 60 °C, which caused dissolution of the crystals. The resulting solution was then cooled to a temperature slightly above saturation before it is returned to the crystallizer.

In a typical run, the solute and the solvent (34 wt% paracetamol, 66 wt% ethanol) were added to the crystallizer, and the resulting solution was heated to 73 °C, which insured complete dissolution of the crystals. The system was then cooled and the data acquisition was started. The system was cooled at a pre-determined linear rate from 73 °C to 13 °C, at which it was held until equilibrium between the solution and the generated crystals was reached (for paracetamol, this was approximately 11 h). In those runs in which fines destruction was implemented, fines were pumped out of the slurry in the crystallizer, dissolved as described previously, and the resulting solution fed back to the crystallizer.

The rate of removal of fines from the crystallizer was determined by the speed of the pump that was set at 20 mL/min when the system was activated (*see calibration curve Appendix A*). As the fines stream was drawn upwards through a vertical line, larger crystals fell back into the crystallizer because their settling velocity was greater than that of the upward fines flow (*see calculations Appendix B*).

The CLD was determined by the FBRM, analyzed, and translated into a CSD (*see program Appendix C*). The FBRM probe uses an infrared laser beam rotating at high velocities. When the laser hits a crystal, the light is backscattered to the probe and software analyzes the signal and provides a chord-length distribution in the form of counts/s vs. chord length at the time of measurement. A typical histogram is shown in Figure 3.2.; the data were obtained at a given time for a run in which the cooling rate was  $-0.10$  °C/min, the feed was a mixture of paracetamol in ethanol, and there was no fines removal.

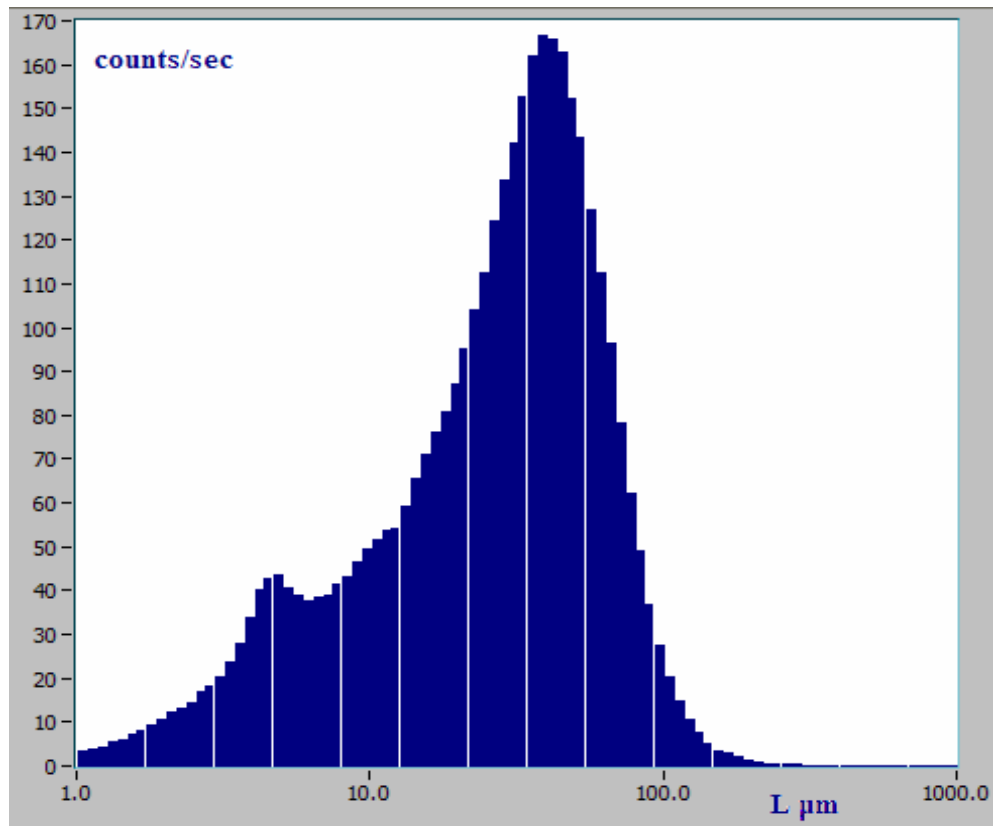


**Figure 3.2. Chord Length Distribution, Paracetamol-Ethanol, Cooling rate – 0.10 °C/min (end of the run)**

The experiments presented in this study have been performed using paracetamol in ethanol solutions. The batch cooling crystallizations were done for cooling rates ranging from – 0.50 °C/min to – 0.10 °C/min. The flow rate of the fines removal stream was set either at 20 mL/min or 0 ml/min. This is summarized in Table 3.1.

**Table 3.1 Experiments realized**

	Cooling rate °C/min	Flow rate fine removal
1	-0.10	0 mL/min
2	-0.10	20 mL/min
3	-0.20	0 mL/min
4	-0.20	20 mL/min
5	-0.35	0 mL/min
6	-0.35	20 mL/min
7	-0.50	0 mL/min
8	-0.50	20 mL/min

Three runs were done at each set of conditions to insure that the results were reproducible. An arithmetic average was then realized on the three sets of data. In Figure 3.2 the CLD corresponding to a run where the cooling rate was  $-0.10^{\circ}\text{C}/\text{min}$  is shown. We can see that the system is dilute (relatively low counts) and that the distribution is bi-modal. This bi-modality is expected due to previous observations on this system's behavior (Worlitschek 2003) and disappears when a fines removal system is used.

## **3.2 Procedures**

### **3.2.1 FBRM Experiments**

An FBRM probe was inserted in the crystallizer to monitor on-line the evolution of the crystal population. The principles on which this technique works can be found in Chapter II.

### 3.2.2 Washing & Drying of Paracetamol Crystals

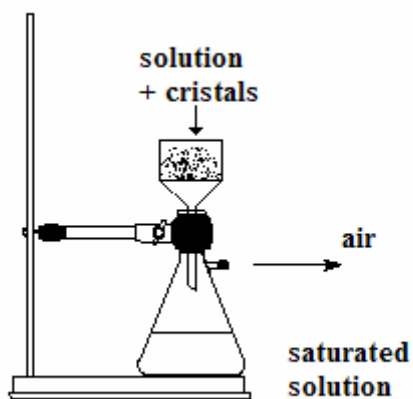


Figure 3.3. Filtration of the Solution

The final slurry of crystals in mother liquor was removed from the crystallizer, and the crystals were recovered by filtration using a Buckner funnel as shown in Figure 3.3. The recovered crystals were introduced into a beaker filled with distilled water at 0°C (Paracetamol is almost insoluble in water at this temperature) and stirred with a magnetic Teflon stirrer. Once thoroughly washed, the crystals were again recovered by filtration. They were then dried at ambient temperature in order to limit the agglomeration of the particles.

### 3.2.3 Sieving



Figure 3.4 Ro-Tap

A Ro-Tap® was used to do the sieving. A stack of sieves was placed in the equipment, with the coarsest sieve opening on top, and the crystals were placed onto the top sieve. The Ro-Tap® run time was set to 45 min, and the rotation and shaking caused the crystals to distribute throughout the sieve stack. The stack was constituted of 3-in. diameter sieves, brass cloth and stainless steel mesh; the sieve openings were as follows: 850  $\mu\text{m}$ , 600  $\mu\text{m}$ , 425  $\mu\text{m}$ , 300  $\mu\text{m}$ , 212  $\mu\text{m}$ , 150  $\mu\text{m}$ , 106  $\mu\text{m}$ , 75  $\mu\text{m}$ , 53  $\mu\text{m}$ , 38  $\mu\text{m}$ , corresponding to a decrease in mesh size by  $\sqrt{2}$  for two consecutive sieve dimensions. The sieves were chosen in consideration of the fact that a limit of 1000  $\mu\text{m}$  is measurable by the FBRM. No crystals larger than 850  $\mu\text{m}$  were recovered after the sieving, and there were no chords detected by the FBRM in the larger bins, thus this limitation has little to no influence on our process.

The maximum amount of crystals allowed with such sieves is 27 g for 3-in. diameter sieves (limit: 6 kg/m<sup>2</sup>). The samples tested were weighed before classification in order to make sure that this limitation was respected.

Once the sizing of the population was complete, the particle size was analyzed. The material retained by each sieve was weighed, and the masses recorded. The population density was calculated as follows (Mullin 2001):

$$n(L_{ave}) = \frac{\Delta M}{V_s k_v \rho L_{ave}^3 \Delta L} \quad (3.1)$$

Where  $L_{ave}$  is the arithmetic mean of 2 consecutive sieve sizes and  $k_v$  is a volumetric shape factor (for paracetamol  $k_v = 0.866$  – Worlitschek 2003).

The population was then normalized (sum equals to 1), plotted and compared to the distribution given by the restoration of the CSD from the CLD determined by the FBRM.

#### **3.2.4 Observation of the Crystals**

The crystals were observed with an optical microscope, as shown in Figure 3.5, in order to confirm the expected octahedral shape (Worlitschek 2003, Beyer 2001). The crystals recovered from the sieving were deposited on a thin microscope slide thus allowing the observation, the magnification 4x, and 10x were used. The picture shown below was obtained from an experiment with a cooling rate of  $-0.10^{\circ}\text{C}/\text{min}$ , no fines removal. The magnification lens used was 10x. This picture is an example of the crystals' shape observed after each experiment.

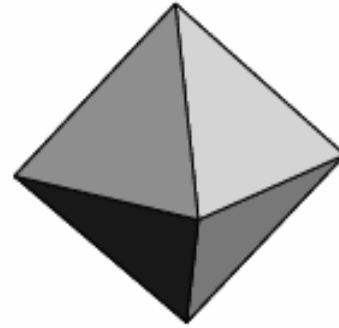
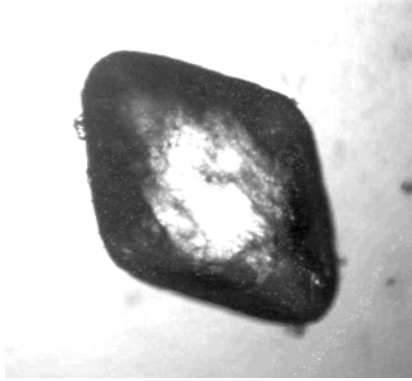


**Figure 3.5. Picture of a Crystal of paracetamol – Octahedral Shape**

### 3.3 Solution Used

The feed mixture was formed by dissolving 89.31 g of paracetamol into 262.5 g of pure ethanol. This gave a feed volume of about 400 mL.

### 3.4 Conversion of CLD to CSD

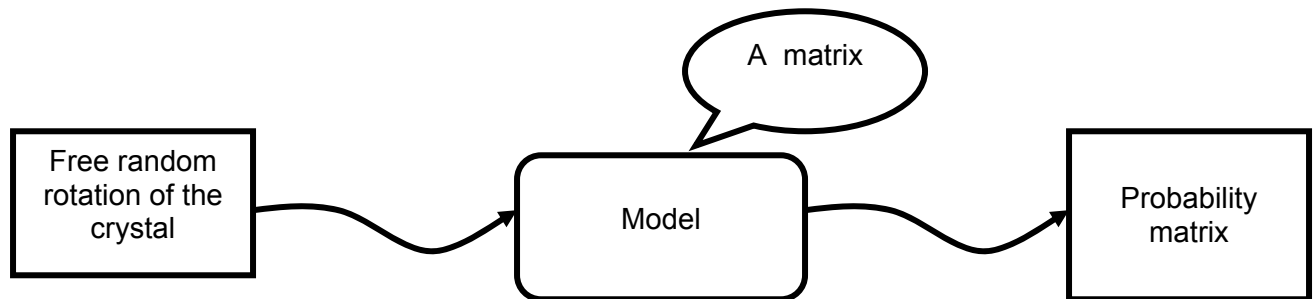


**Figure 3.6. Scheme of the computation of the matrix**

A Monte-Carlo Simulation was used to implement the model (Shi 2002). This method involves the generation and use of a set of random numbers, allowing the calculation of probabilities used to solve a given problem. The computer helps to make predictions that mimic real life. The model used is called deterministic, meaning that for a large enough number of inputs, the output will be the same no matter how many times

the probabilities are recalculated. The elaboration of the model will be further detailed in Chapter IV.

Once the CSD obtained, the mean size and the width of the distribution are calculated according to the following equations.

$$L_{mean} = \int_0^{\infty} L f_c(L) dL \quad (3.2)$$

$$\sigma^2 = \int_0^{\infty} L^2 f_c(L) dL - \left( \int_0^{\infty} L f_c(L) dL \right)^2 \quad (3.3)$$

The experimental values are then compared to the ones issued by the simulation.

## CHAPTER IV

### MODEL

In order to implement an efficient control scheme, it is essential to model the system, to be able to convert the raw data given by the FBRM (the Chord Length Distribution, CLD), to the Crystal Size Distribution (CSD). The relationship between the two distributions is complex and requires the use of distribution functions. A model taking into account this statistical relationship and allowing such a transformation is fully described in this chapter.

#### 4.1 Relationship between CLD and CSD

Batch crystallization is used widely in the production of pharmaceutical and many other specialty chemicals where it is often a key step in product recovery or purification. This operation is essential as it determines the purity, the CSD, the morphology, and the yield of the product.

Although still a significant challenge, the in-situ measurement of CSD no longer constitutes a major limitation. The development of new efficient techniques, such as the FBRM, provides a methodology for on-line monitoring of a representation of the crystal population in either batch or continuous crystallization systems. The FBRM technology is based on laser light scattering; properly installed, it allows on-line determination of the CLD (chord counts / bin), which is statistically related to the CSD and strongly depends on the geometry of the crystal. Several publications deal with the relationship between CSD and CLD, more particularly the estimation of the CSD from the CLD. For the FBRM technology, the geometry of the crystal must be well known and a 3D model needs to be established in order to implement the time-consuming calculations (Worlitschek 2003,

Wynn 2003, Ruf 2000, Li 2005 and Shi 2002). The restoration of the CSD from spherical particles has already been widely detailed in the literature. Modeling non-spherical particles is more complicated because the chords measured for a particular particle also depend on its orientation in space. The focus of this chapter is the restoration of the CSD from the measured CLD. A. Ruf and M. Mazzotti (Ruf 2000) address the issue of non-spherical particles; this publication was used as a starting point for the development of our model. A methodology using many aspects of their work is fully described in the following discussion.

#### **4.1.1 General Description of the Procedure**

The CSD and the CLD are statistically related as follows: (Ruf 2000, Shi 2002)

$$\text{CLD} = A * \text{CSD} \quad (4-1)$$

This relationship is qualitative and needs to be specified further in order to obtain a quantitative relationship; this correlation will be investigated later in this chapter (Section 4.2).

We will first focus on the computation of the conversion matrix A and then explore a way to restore the CSD from a measured CLD. To begin the evaluation of A, a description of the shape of the crystal in space is needed. The crystal can rotate freely in the slurry so, once the crystal geometry is described, all the possible orientations potentially scanned by the FBRM must be taken into account. In order to do so, a Monte-Carlo simulation has been implemented. The random movement of the particle in space will be described according to the Euler theorem and Euler angles. The FBRM measures the chord length of a randomly oriented particle. For each orientation, the 3D object representing the crystal is projected onto a 2D-plane and the corresponding CLD is calculated for that specified configuration. Physically, this means that all light is reflected directly back at the sensor, independent of the orientation of the crystal face. For each

pre-defined dimension of the particle, the CLD will be computed, thus constructing the probability matrix  $A$  in a step-by-step manner. The method used to restore the CSD from the CLD is the CLSM (Constrained Least Squares Minimization) (Worlitschek 2003). A build-in function of the software Matlab has been used to perform the minimization.

In order to model the system, we make several assumptions about the measurements. First, we have to make sure that the distance from the probe window to the particle does not influence the CLD measured, so the assumptions are made that the laser beam is focused into a point and that there is no attenuation of the signal during its propagation through the solution. Then, in order to justify a 2D projection of the 3D model, we assume that for any considered orientation of the crystal, the light is reflected back to the probe along the same incoming direction. We also assume that the flow has no influence on the measurement; i.e., the particle does not move during the measurement and that a straight line between 2 edges of the object represents the chord length. To capture the effect that larger crystals are measured more often by the probe, we assume that the probability that the beam crosses a particle having a specific 3D orientation is proportional to the vertical length (height) occupied by the corresponding 2D projection of the object. We also neglect the effect of mixing, suspension density, shadowing and masking.

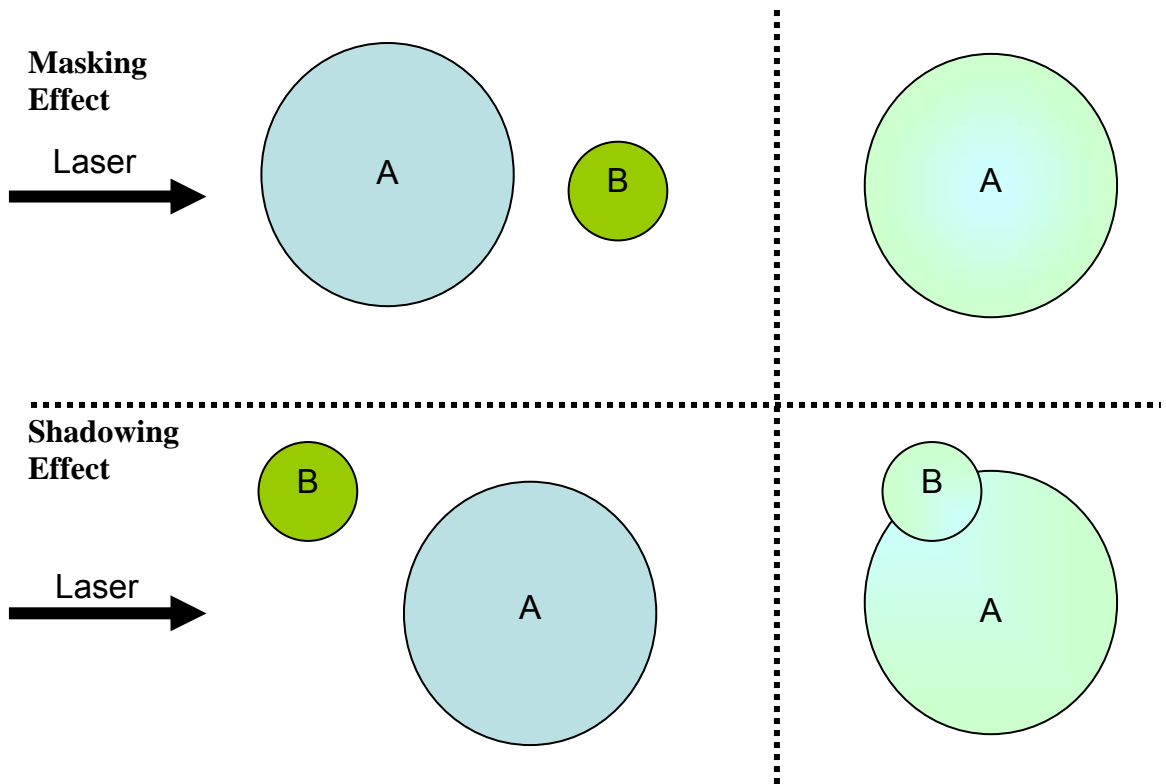


**Figure 4.1. Masking and Shadow effect**

As shown in Figure 4.1, if A is larger than B, and is located behind B, then the beam will not detect the particle that is masked by A. If B is located partially in front of a larger particle A, then the probe will only consider the particle as one. These two effects are called masking and shadowing effects, and they are neglected here. These assumptions are made so a simpler model can be implemented.

As shown in Figure 4.2, the CSD, as defined by the normalized population density  $n(L)$ , is discretized into  $n_d(L)$ . The interval (1 to 1000  $\mu\text{m}$ ) is divided into 90 size ranges, also called channels or bins (for example 100 to 107.978  $\mu\text{m}$ ). These intervals

are pre-defined by the FBRM, so that the logarithm of the ratio ( $L_{i+1}/L_i$ ) is a constant (about 0.0767).

The probable resulting CLD for a single particle of characteristic size  $L$  is represented mathematically as  $q_p(s, L)$ , where  $s$  is the representative value of chord length for a particle of size  $L$ . This distribution is computed using an algorithm defined later in this chapter, and then weighted to account for preferential sampling of large particles. Then all the weighted CLDs (one for each random orientation considered of the particle of size  $L$ ) obtained are added and the resulting distribution is normalized in order to provide the probable CLD -  $q(s)$  - corresponding to the initial distribution  $n(L)$ .

By assuming a known CSD,  $n(L)$ , and calculating the corresponding CLD,  $q(s)$ , a relationship between CLD and CSD was derived. This correlation can then be used to compute the CLD from the CSD and vice versa (see Section 4.2).

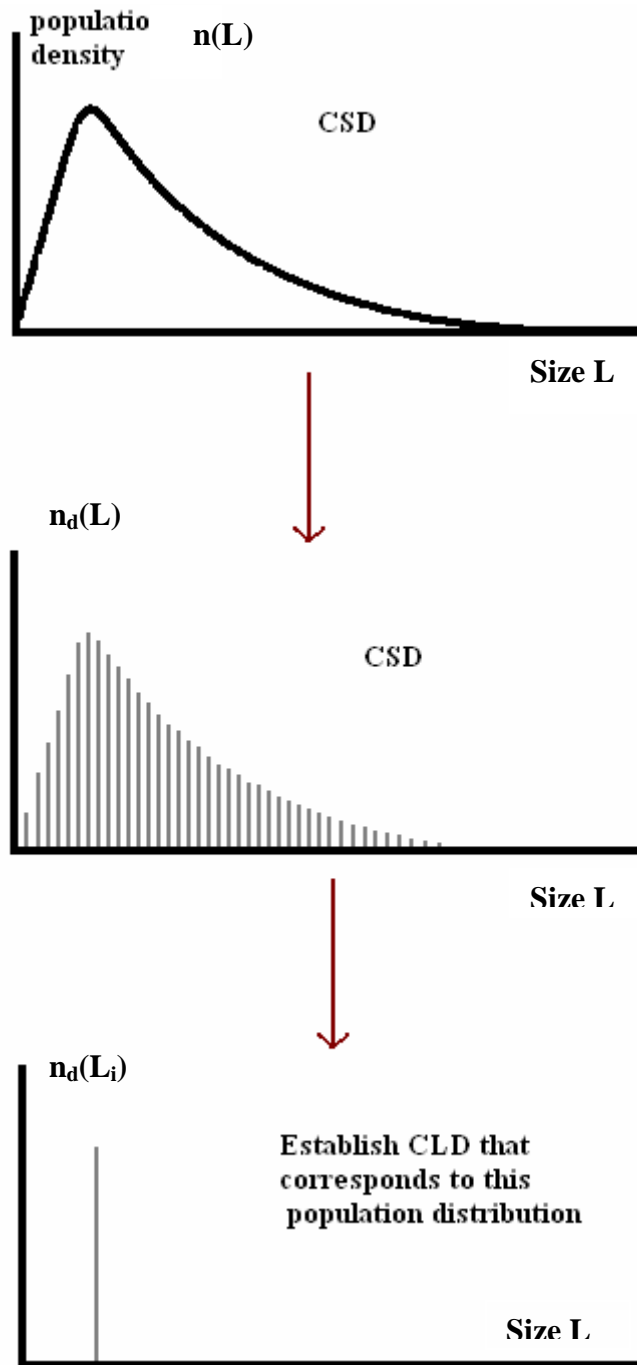


Figure 4.2. Discretization of the population density

First, we calculate the CLD,  $q_p(s,L)$  corresponding to a single particle of a known size  $L$  and geometry. Then we will generalize the process to a larger population of crystals with various sizes but the same known geometry, thus calculating  $q(s)$ .

#### 4.1.2 Step by Step Description of the Process

##### *Computation of the Matrix*

##### **Step 1-** Definition of the crystal shape in the 3D space

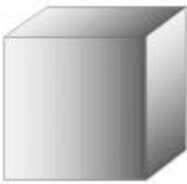
In order to implement the simulation, the geometry of the particle must be well known.

The shape of the particle is simply defined in 3D space by an ellipsoid equation (Equation 4.2):

$$\left| \frac{x}{a} \right|^k + \left| \frac{y}{b} \right|^k + \left| \frac{z}{c} \right|^k = 1 \quad (4.2)$$

The parameters  $\mathbf{a}$ ,  $\mathbf{b}$ ,  $\mathbf{c}$ , and  $\mathbf{k}$  are determined by the shape of the crystal;  $\mathbf{a}$ ,  $\mathbf{b}$ ,  $\mathbf{c}$  represent the semi-axis of the crystal, i.e. the distance along the  $\mathbf{x}$ ,  $\mathbf{y}$  and  $\mathbf{z}$  axis (as shown in Figure 4.2), and  $\mathbf{k}$  is a shape factor as illustrated below (Ruf 2000).

Here are some examples:



Cube:  $\mathbf{a} = \mathbf{b} = \mathbf{c}$  and  $\mathbf{k} = 10$

$$|x|^{10} + |y|^{10} + |z|^{10} = |a|^{10} \quad (4.3)$$

where  $\mathbf{a}$  is the semi axis corresponding to half of the face diagonal



Octahedron:  $\mathbf{a} = \mathbf{b} = \mathbf{c}$  and  $\mathbf{k} = 1$

$$|x| + |y| + |z| = |a| \quad (4.4)$$

where  $\mathbf{a}$  is half the height of the octahedron



Sphere:  $\mathbf{a} = \mathbf{b} = \mathbf{c}$  and  $\mathbf{k} = 2$

$$|x|^2 + |y|^2 + |z|^2 = |a|^2 \quad (4.5)$$

where  $a$  is the radius of the sphere

To implement this step, it is assumed that the shape of the crystal is well known. Paracetamol crystals, for example, have an octahedral shape, which means the parameters are,  $\mathbf{a} = \mathbf{b} = \mathbf{c}$  and  $\mathbf{k} = 1$ :

$$|x| + |y| + |z| = |a| \quad (4.4)$$

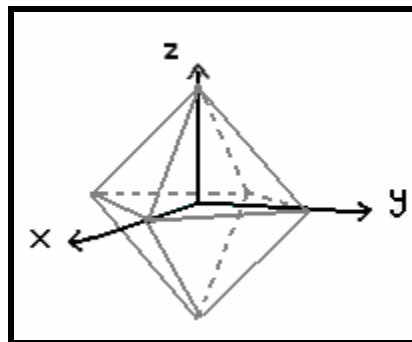


Figure 4.3. Representation of an octahedron in 3D space

Figure 4.3 represents the octahedron in 3D space as defined by Equation (4.4)

**Step 2-** Monte-Carlo Simulations: the angle of rotation is a random variable

The general expression "Monte Carlo method" relates to a wide variety of procedures. Monte Carlo (MC) methods are based on the use of random numbers and probability statistics to simulate very complex systems. For example, solving equations

that describe the interactions between two atoms is fairly simple; solving the same equations for hundreds or thousands of atoms is almost impossible. With MC methods, a large system can be modeled by a number of random configurations, that can be used to describe the system as a whole, and the problem can be solved using the resulting probabilities.

MC simulations refer to an analytical method meant to mimic a real-life system, and they are used when other analyses are too mathematically complex or too difficult to implement. A simulation automatically analyzes the effect of varying inputs on the output of the modeled system. Monte Carlo simulations involve the repetitive random generation of values for uncertain variables in order to simulate a specific model. Simulations are comprised of hundreds or even thousands of trials. The accuracy of the result depends on this number (the higher, the better) and can also depend on the quality of the random-number generator.

A wide variety of software can be used to generate random values. The problem is that computer-generated numbers aren't truly random, since computers are deterministic. But, given an initial value — generally called a random-number seed — several mathematical operations can be done on the seed so as to generate unrelated (pseudorandom) numbers. One remaining disadvantage is that if the same seed is used more than once, the same random numbers will be generated for every run. Considering that there are multiple trials, the use of different random-number seeds is crucial. Commercial programs usually pull a random seed from somewhere within the system, sometimes the time, so the seed is unlikely to be the same for two different trials.

This is the method that was used here to compute the conversion matrix A. The random numbers generated are linked to the random orientation of the particle in space. The software used to produce this set of numbers uses time as the seed.

**Step 3-** Generation of random rotations

A crystal in a slurry moves freely and randomly under the effect of the agitation. According to Euler's theorem, "an arbitrary rotation may be described by only three parameters". Several conventions exist for the Euler angles ( $\phi$ ,  $\theta$ ,  $\psi$ ), the most commonly used are: the 'x-convention', the 'y-convention' and the 'x, y, z - convention'. For each convention, a matrix has been developed to express the coordinates in the new basis (after a random rotation) as a function of the coordinates in the first basis. Figure 4.4 shows a rotation around the x-axis by an angle  $\alpha$ .

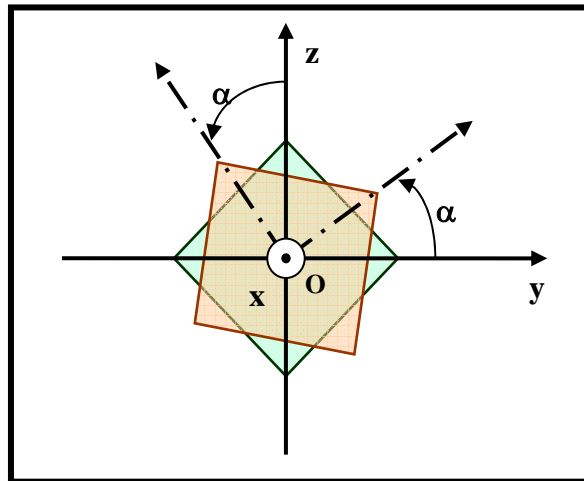


**Figure 4.4.** Rotation of an object by an angle  $\alpha$  and around the x-axis.

The rotation matrix is obtained by multiplying the matrices of the individual transformations. Positive rotations in the mathematical sense are counterclockwise:

$$\text{Rotation by } \alpha \text{ about the z-axis: } Z(\alpha) = \begin{pmatrix} \cos \alpha & \sin \alpha & 0 \\ -\sin \alpha & \cos \alpha & 0 \\ 0 & 0 & 1 \end{pmatrix} \quad (4.6)$$

$$\text{Rotation by } \beta \text{ about the x-axis: } X(\beta) = \begin{pmatrix} 1 & 0 & 0 \\ 0 & \cos \beta & \sin \beta \\ 0 & -\sin \beta & \cos \beta \end{pmatrix} \quad (4.7)$$

$$\text{Rotation by } \gamma \text{ about the y-axis: } Y(\gamma) = \begin{pmatrix} \cos \gamma & 0 & -\sin \gamma \\ 0 & 1 & 0 \\ \sin \gamma & 0 & \cos \gamma \end{pmatrix} \quad (4.8)$$

For the 'x, y, z' convention also known as the 'pitch-roll-yaw' convention (In an airplane or similar craft, the three axes are called roll, pitch, and yaw:  $\theta$  is pitch,  $\psi$  is roll, and  $\phi$  is yaw). The first rotation is along the z-axis by  $\phi \in [0, 2\pi]$ , then the second is around the new y-axis by  $\theta \in [0, \pi]$  and the third is along the new x-axis by  $\psi \in [0, 2\pi]$ , the matrix representing this transformation is:

$$R_{x,y,z} = X(\psi) * Y(\theta) * Z(\phi) \quad (4.9)$$

$$R_{x,y,z} = \begin{pmatrix} \cos \theta \cos \phi & \cos \theta \sin \phi & -\sin \theta \\ \sin \psi \sin \theta \cos \phi - \cos \psi \sin \phi & \sin \psi \sin \theta \sin \phi + \cos \psi \cos \phi & \cos \theta \sin \psi \\ \cos \psi \sin \theta \cos \phi + \sin \psi \sin \phi & \cos \psi \sin \theta \sin \phi - \sin \psi \cos \phi & \cos \theta \cos \psi \end{pmatrix} \quad (4.10)$$

The 'x, y, z' convention will be used in this study. Considering that any one of the three conventions would give the same results at the end of the simulation, it is in fact just a matter of preference. For this range of angles, and with a totally random definition of the angles, all the crystals orientations are equally likely.

**Step 4-** Exportation of the model in the new random basis

The model is defined in a given basis by a relationship between the coordinates such as  $f(x, y, z) = 0$ , this relationship is expressed in Equation (4.2). In order to export the model in the new basis, the new coordinates must be re-evaluated. The following equation links the old coordinates to the new ones:

$$\begin{pmatrix} x' \\ y' \\ z' \end{pmatrix} = R_{x,y,z} * \begin{pmatrix} x \\ y \\ z \end{pmatrix} \quad (4.11)$$

Inverting the matrix  $R_{x,y,z}$  leads to the expression of the former coordinates  $x, y, z$  in function of the new ones  $x', y', z'$

$$\begin{pmatrix} x \\ y \\ z \end{pmatrix} = R_{x,y,z}^{-1} * \begin{pmatrix} x' \\ y' \\ z' \end{pmatrix} = M * \begin{pmatrix} x' \\ y' \\ z' \end{pmatrix} \quad (4.12)$$

Thus the model Equation (4.1) describing the particle shape becomes

$$\left| \frac{(M_{11}x' + M_{12}y' + M_{13}z')}{a} \right|^k + \left| \frac{(M_{21}x' + M_{22}y' + M_{23}z')}{b} \right|^k + \left| \frac{(M_{31}x' + M_{32}y' + M_{33}z')}{c} \right|^k = 1 \quad (4.13)$$

For paracetamol, this equation can be simplified into:

$$\left| (M_{11}x' + M_{12}y' + M_{13}z') \right| + \left| (M_{21}x' + M_{22}y' + M_{23}z') \right| + \left| (M_{31}x' + M_{32}y' + M_{33}z') \right| = |a| \quad (4.14)$$

**Step 5-** Orthogonal projection onto the  $x', y'$ -plane,

Computation of the chord length  $s$

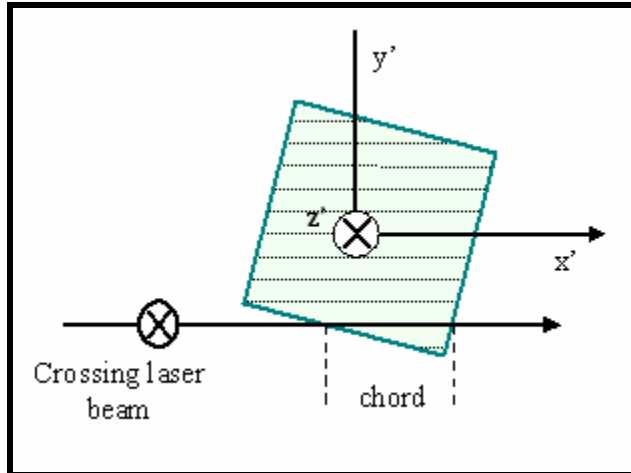


**Figure 4.5. Chord length measured by FBRM**

Now that the particle shape is fully defined in the new basis, it is necessary to describe what the FBRM actually measures, which is revealed in Figure 4.6. Considering the properties of the FBRM, the 3D shape needs to be orthogonally projected into a 2D plane in order to describe correctly the shape observed by the probe.

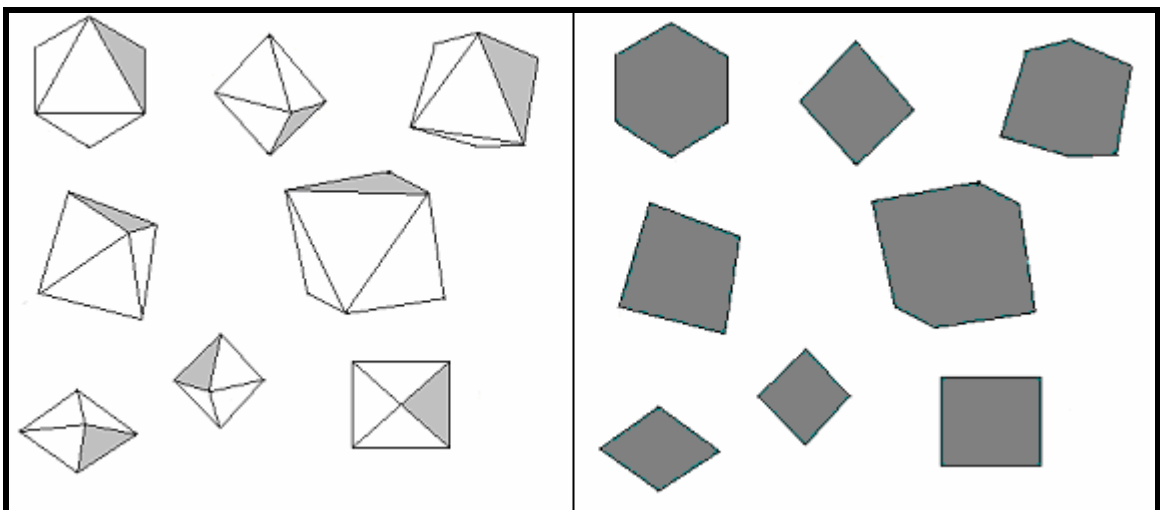


**Figure 4.6. On the left, various possible orientations of the particle -- On the right, what is measured by the FBRM (orthogonal 2D-projection of the particles located on the left). The laser beam is normal to the plane constituted by the paper.**

The FBRM laser is assumed to have a  $0^\circ$  aperture; the projection on the 2D plane is an orthogonal one, also known as orthographic projection. The 2D graphic representation of a 3D object projected onto a plane is formed by the perpendicular intersection of lines drawn from all the points on the 3D object to the plane of projection.

The 2D projection, as shown in Figure 4.7, of the particle with a specific orientation can thus be calculated. In order to realize this projection, the particle was first defined in 3D space. Considering the maximum length  $L$ , a matrix describing the  $y'$  and  $z'$ -coordinates containing equally spaced values for  $y'$  and  $z'$  was constituted and the equation determining the shape was transformed to fit the new system of coordinates. This equation was then solved for the corresponding  $x'$ -coordinate.

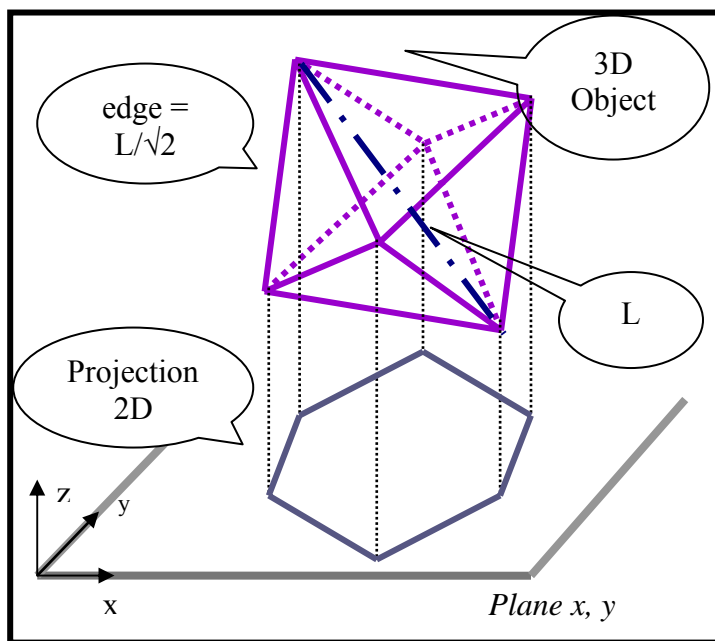


Figure 4.7. Projection of a 2D shape onto the x-y plane from a 3D object in a specific orientation

Considering that the maximum dimension is  $L$  and that the point of origin  $O(0,0)$  always is located at the center of the crystal, the maximum absolute value possible for the coordinates is  $L/2$ . Thus we could define a coordinate matrix with  $y'$ -coordinates ranging from  $-L/2$  up to  $L/2$  with those values calculated by taking either a predefined step  $\Delta y$  or a predefined number of points  $p_{\max}$ . The model was described by Equation (4.4) where  $a = L/2$ . Knowing the conversion matrix to transform from one basis to another, Equation (4.4) was then modified in order to obtain Equation (4.14) as shown previously.

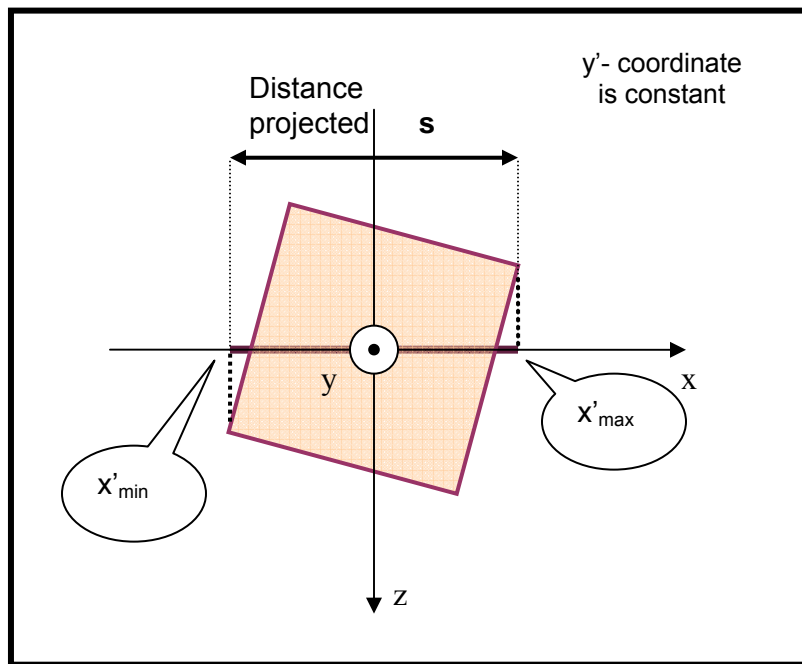


Figure 4.8. Projection onto the x-z plane

Considering that we are doing a projection onto the x-y plane, the largest distance  $s$  ( $z'$  varies) along the x-axis for a given  $y'$  is going to be projected on the plane as shown by the Figure 4.8.

Then we define a  $z'$ -coordinate matrix the same way as we defined the  $y'$ -coordinate matrix, ranging from  $L/2$  to  $-L/2$  with a predefined step size  $\Delta z$  or a predefined number of points  $n_{\max}$ . For each  $y'$ -coordinate considered, Equation (4.14) was solved for the unknown  $x'$ -coordinate, with all the  $z'$ -coordinates taken into consideration. This equation had either no solution, 1 (very unlikely, but still a possibility) or 2 solutions depending on the orientation of the crystal. When there were 1 or 2 solutions, they were recorded as  $x_1'$  and  $x_2'$ . The maximum and the minimum solutions  $x'$  found were recorded and used to calculate the projection and thus doing, the chord length  $s$  corresponding to each  $y'$ , as shown in Figure 4.8:

$$s = |x'_{\max} - x'_{\min}| \quad (4-15)$$

The chord lengths measured by the FBRM corresponded to the largest lengths along the x-axis measurable for a given  $y'$  (for all  $z'$ ).

To summarize, the object was divided into slices along the  $y$ -axis. The slices were projected onto the x-y plane, and the corresponding chord was calculated as being the length of the straight line between 2 edges of the 2D object, as illustrated in Figure 4.9. Then all the chords (for all the slices) were regrouped, according to the pre-specified bins for chord length, to implement the calculation of the discretized CLD for a single particle  $q_{p,d}(s, L)$ . The chord length distribution  $q_{p,d}(s, L)$  contains the normalized number of chords expected for each channel of  $s$ , generated by a particle of size  $L$ .

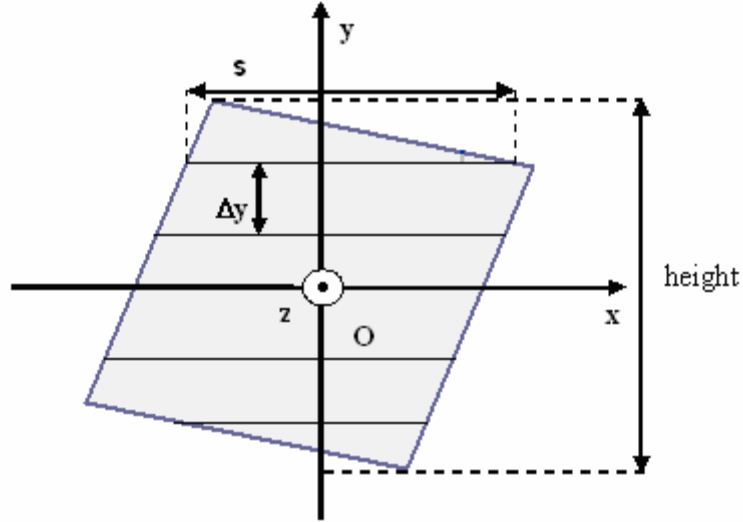


**Figure 4.9. Computation of the CLD for a random orientation projected on the plane**

The calculated chord lengths  $s$  were defined as shown in Figure 4.9. The CLD (chord counts / bin) for a particular orientation of a particle of a given characteristic size could thus be calculated.

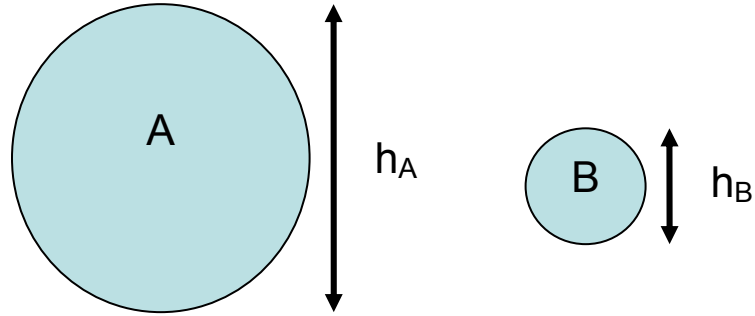
**Step 6-** Computation of the CLD for a single particle of size  $L$ ,  $q_{p,d}(s, L)$

The CLD is realized by computing the number of chord lengths in a specific channel. Once the bins are defined, the distribution can be calculated (number of chord lengths / predefined bin). The CLD is obtained by calculating how many calculated chords  $s$  are located inside each bin. The resulting CLD is then normalized to obtain  $q_{p,d}(s, L)$  (Ruf, 2000).

$$\sum_{j=1}^{90} q_{p,d}(s_j, L) * (s_{j+1} - s_j) = 1 \quad (4-16)$$

It was assumed that the probability of the laser from the FBRM striking a particle with a particular orientation is proportional to the height of the particle  $h$ . Thus each of the

CLDs (one for each random orientation) was weighted by the height of the 2D image in the new projection (Ruf 2000).



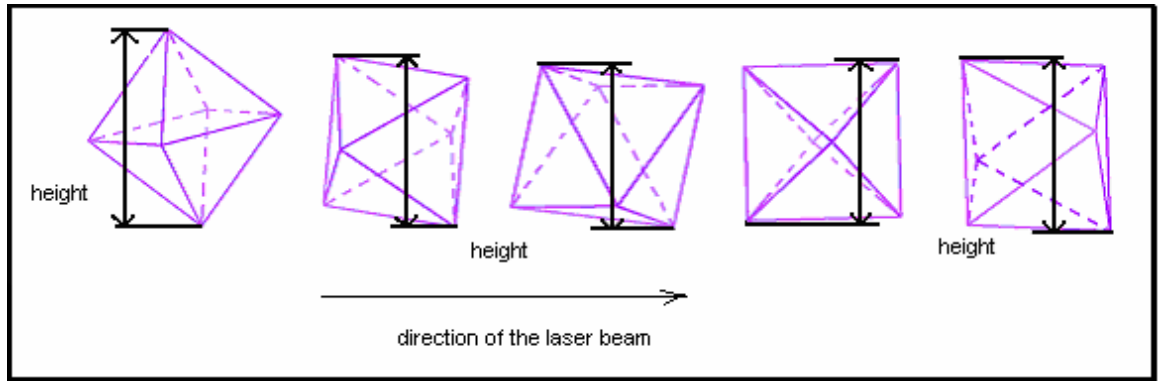
**Figure 4.10. Influence of the size of the particle**

Figure 4.10 illustrates this point by showing how a larger particle A of height  $h_A$  is more likely to be struck by the FBRM laser than a particle B of height  $h_B$ . Therefore, since the step-size in computing the CLD is constant regardless of  $h$ , the CLD of A has a larger impact on the overall CLD than the CLD of B. We account for this by weighting each calculated CLD by the height of the particle.

$$q_{p,d}(s, L) = \frac{\sum_{i=1}^{5000} q_{p,d,i}(s, L) * h_i}{\sum_{i=1}^{5000} h_i} \quad (4-17)$$

As illustrated in Figure 4.11, the height  $h$  was calculated by projecting the 6 vertices of the octahedron onto a 2D-plane and searching for the maximum absolute value  $y_{\max}$  for the  $y$ -coordinate ( $y_{\max} \leq L$ ). Considering that the system is highly symmetric,  $h$  was calculated according to the following formula:

$$h = 2 * y_{\max} \quad (4-18)$$



**Figure 4.11. Height of particle for different orientations**

**Step 7-** Probable CLD  $q_{p,d}(s, L)$  for a particle of the specified size  $L$

Steps 1 through 6 were repeated for over 5000 different random orientations, thus implementing a Monte-Carlo Simulation. The chord length distributions obtained for each orientation were weighted by the projected height of the crystal with the specified orientation. They were then summed up and the total was normalized. This results in the computation of a constant probable CLD for a single crystal of a given size  $L$ :  $q_{p,d}(s, L)$ . This simulation was realized to take into account the random orientations possible of the particle.

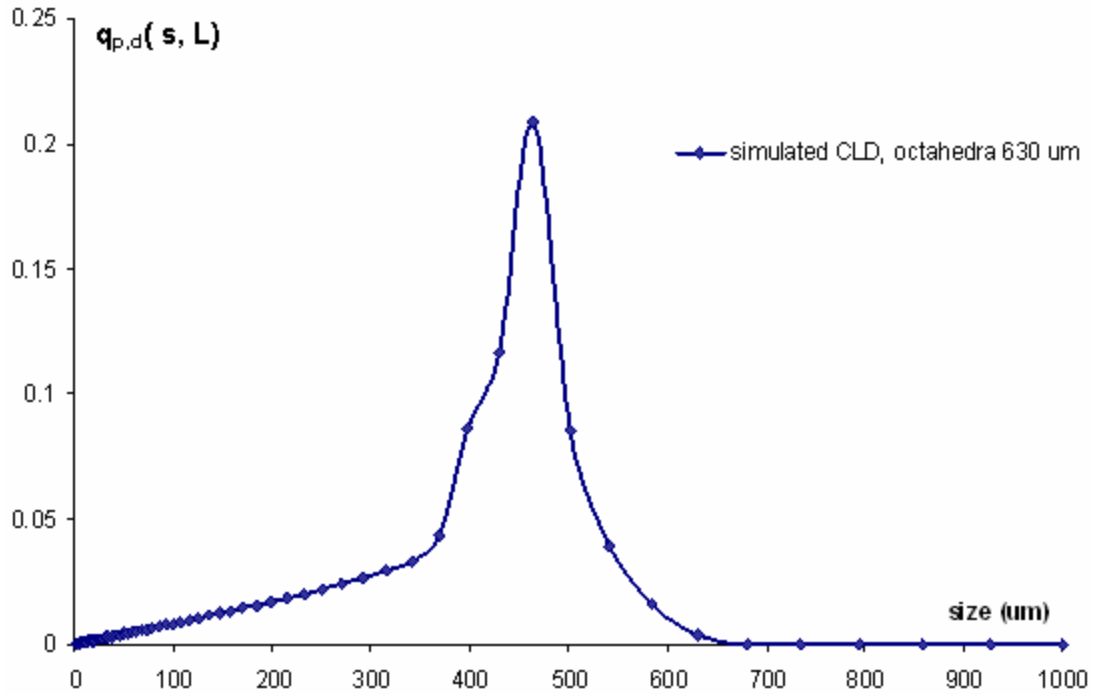
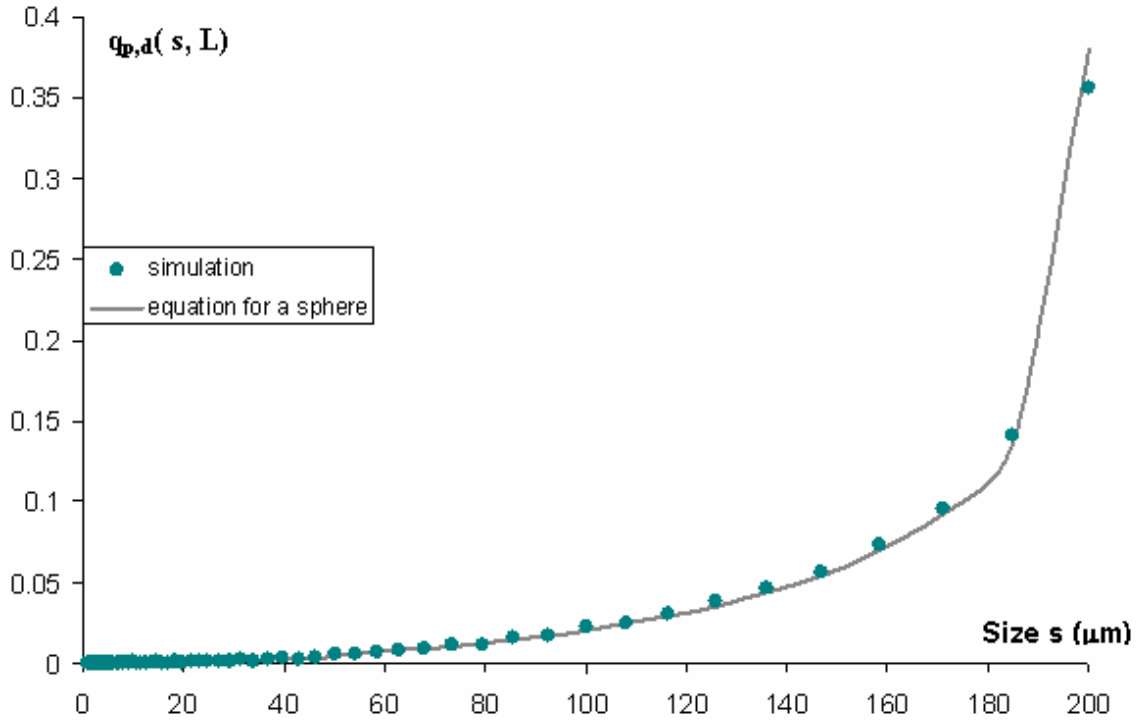


Figure 4.12. Probable CLD -  $q_{p,d}(s, L=630)$  - for an octahedron such as  $L=630 \mu\text{m}$

Figure 4.12 illustrates the distribution  $q_{p,d}(s, L)$  for  $L=630 \mu\text{m}$  for an octahedron of shape defined by  $a = b = c$  and  $k = 1$ . There is a sharp maximum for  $L/\sqrt{2} = 445.5 \mu\text{m}$  (size range: 429.866 to 464.159  $\mu\text{m}$ ), which corresponds to the length of the edges of the octahedron (see Figure 4.7), thus making it most likely to be detected. The distributions corresponding to other common shapes have been published elsewhere (Ruf 2000, Shi 2000 and Shi 2002). In contrast, the sphere geometry generates the exponentially shaped curve shown in Figure 4.13.



**Figure 4.13. Chord length distribution  $q_{p,d}(s, L)$  for a sphere of diameter  $L=200 \mu\text{m}$**

Thus the CLD,  $q_p(s,L)$ , for a single particle of known shape and size  $L$  is computed. In an attempt to clarify the process and generalize the procedure for a larger number of crystals of different sizes, but identical geometry, a simple example is presented.

We assume a discretized population distribution  $n_d(L)$  that has 1 paracetamol crystal of size  $10 \mu\text{m}$  and 1 paracetamol crystal of size  $100 \mu\text{m}$ . The paracetamol crystal has an octahedral shape. Thus the corresponding CSD, expressed as  $n_d(L)$ , is displayed in Figure 4.14.

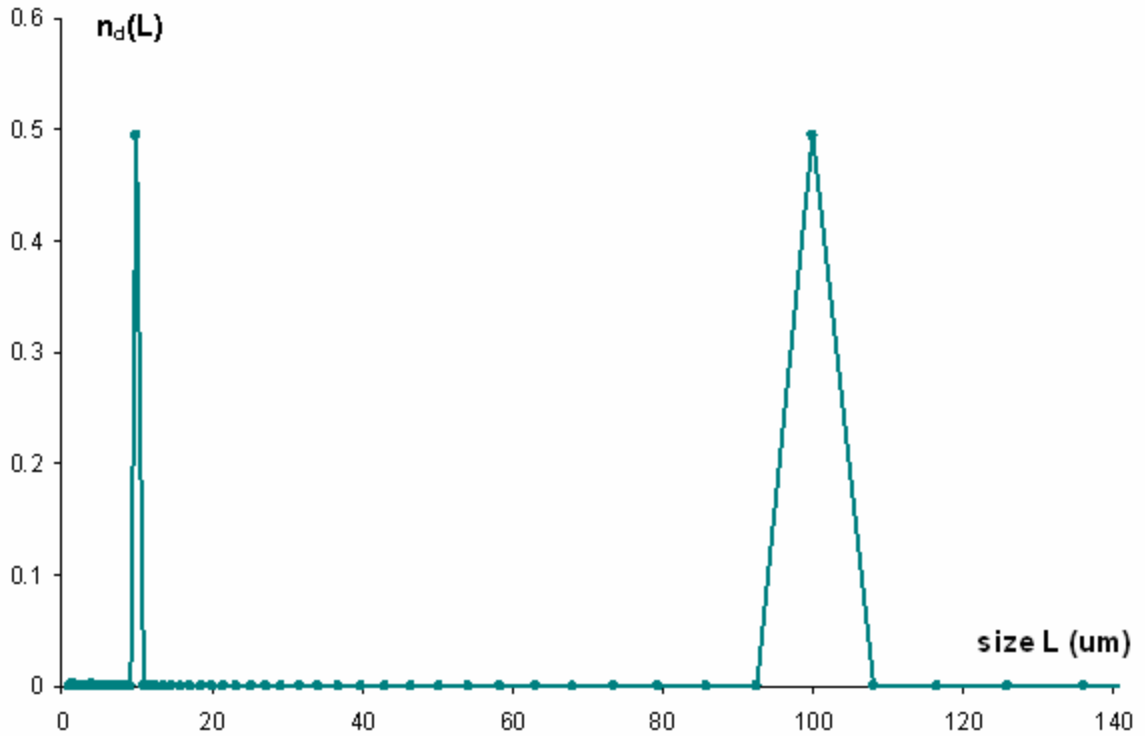


Figure 4.14. Population considered in the example,  $n_d(L)$

There is one crystal in the size range 9.261 to 10  $\mu\text{m}$  and another one in the size range 92.612-100  $\mu\text{m}$ . The computed CLD  $q_{p,d}(s, L)$  for the two crystals is shown in Figure 4.15. Both distributions were obtained according to the process described previously, and are averaged over 5000 different orientations of the particle.

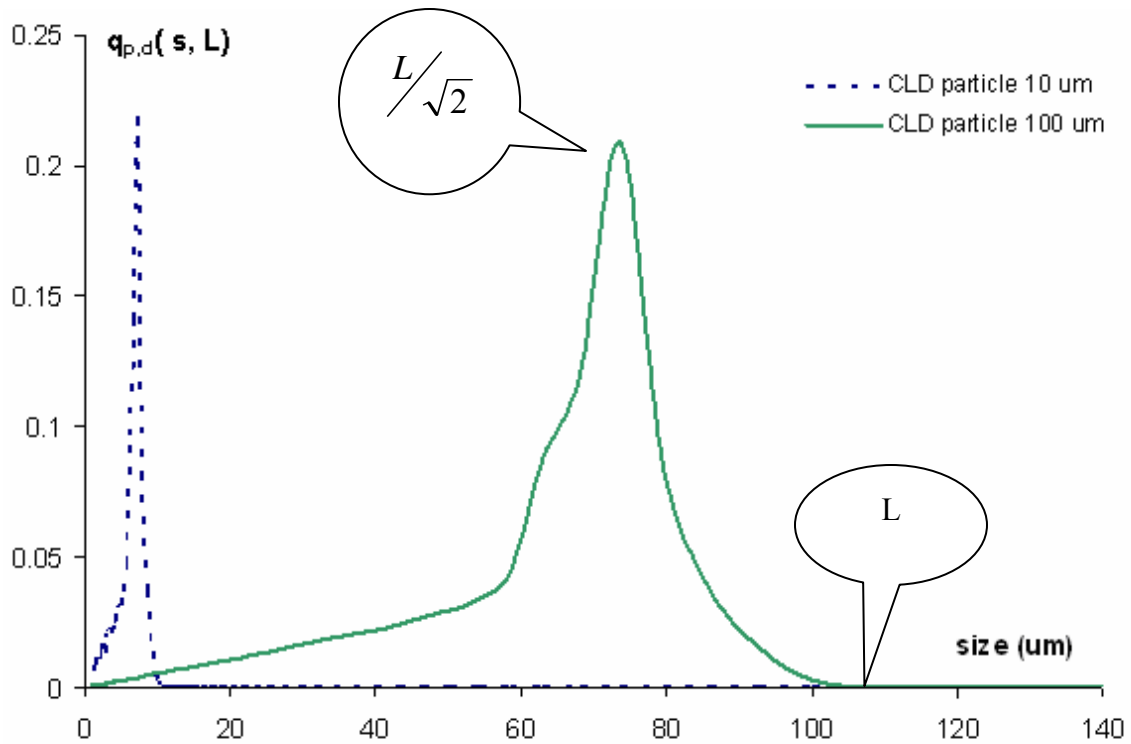


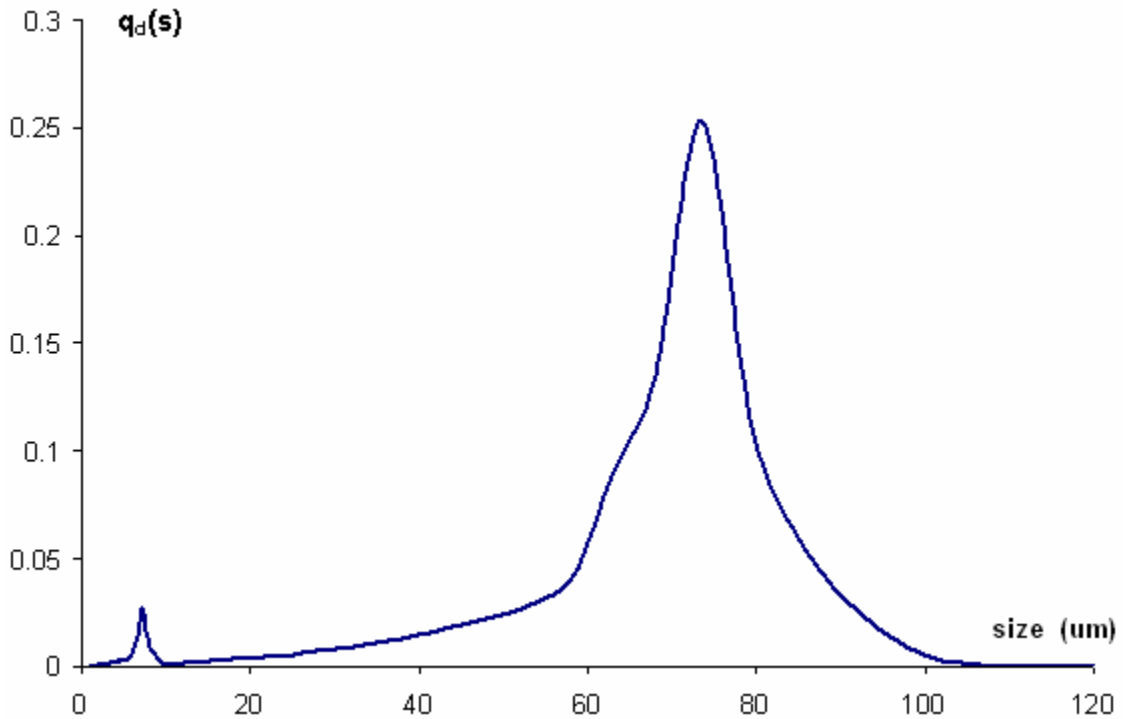
Figure 4.15.  $q_{p,d}(s, L)$  for a single particle of dimension  $10 \mu\text{m}$  and of dimension  $100 \mu\text{m}$

Figure 4.15 shows the CLDs for two crystals,  $q_{p,d}(s, L)$ , one of size  $10 \mu\text{m}$  and another of size  $100 \mu\text{m}$ . According to the same principle illustrated in Figure 4.10, the larger crystal has a larger cross-section, and therefore has a larger influence on the resulting distribution  $q(s)$ . Thus both CLDs are weighted by  $L$  before being added and normalized to form the CLD -  $q(s)$  - corresponding to the population previously described (Ruf 2000, Worlitschek 2005).

$$q(s) = \int_0^{\infty} q_p(s, L) * n_1(L) dL \quad (4-19)$$

$$n_1(L) = \frac{n(L) * L}{\int_0^{\infty} L * n(L) dL} \quad (4-20)$$

The resulting discretized chord length distribution,  $q_d(s)$  (chord counts / bin) corresponding to the continuous distribution  $q(s)$ , for the population is shown in Figure 4.16.



**Figure 4.16. CLD -  $q_d(s)$  - for the population of octahedron considered in the example**

The same procedure was used to generalize the process to a population of  $X$  crystals of different sizes. The crystal sizes  $L$  were discretized into the same bins as the chord length  $s$  so 90 representative sizes were considered. The CLDs ( $q_{p,d}(s, L)$ ) corresponding to a single particle were computed for each representative crystal sizes  $L$ . These CLDs were arranged to form a  $90 \times 90$  superior triangular conversion matrix  $A$ . This matrix was then used to restore the CSD  $-n_d(L)$  - from the CLD  $-q_d(s)$ .

## 4.2 Restoration of the CSD

It has been shown that the CSD,  $n(L)$ , and the CLD,  $q(s)$ , are statistically related. The conversion matrix  $A$  described earlier is the link between the two distributions. The qualitative relationship usually shown is expressed as follows:  $CLD = A * CSD$  (4.1). (Ruf 2000, and Shi 2002),

$$b = Ax + e \quad (4-21)$$

Where  $b$ ,  $A$ ,  $x$  are defined such as (Ruf 2000, Worlitschek 2005):

$$b(i) = \frac{1}{\ln\left(\frac{s_{i+1}}{s_i}\right)} \int_{s_i}^{s_{i+1}} q(s) ds \quad (4-22)$$

$$A(i, j) = \frac{1}{\ln\left(\frac{s_{i+1}}{s_i}\right)} \frac{\ln\left(\frac{L_{j+1}}{L_j}\right)}{(L_{j+1} - L_j)} \int_{s_i}^{s_{i+1}} \left( \int_{L_j}^{L_{j+1}} q_p(s, L) dL \right) ds \quad (4-23)$$

$$x(j) = \frac{1}{\ln\left(\frac{L_{j+1}}{L_j}\right)} \int_{L_j}^{L_{j+1}} n_1(L) dL \quad (4-24)$$

The conversion matrix  $A$  was not computed using Equation (4-23) since the continuous distribution  $q_p(s, L)$  is not known analytically, but was determined instead using Monte Carlo Simulations, as explained in the previous paragraphs and is a triangular one. Considering that the particle size is defined as being the larger dimension

of the crystal, it is not possible to measure a chord length  $s$  longer than the actual particle size  $L$ . In few cases (e.g. spherical particles), it seems easy to invert the conversion matrix in order to restore the CSD  $n_d(L)$ . Unfortunately, for most crystals geometry,  $A$  is ill-posed. The solution to the above equation is:

$$x = (A^T A)^{-1} A^T b \quad (4-25)$$

For example, the matrix can be inverted for spherical particles. But, quite often the matrix cannot be inverted or the precision on the inverse is poor, and the problem is thus said to be ill-conditioned. This is the case for octahedron (condition number of  $A = 2 \cdot 10^{18}$ ). Thus we will explore further an alternate method used elsewhere (Worlitschek 2003) to restore the CSD,  $n(L)$ : the utilization of the CLSM (Constrained Least Squares Minimization). With this method, additional constraints are added so that a unique CSD,  $n_d(L)$  can be computed from the CLD  $q_d(s)$ .

The following minimization problem is considered:

$$\min \left( \|A\hat{x} - b\|^2 + \lambda \|B\hat{x}\|^2 \right) \quad (4.26)$$

Where the Euclidian norm is used,  $\lambda$  is an apositive adjustable regularization parameter, and  $B$  is a matrix operator defining the a priori constraint.

Thus for a chosen  $B$  and  $\lambda$ , the solution to (4.18) is unique and is given by:

$$\hat{x} = (A^T A + \lambda B^T B)^{-1} A^T b \quad (4.27)$$

The matrix  $B$  and the parameter  $\lambda$  are introducing additional constraints into the system so that a unique solution to the equation exists. There are 2 common choices for  $B$  depending on the constraint one wants to impose to the system. First,  $B=I$  is said to be the 'lowest energy' solution ( $\|\hat{x}\|$  small is requested). The second possibility is to look for a solution with low curvature, in this case we use:

$$B = \begin{pmatrix} -1 & 2 & -1 & 0 & \dots & \dots & 0 \\ 0 & -1 & 2 & \ddots & \ddots & & \vdots \\ \vdots & \ddots & \ddots & \ddots & \ddots & \ddots & \vdots \\ \vdots & & \ddots & \ddots & \ddots & \ddots & 0 \\ 0 & \dots & \dots & 0 & -1 & 2 & -1 \end{pmatrix} \quad (4.28)$$

We use the matrix B in Equation (4.28) since we expect the distribution to be smooth. To obtain the parameter  $\lambda$  assuming a lack of information on the error, a plot  $\ln(\|A\hat{x} - B\|^2)$  versus  $\ln(\|B\hat{x}\|^2)$  was generated. This curve has the shape like an L, the value of  $\lambda$  was determined according to the L-curve criterion, the location of the kink of the L-curve happened for the optimum value of  $\lambda$  (Worlitschek 2003). The optimum value of  $\lambda$  is, for our system, 1.6.

Once  $\lambda$  was determined, the CSD ( $\hat{x}$ ) was then easily calculated.

$$\begin{aligned} \hat{x} &= Cb \\ C &= (A^T A + \lambda B^T B)^{-1} A^T \end{aligned} \quad (4.29)$$

Another easier way to restore the CSD, reside in the utilization of the “lsqlin” function in Matlab. This is the function we will use. It solves the minimization problem:

$$\min_x \left( \frac{1}{2} \|A * x - b\|_2^2 \right) \quad (4.30)$$

The following conditions are implemented:

- $\forall i \quad n_1(L_i) \geq 0$
- $\forall i \quad n_1(L_i) \leq 1$
- $\sum_i n_1(L_i) = 1$

The restored CSD is then normalized and then compared to the results given by the sieving experiments (see chapter V.)

For the example described previously in this chapter, the global CLD,  $q_d(s)$ , was considered in order to check if the restored CSD,  $n_d(L)$ , matched the actual population; the results are displayed in Figure 4.17. We can see 2 peaks located at 10 and 100  $\mu\text{m}$ , the restored distribution overlaps with the initial one.

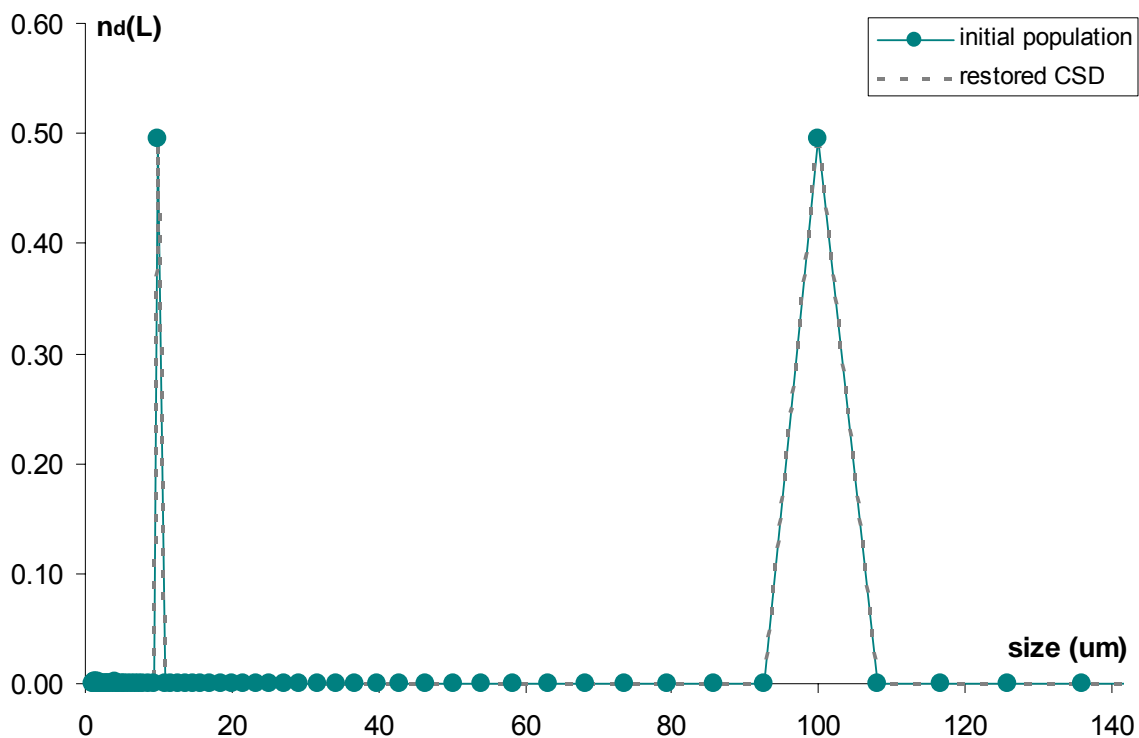


**Figure 4.17. Comparison, initial population and CSD,  $n_d(L)$  restored according to the procedure described in this chapter**

The CLD  $q_d(s)$  was then computed from the calculated CSD  $n_d(L)$  (according to equation 4.1) in order to provide another checkpoint of the model. Figure 4.18 shows the results, the two distributions overlap.

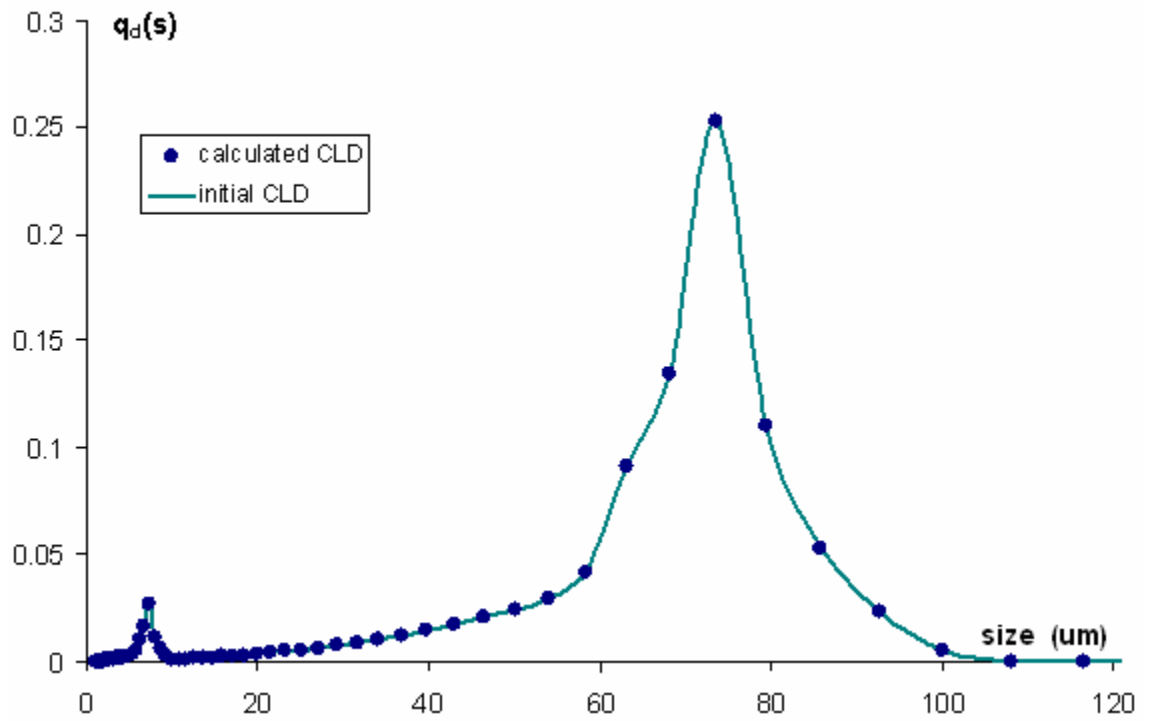


Figure 4.18. Comparison between recalculated CLD and initial CLD

This simple example illustrates the procedure that will be used to restore the population distribution  $n_d(L)$  from the discretized chord length distribution given by the FBRM  $q_d(s)$ .

## CHAPTER V

### RESULTS

The results obtained in the series of experiments described in Chapter III are presented here. The influence of the cooling rate and the fines removal system are explored. The population density obtained for each experiment is computed in two different ways. First, an experimental distribution is obtained via a sieving and weighting of the crystals; and second, the population density is restored from the CLD raw data according to the model detailed in Chapter IV.

#### 5.1 No Fines Removal

Several cooling rates were used to determine the evolution of the population as a function of the cooling rate. Each experiment was run three times in order to insure reproducibility of the results. The collected data were averaged over the three runs for each set of experimental conditions (1–3 and 4–6).

##### 5.1.1 Cooling Rate – 0.10 °C/min

Acetaminophen, also known as paracetamol, was crystallized from solutions in ethanol at a cooling rate of  $-0.10$  °C/min without fines removal. Figure 5.1 shows the evolution of the chord counts during the run as measured by the FBRM. The evolution of the temperature is also displayed on the graph. The onset of nucleation is clearly identified as occurring after about 7 hours of run time: i.e., when the temperature reached approximately 32 °C. Note that the chord counts increased steeply for all size ranges, although slightly more slowly for the larger sizes than for the smaller ones.

There was some decrease in the counts of small crystals as the run progressed, although the chord counts became nearly constant for all sizes after about 8.5 hours.

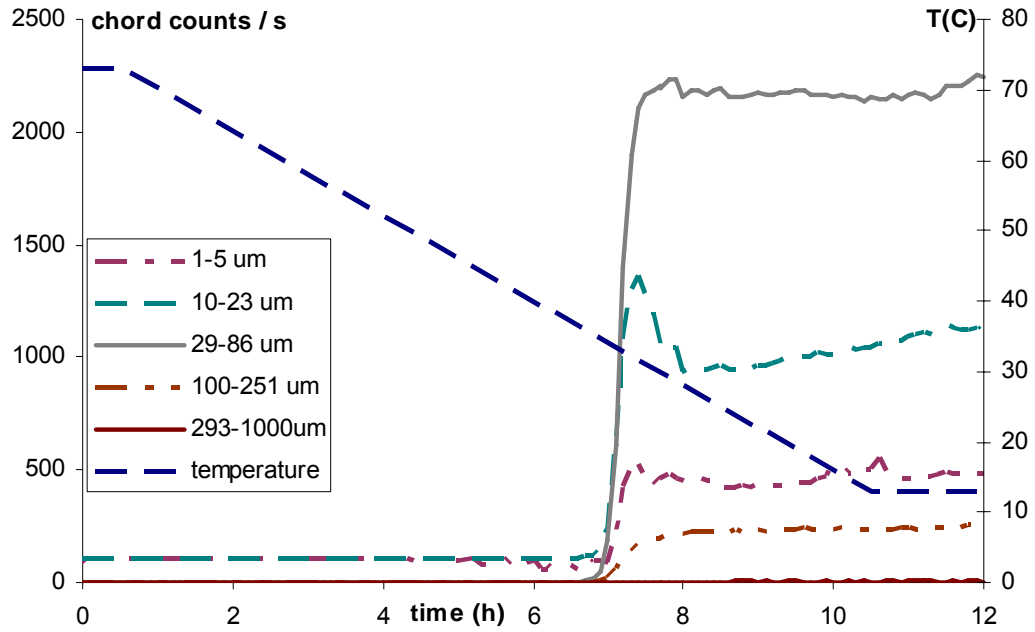


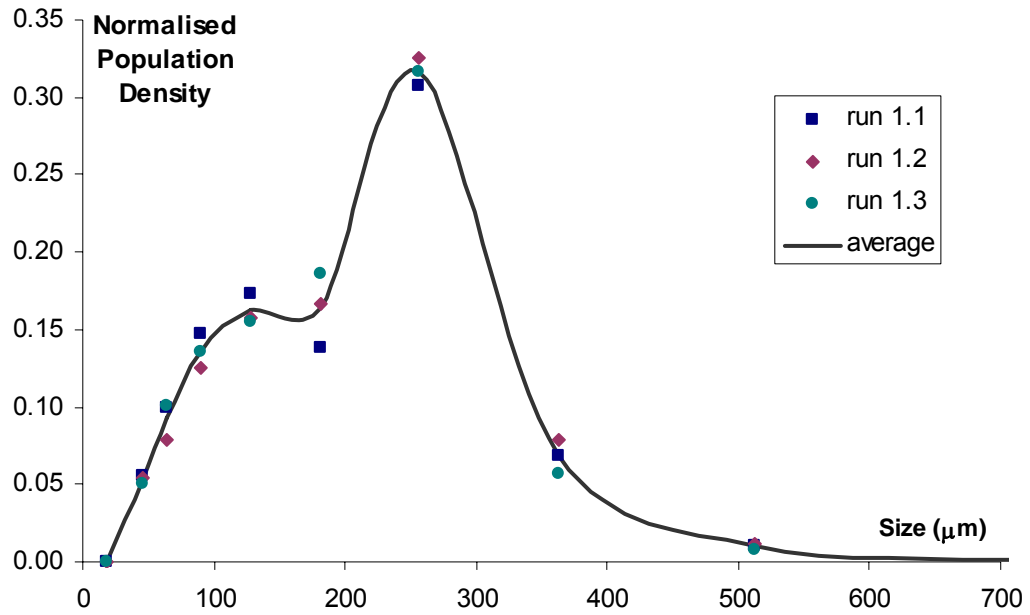
**Figure 5.3. Evolution of the chord counts and the temperature for a cooling rate of  $-0.10\text{ }^{\circ}\text{C}/\text{min}$  without fines removal**

After each run, the crystals were washed with water at  $0\text{ }^{\circ}\text{C}$ , and then dried at ambient temperature. Table 5.1 shows the results of sieve analysis performed on each crystal product. From the sieve analyses, the population distribution was determined according to the procedure explained in Chapter III. Figure 5.2 illustrate the results.

**Table 5.1. Sieving results from runs with a cooling rate of  $-0.10$  °C/min without fines removal**

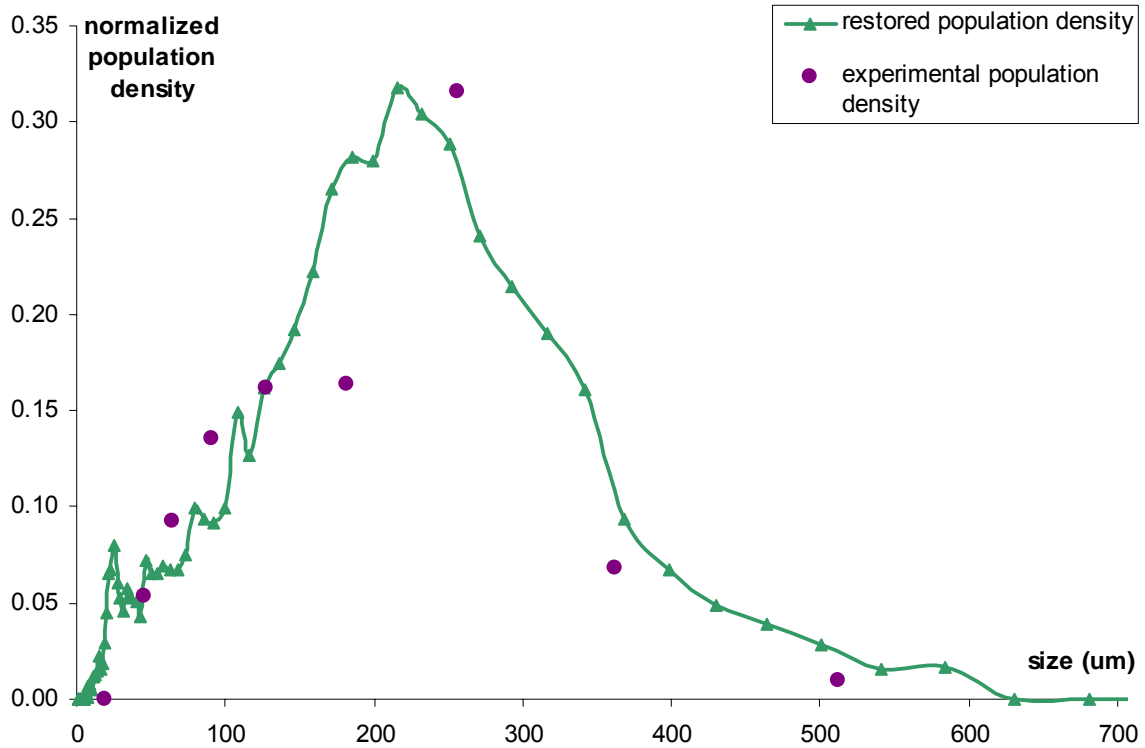
L [ $\mu\text{m}$ ]	$L_{\text{mean}}$ [ $\mu\text{m}$ ]	Run1.1 $\Delta\text{M}$ [g]	Run1.2 $\Delta\text{M}$ [g]	Run1.3 $\Delta\text{M}$ [g]
1000				
850	925	0.12	0.38	0
600	725	1.60	2.18	2.18
425	512.5	5.82	6.73	4.23
300	362.5	9.93	11.33	8.16
212	256	10.97	11.65	11.29
150	181	1.24	1.48	1.66
106	128	0.39	0.35	0.35
75	90.5	0.08	0.07	0.08
53	64	0.01	0.01	0.01
38	45.5	0.01	0.01	0
0	19	0	0	0

Figure 5.2 shows a fit of the normalized population density to the sieve data from Runs 1.1, 1.2, and 1.3. The runs were operated with a cooling rate of  $-0.10$  °C/min, but without fines removal. The data from the three runs generally are clustered close together, showing good run-to-run reproducibility. The means and spreads of the distributions were  $232.5 \pm 3.71$   $\mu\text{m}$  and  $103.3 \pm 0.26$   $\mu\text{m}$ , respectively. The fit and the data points from each run indicate that the size distribution was bimodal.



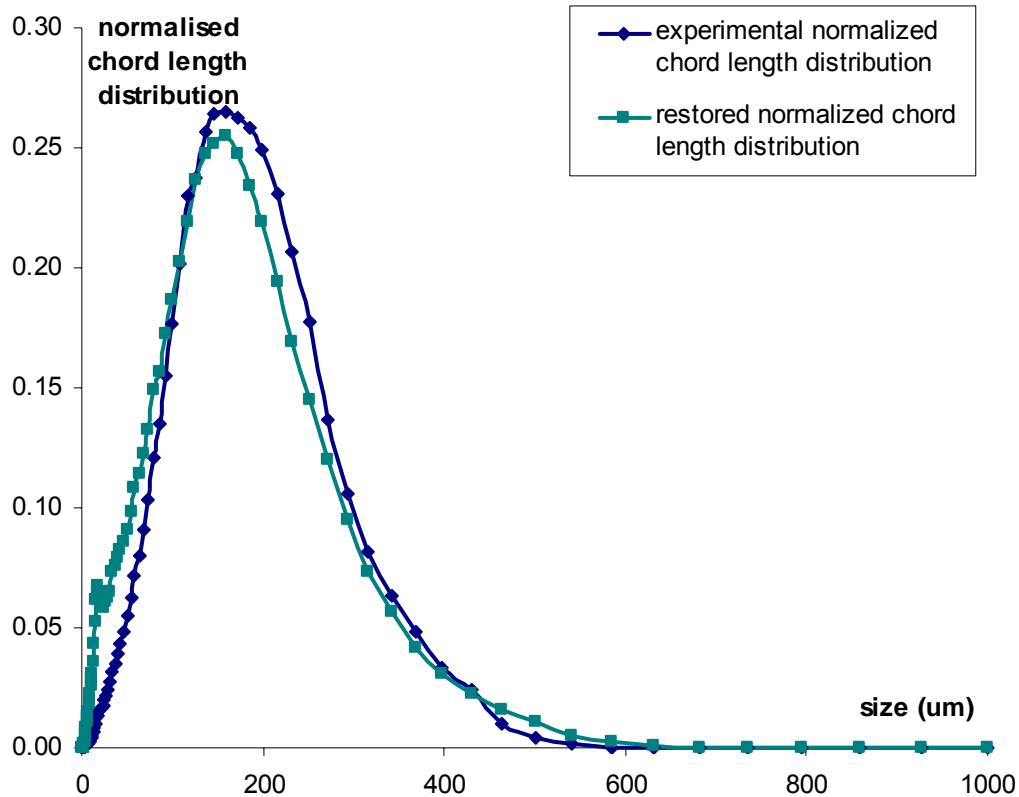
**Figure 5.2. Sieving data from runs 1.1, 1.2 and 1.3 for a cooling rate of  $-0.10$  °C/min, without fines removal**

The final normalized chord length distributions for the three runs in this set were averaged and used in conjunction with the method outlined in Chapter IV to recover the crystal size distribution, as quantified in normalized population density. A comparison between the recovered population density and the experimental values for the three runs is shown in Figure 5.3. Although somewhat noisy over smaller size ranges, agreement is reasonably good.



**Figure 5.3. Restored and Experimental distribution for a cooling rate – 0.10 °C/min, without fines removal**

Due to the method of recovery of the crystals (collection from the slurry, washing and drying), it is possible that some smaller particles were lost during the procedures and some bigger particles might have been broken during the sieving process. Those experimental conditions might explain the observed difference.



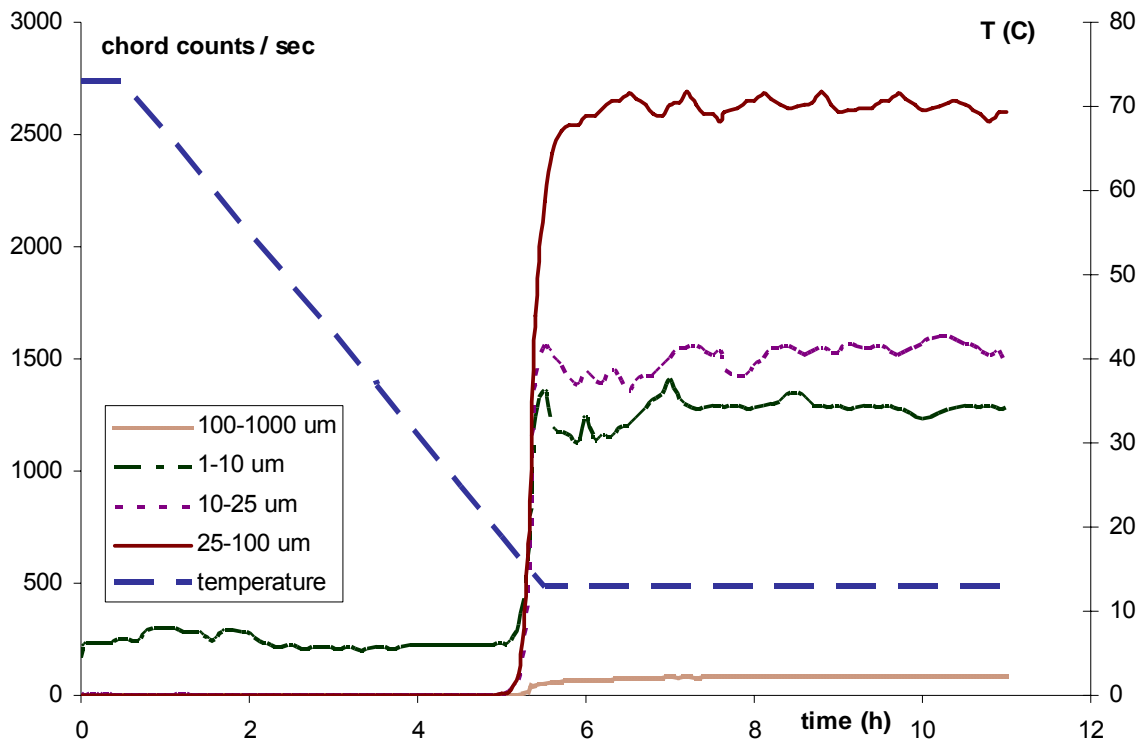
**Figure 5.4. Experimental and restored normalized chord length distributions for a cooling rate of  $-0.10\text{ }^{\circ}\text{C}/\text{min}$ , without fines removal**

Figure 5.4 shows the CLD restored from the calculated CSD according to the formula  $\text{CLD} = A * \text{CSD}$ . The two curves are comparable, this shows that going from CLD to CSD and then from CSD back to CLD does not introduce a significant variation.

### 5.1.2 Cooling Rate $-0.20\text{ }^{\circ}\text{C}/\text{min}$

Acetaminophen was crystallized from ethanol this time at a higher cooling rate of  $-0.20\text{ }^{\circ}\text{C}/\text{min}$  without fines removal. Figure 5.5 shows the evolution of the chords counts, as well as the evolution of the temperature during the run as monitored by the FBRM and the thermo-sensors. Nucleation clearly occurred after about 5.2 hours of run time; the temperature at this time was approximately  $19\text{ }^{\circ}\text{C}$ . The nucleation event

resulted in a sudden and steep rise in the chord counts for all size ranges. This increase was slightly less marked for the larger sizes compared to the smaller ones. The chord counts became nearly steady for all size ranges after about 6 hours.



**Figure 5.5. Evolution of the chord counts and the temperature for a cooling rate of  $-0.20\text{ }^{\circ}\text{C}/\text{min}$  without fines removal**

After each experiment, the crystals were washed with cold water ( $0\text{ }^{\circ}\text{C}$ ), dried at ambient temperature and classified according to their size by using a Ro-Tap sieve shaker. Table 5.2 display the results of the sieve analyses carried out after each experiment. Each sieve was then weighted and the population density was established according to the procedure described in Chapter III, and are displayed in Figure 5.6.

**Table 5.2. Sieving results from runs with a cooling rate of  $-0.20\text{ }^{\circ}\text{C}/\text{min}$  without fines removal**

L [ $\mu\text{m}$ ]	$L_{\text{mean}}[\mu\text{m}]$	Run2.1 $\Delta\text{M}$ [g]	Run2.2 $\Delta\text{M}$ [g]	Run2.3 $\Delta\text{M}$ [g]
1000				
850	925	0	0	0
600	725	1.26	1.54	1.62
425	512.5	2.15	2.64	2.77
300	362.5	4.82	5.58	2.75
212	256	7.09	7.87	6.55
150	181	4.42	6.13	6.85
106	128	1.20	1.52	1.70
75	90.5	0.25	0.28	0.35
53	64	0.02	0.04	0.03
38	45.5	0.01	0.01	0.01
0	19	0	0	0

Figure 5.6 shows a fit of the normalized population density to the sieve data from Runs 2.1, 2.2, and 2.3. The runs were operated with a cooling rate of  $-0.20\text{ }^{\circ}\text{C}/\text{min}$ , without fines removal. The data from the three runs generally show good reproducibility. The means and spreads of the distributions were  $180.7 \pm 2.74\ \mu\text{m}$  and  $82.5 \pm 0.71\ \mu\text{m}$ , respectively.

In the distribution in Figure 5.6, we can see that the mean size is shifted to lower values compared to the results obtained with the previous cooling rates. The mean size and the spread of the distribution are decreasing with the cooling rate.

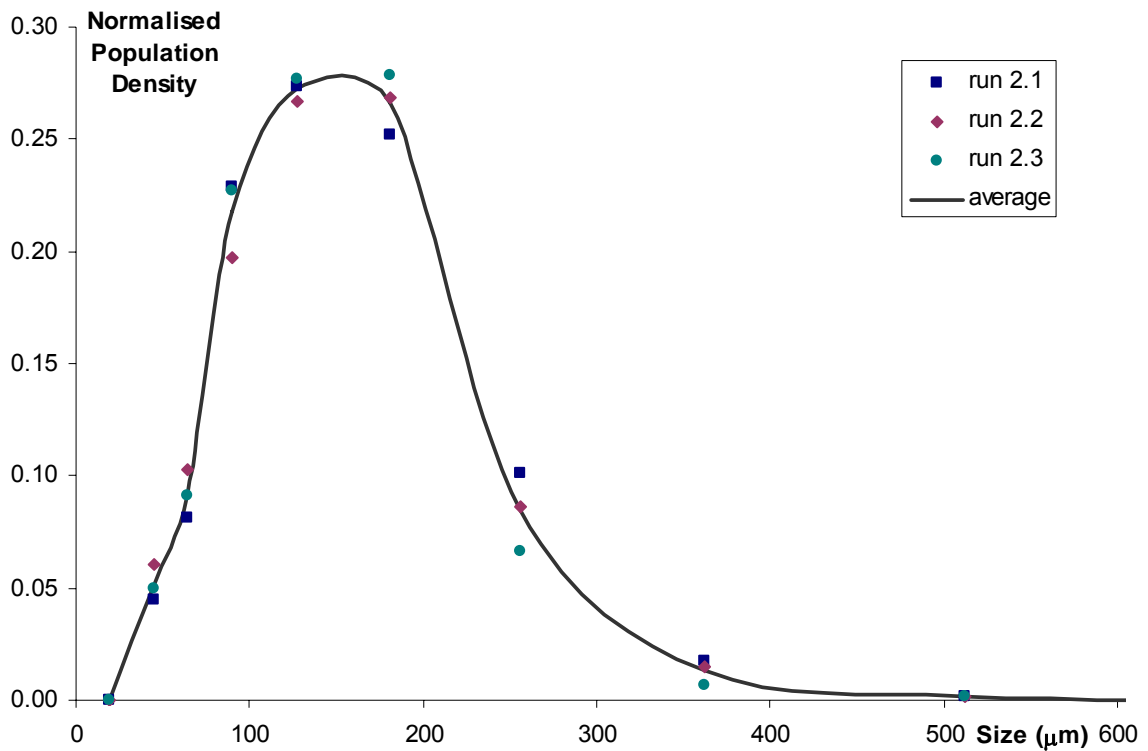


**Figure 5.6. Sieving data from runs 2.1, 2.2 and 2.3 for a cooling rate of  $-0.20$  °C/min, without fines removal**

The final normalized chord length distributions for the three runs in this second set were averaged and used to implement the method described in Chapter IV in order to recover the crystal size distribution, as quantified in normalized population density. A comparison between the recovered population density and the experimental values for the three runs is shown in Figure 5.7. Although slightly noisy over smaller size ranges, agreement is reasonably good.

A small difference is noticed and might be due to both the model employed to compute the CSD and the experimental method of recovery for the crystals.

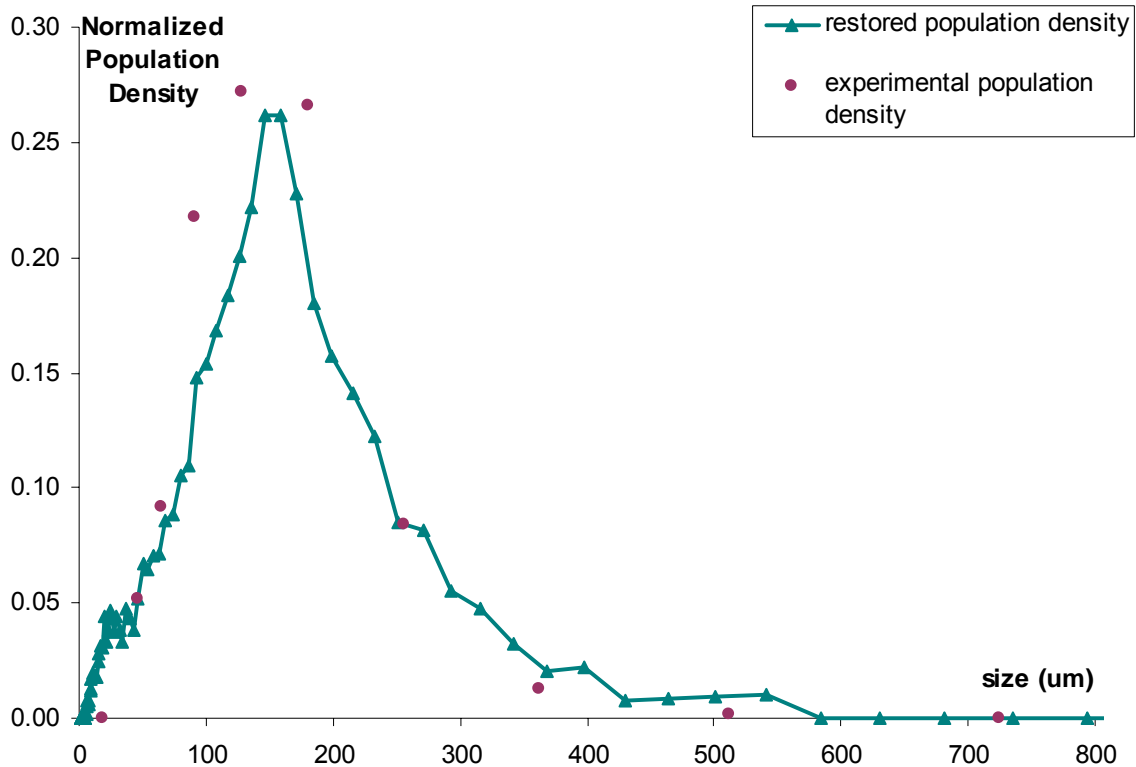


**Figure 5.7. Restored and Experimental distribution for a cooling rate – 0.20 °C/min, without fines removal**

### 5.1.3 Cooling Rate – 0.35 °C/min

The same compound was crystallized from the alcohol, this time at a cooling rate of – 0.35 °C/min, once again without fines removal. Figure 5.8 illustrates the variation of the chord counts during the run as recorded by the FBRM, the recorded evolution of the temperature is also shown. Nucleation is clearly noted as occurring after about 4.4 hours of run time, the temperature measured is approximately 13 °C. Note that the chord counts increased steeply for all size ranges, except for the larger sizes whose number is weakening as the cooling rate increases. Steady state was achieved after about 6 hours.

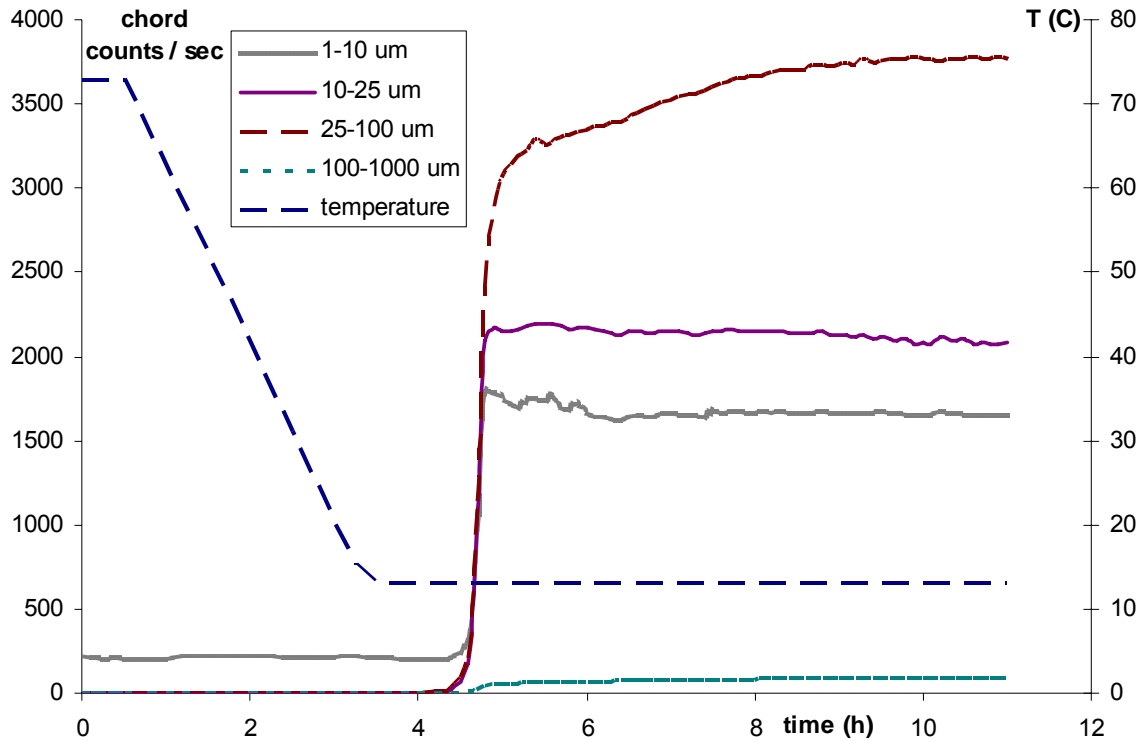


**Figure 5.8. Evolution of the chord counts and the temperature for a cooling rate of  $-0.35\text{ }^{\circ}\text{C}/\text{min}$  without fines removal**

This time again, after each run, the crystals were washed, then dried and classified according to their sizes, this was done following the procedure described earlier. Table 5.3 regroups the results of the size analysis realized on each crystal product. From this analysis, the population distribution was calculated according to the formulas detailed in Chapter III. The resulting population distribution is illustrated by Figure 5.9.

**Table 5.3. Sieving results from runs with a cooling rate of  $-0.35\text{ }^{\circ}\text{C}/\text{min}$  without fines removal**

L [ $\mu\text{m}$ ]	$L_{\text{mean}}[\mu\text{m}]$	Run3.1 $\Delta\text{M}$ [g]	Run3.2 $\Delta\text{M}$ [g]	Run3.3 $\Delta\text{M}$ [g]
1000				
850	925	0	0	0
600	725	0	0	0
425	512.5	0	0.41	0
300	362.5	4.28	9.55	7.01
212	256	13.53	10.24	11.99
150	181	7.09	5.42	6.74
106	128	2.03	1.53	2.08
75	90.5	0.47	0.35	0.45
53	64	0.09	0.06	0.05
38	45.5	0.02	0.02	0.01
0	19	0	0.00	0

Figure 5.9 shows a fit of the normalized population density to the sieve data from Runs 3.1, 3.2, and 3.3. The runs were realized with a cooling rate of  $-0.35\text{ }^{\circ}\text{C}/\text{min}$ , and without fines removal. The experimental data collected from the three runs are close, thus showing a good reproducibility of the system. The means and spreads of the distributions were  $153.27 \pm 2.08\text{ }\mu\text{m}$  and  $64.1 \pm 0.54\text{ }\mu\text{m}$ , respectively.

Figure 5.9 confirms the trend that both the mean size and the spread of the distribution are decreasing with the cooling rate.

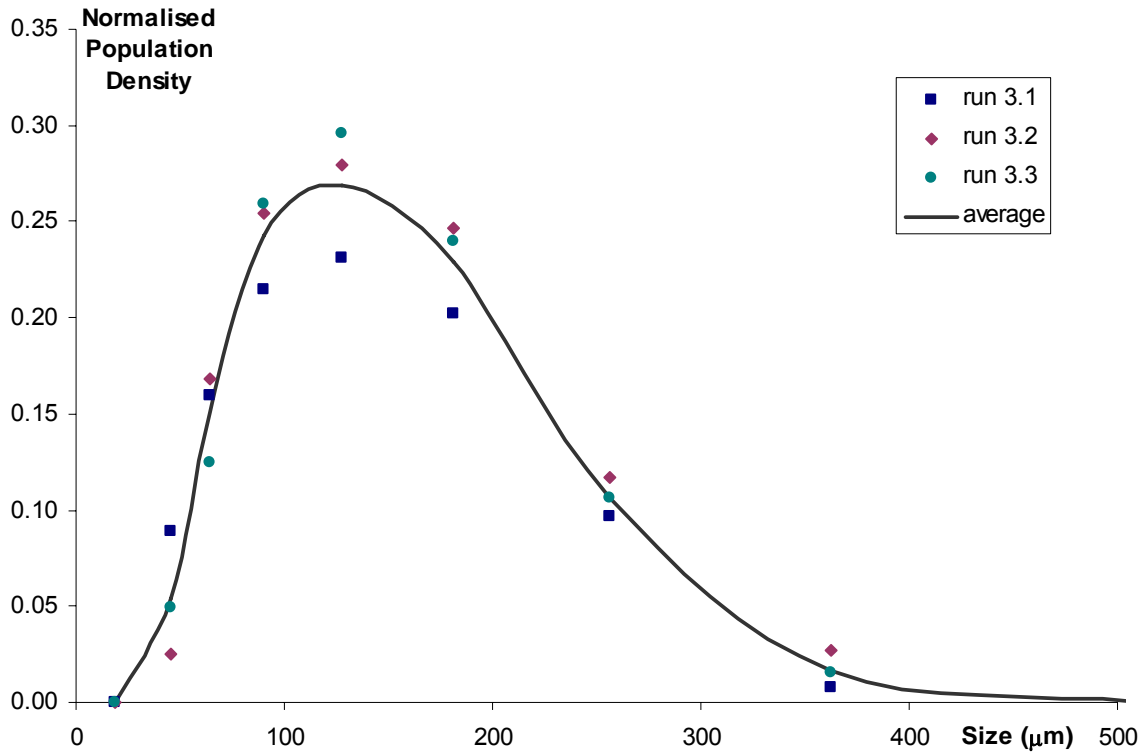


Figure 5.9. Sieving data from runs 3.1, 3.2 and 3.3 for a cooling rate of  $-0.35\text{ }^{\circ}\text{C}/\text{min}$ , without fines removal

The final normalized chord length distributions for the three runs in this third set were averaged. The resulting distribution was used to implement the model outlined in Chapter IV to recover the crystal size distribution, as quantified in normalized population density. A comparison between the recovered population density and the experimental values for the three runs is shown in Figure 5.10. Although somewhat noisy, agreement is reasonably good.

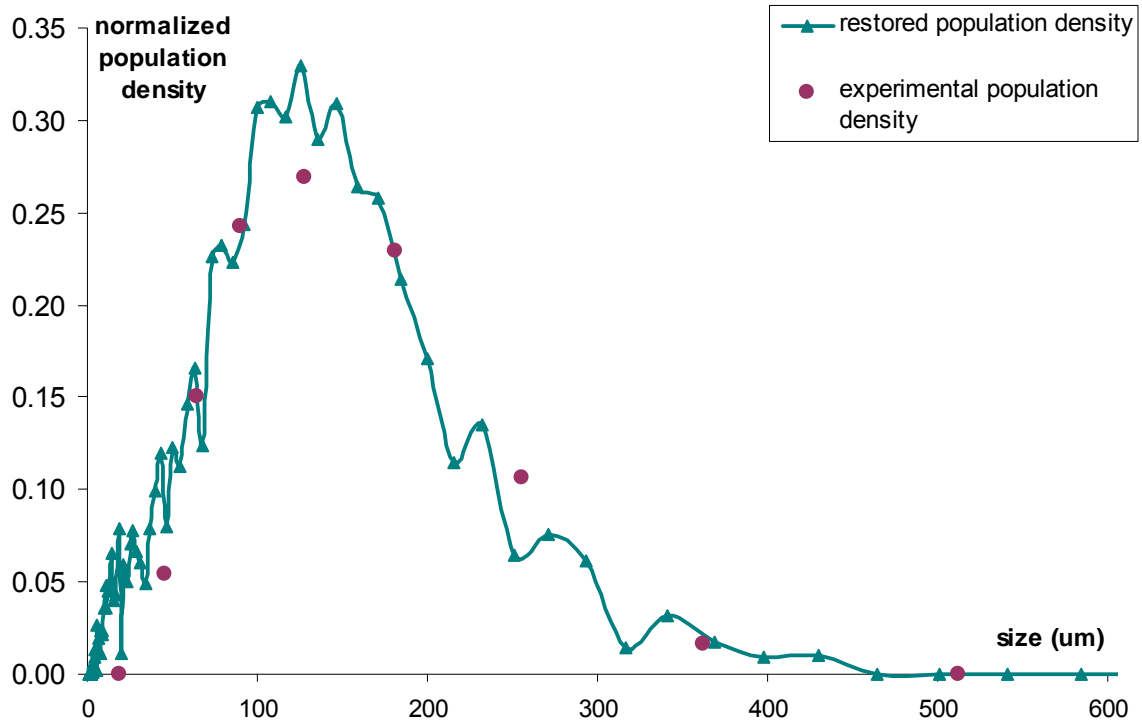
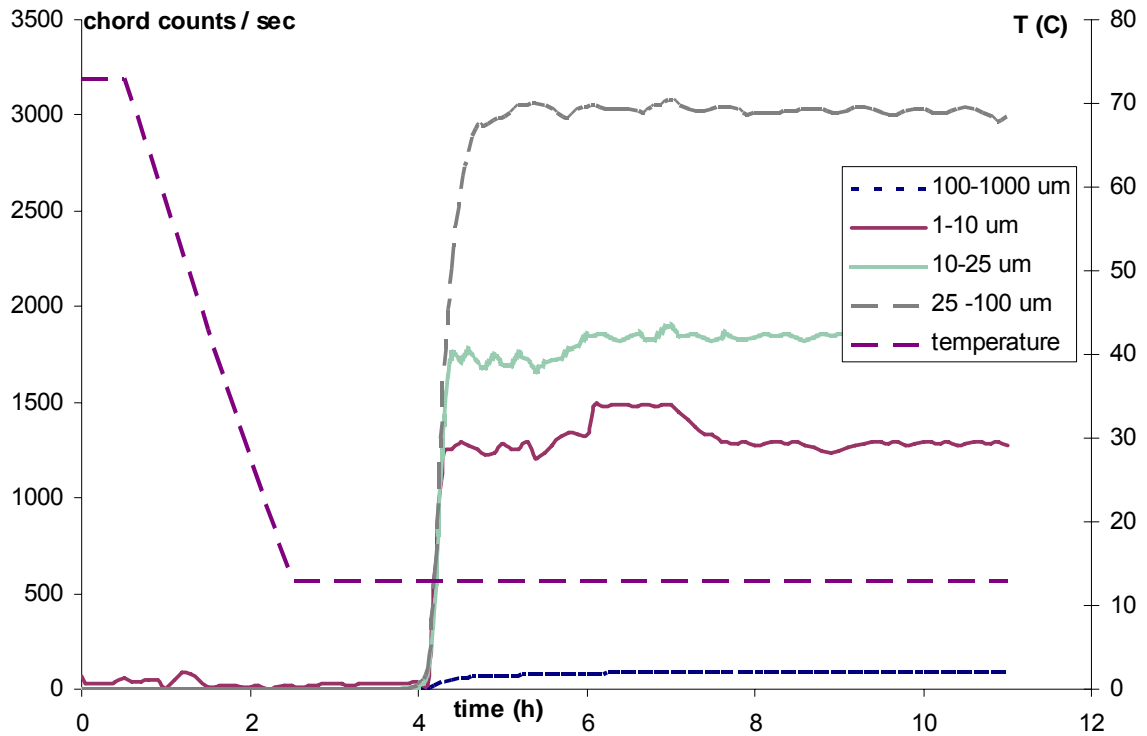


Figure 5.10. Restored and Experimental distribution for a cooling rate – 0.35 °C/min, without fines removal

#### 5.1.4 Cooling Rate – 0.50 °C/min

The crystallization is now done at a cooling rate of – 0.50 °C/min, without fines removal. Figure 5.11 shows the evolution of the counts and the temperature versus time. Nucleation occurs this time about 5 hours; then the temperature probe read 13 °C. As in the other runs, the chord counts increased abruptly for all size ranges, the counts for large chords are still lower. A constant is reached for all size ranges after 5 hours.



**Figure 5.11. Evolution of the chord counts and the temperature for a cooling rate of  $-0.50\text{ }^{\circ}\text{C}/\text{min}$  without fines removal**

As usual, the crystals obtained were washed, dried and classified. Table 5.4 shows the results of the sieve analysis performed after each experiment. The population density was then determined according to the formula explained in Chapter III, the corresponding distribution is shown in Figure 5.12. Once again, the three data sets are close, indicating that the runs are consistent.

**Table 5.4. Sieving results from runs with a cooling rate of  $-0.50\text{ }^{\circ}\text{C}/\text{min}$  without fines removal**

L [ $\mu\text{m}$ ]	$L_{\text{mean}}[\mu\text{m}]$	Run4.1 $\Delta\text{M}$ [g]	Run4.2 $\Delta\text{M}$ [g]	Run4.3 $\Delta\text{M}$ [g]
1000				
850	925	0	0	0
600	725	0	0	0
425	512.5	0	16.24	0
300	362.5	8.07	5.56	14.35
212	256	13.62	8.69	13.35
150	181	9.00	4.85	8.29
106	128	2.82	1.37	2.28
75	90.5	0.55	0.27	0.43
53	64	0.08	0.04	0.07
38	45.5	0.02	0.01	0.02
0	19	0	0	0

Figure 5.12 shows a comparison of the normalized population density to the sieve data from Runs 4.1, 4.2, and 4.3. The runs were operated with a cooling rate of  $-0.50\text{ }^{\circ}\text{C}/\text{min}$ , without fines removal. As the three data sets are giving similar results, reproducibility is insured. The means and spreads of the distributions were  $141.5 \pm 2.57\text{ }\mu\text{m}$  and  $58.42 \pm 0.61\text{ }\mu\text{m}$ , respectively.

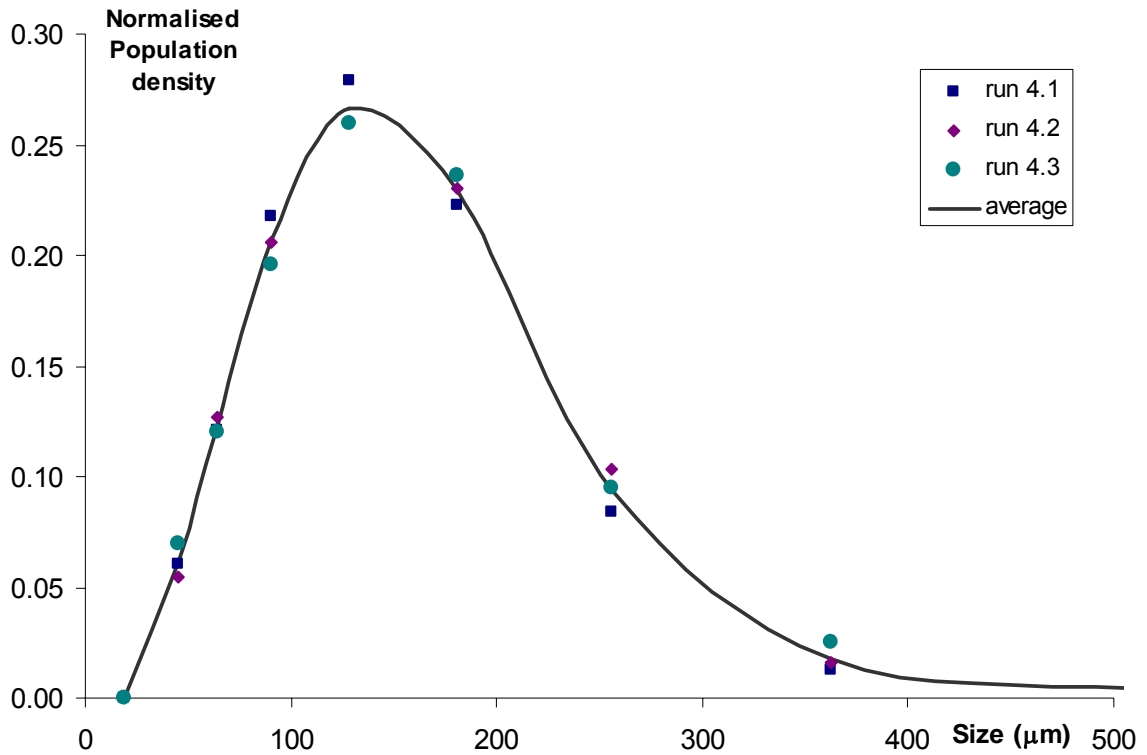


**Figure 5.12. Sieving data from runs 4.1, 4.2 and 4.3 for a cooling rate of  $-0.50\text{ }^{\circ}\text{C}/\text{min}$ , without fines removal**

The final normalized chord length distribution for the three runs in this set were averaged and used in accordance with the method detailed in Chapter IV to recover the crystal size distribution, as quantified in normalized population density. A comparison between the recovered and the experimental population density for the three runs is shown in Figure 5.13. Although slightly noisy over smaller size ranges, agreement is fairly good.

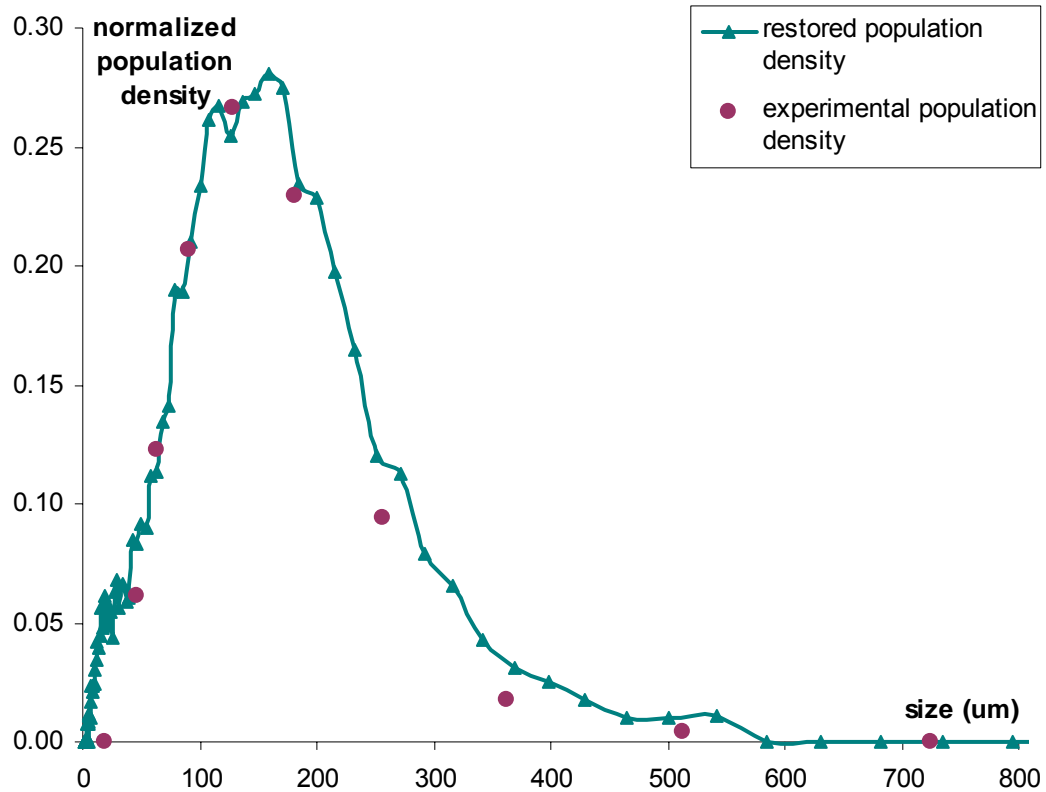


Figure 5.13. Restored and Experimental distribution for a cooling rate – 0.50 °C/min, without fines removal

## 5.2 Fines removal

The experiments described in Section 5.1 were repeated, but with the implementation of classified fines removal. As before, each experiment was repeated three times in order to insure reproducibility of the results. The collected data were averaged over the three runs for each set of experimental conditions.

### 5.2.1 Cooling Rate – 0.10 °C/min

Acetaminophen was crystallized from solutions in ethanol at a cooling rate of – 0.10 °C/min, this time with fines removal. The evolution of chord counts in Figure 5.14 contrasts in several key ways with that for the system without fine removal shown in

Figure 5.10. Again, the onset of nucleation is denoted by a rapid increase in chord counts, but only after about 8.5 hours of run time. At that point the system temperature had decreased to approximately 22 °C, which is 10 °C lower than was necessary for operation without fines removal. After increasing rapidly, the chord counts for the smaller sizes reached a maximum and then steadily diminished in the ensuing two hours. Clearly, the small crystals were being dissolved and the larger ones were growing.

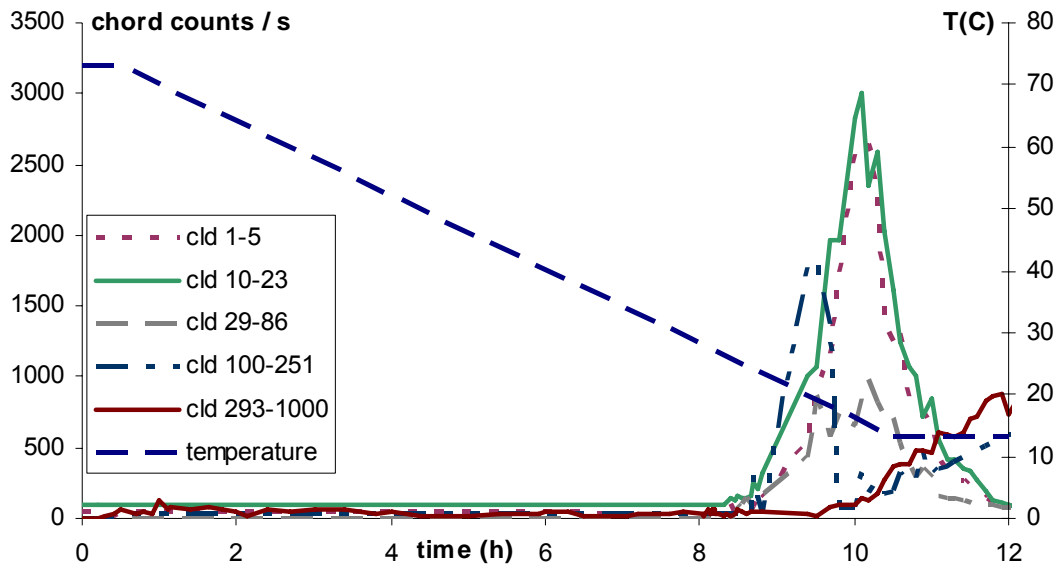


**Figure 5.14. Evolution of the chord counts and the temperature for a cooling rate of  $-0.10$  °C/min with fines removal**

The crystals were washed and dried as described. Table 5.5 shows the results of sieve analysis performed on each crystal product. From the sieve analyses, the population density was determined according to the procedure explained in Chapter III and is plotted in Figures 5.15.

**Table 5.5. Sieving results from runs with a cooling rate of  $-0.10\text{ }^{\circ}\text{C}/\text{min}$  with fines removal**

L [ $\mu\text{m}$ ]	$L_{\text{mean}}[\mu\text{m}]$	Run1.4 $\Delta\text{M}$ [g]	Run1.5 $\Delta\text{M}$ [g]	Run1.6 $\Delta\text{M}$ [g]
1000				
850	925	17.53	8.37	3.58
600	725	12.73	14.68	11.07
425	512.5	2.99	5.15	9.51
300	362.5	1.09	8.48	7.79
212	256	0.59	1.97	1.81
150	181	0.18	0.33	0.32
106	128	0.06	0.04	0.04
75	90.5	0.03	0.03	0.01
53	64	0.02	0.01	0
38	45.5	0.01	0	0
0	19	0	0	0

Figure 5.15 shows a fit of the normalized population density to the sieve data from Runs 1.4, 1.5, and 1.6. The runs were operated with a cooling rate of  $-0.10\text{ }^{\circ}\text{C}/\text{min}$ , with fines removal. The data from the three runs in this set generally are clustered close together, showing good run-to-run reproducibility. The means and spreads of the distributions were  $414.7 \pm 12\ \mu\text{m}$  and  $285.5 \pm 1.43\ \mu\text{m}$ , respectively. We can note an increase in the mean size by a factor 1.78 but unfortunately, the width of the distribution also rises by a factor 2.76 when compared to the run without fines removal.

The distribution in Figure 5.15 does not show the same bimodality as that exhibited in runs without fines removal. Presumably, this is because the fines removal system reduced the fraction of fine particles that cause the bimodality. While two of the data sets obtained were comparable, the third one was quite dissimilar and doesn't appear in the exploitation of the results.

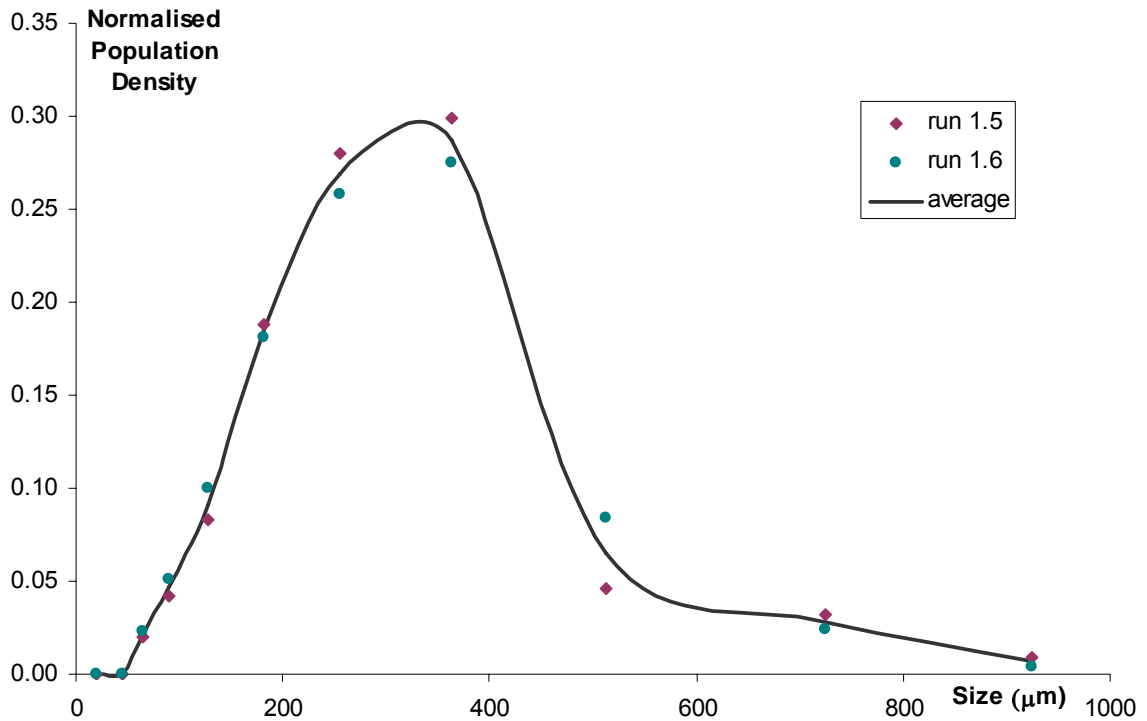


**Figure 5.15. Sieving data from runs 1.4, 1.5 and 1.6 for a cooling rate of  $-0.10\text{ }^{\circ}\text{C}/\text{min}$ , with fines removal**

The final normalized chord length distribution for the two remaining runs were averaged and used in conjunction with the method outlined in Chapter IV to recover the crystal size distribution, as quantified in normalized population density. A comparison between the recovered population density and the experimental values for the three runs is shown in Figure 5.16.

We can observe that the restored CSD is really noisy; this is due to the fact that the CLD raw data given by the FBRM for this data set were somewhat noisy. The restoration process increases that noise. The restored population density is in agreement with the sieving experiments, but the noise “shadows” this agreement.

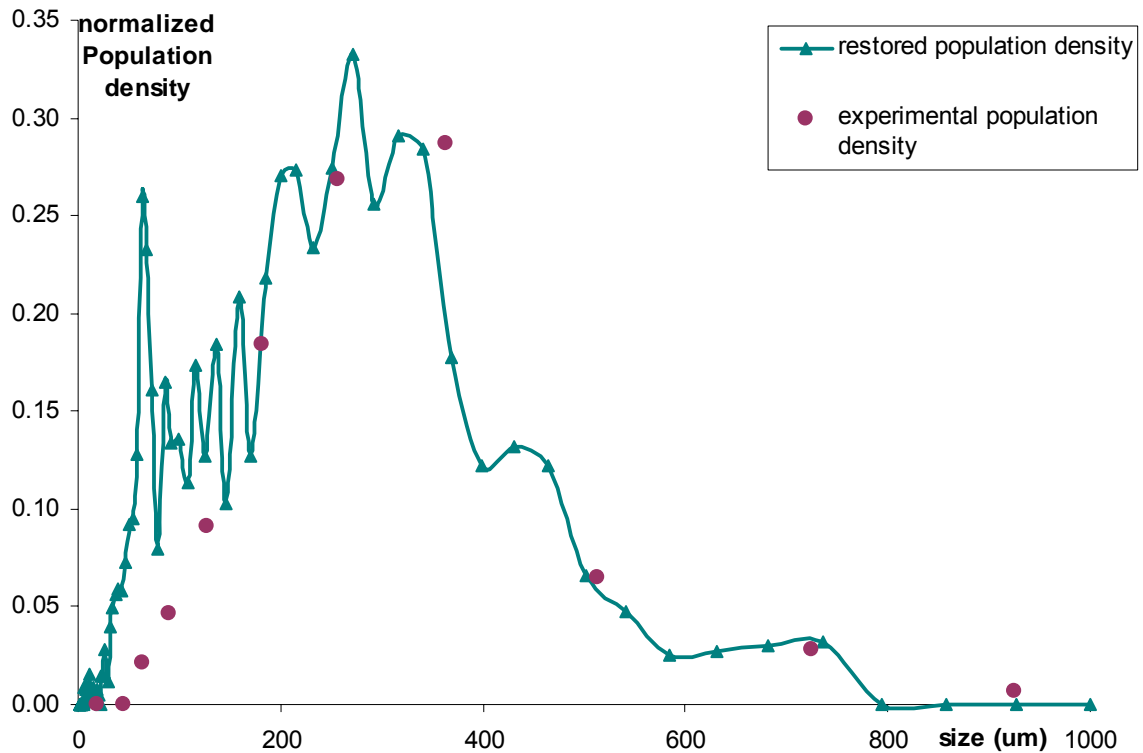


**Figure 5.16. Restored and Experimental distribution for a cooling rate – 0.10 °C/min, with fines removal**

### 5.2.2 Cooling rate – 0.20 °C/min

The crystallization was realized this time at a cooling rate of – 0.20 °C/min with fines removal. The evolution of chord counts in Figure 5.17 is to be put in parallel with that for the system without fine removal shown in Figure 5.5. Again, a rapid increase in chord counts distinctively marked the onset of nucleation after about 6.1 hours of run time. The slurry temperature had then decreased to approximately 13 °C, which is lower than the value the temperature reached when the set-up was operated without fines removal. The FBRM only detects particles greater than 1  $\mu\text{m}$ , and the presence of the fines removal system apparently delayed their detection by dissolving small crystals. After rising sharply, the chord counts for the smaller particles reached a maximum and

then steadily decreased in the following hours. Again, the small crystals were being dissolved and the larger ones were growing.

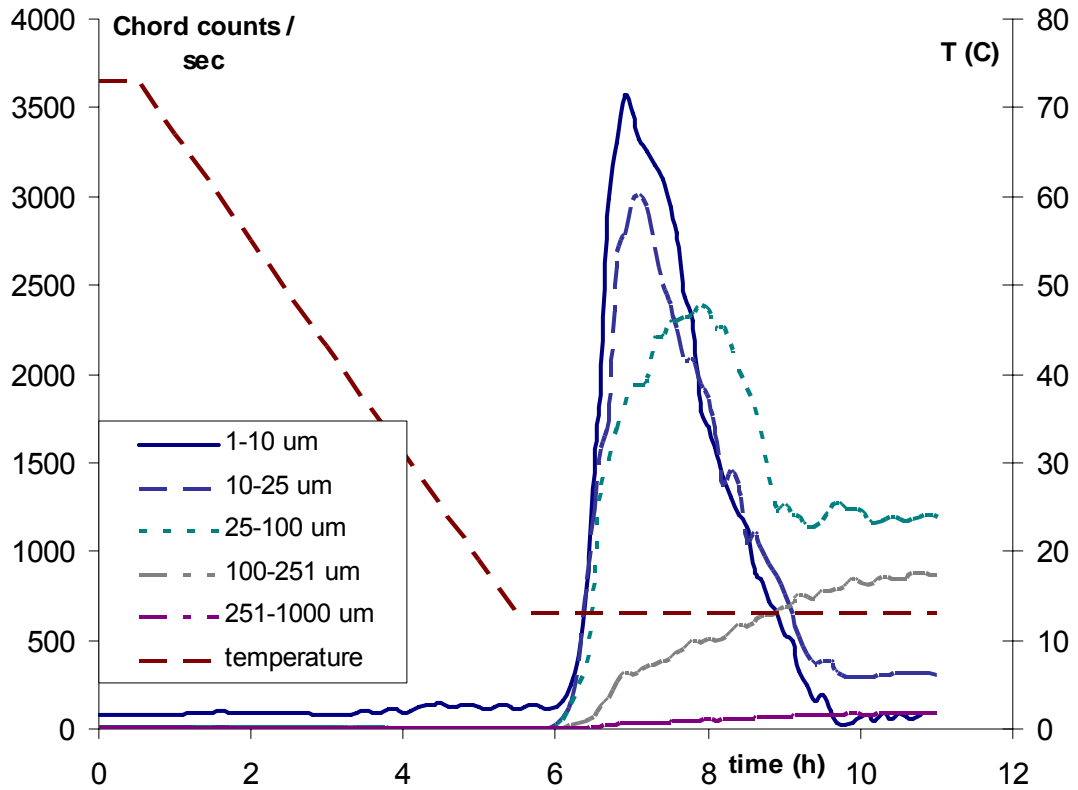


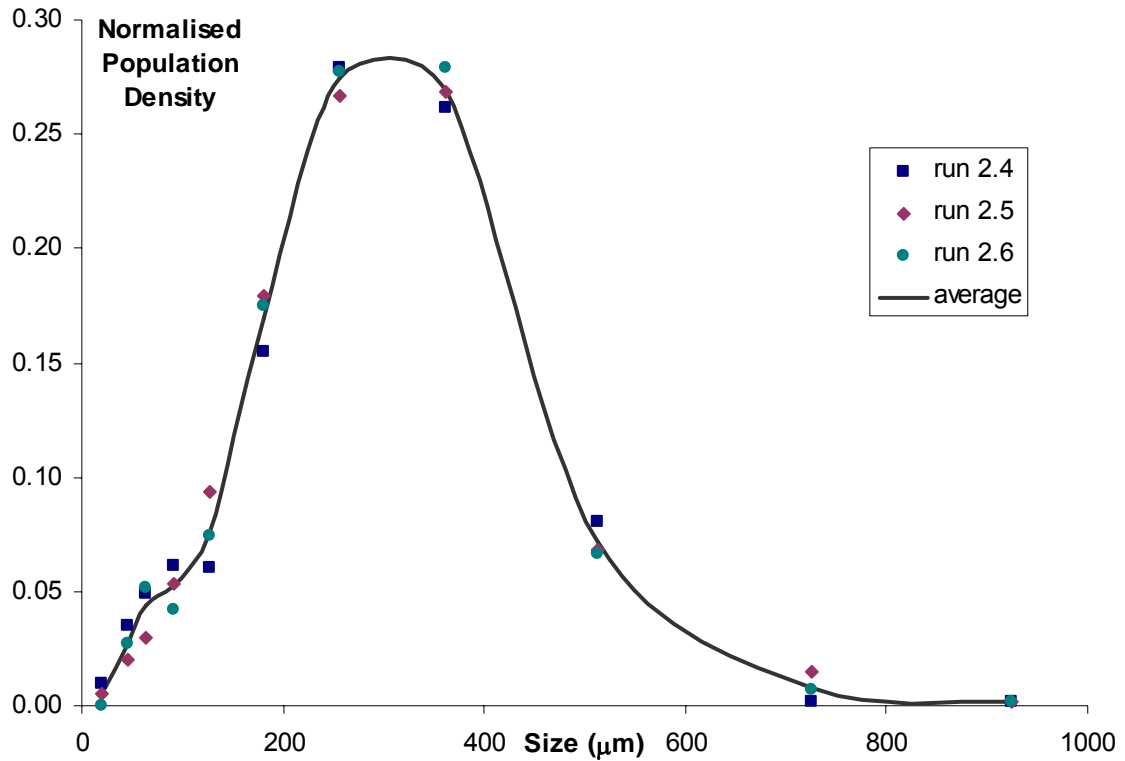
**Figure 5.17. Evolution of the chord counts and the temperature for a cooling rate of  $-0.20\text{ }^{\circ}\text{C}/\text{min}$  with fines removal**

The crystals were washed and dried as previously described. Table 5.6 display the results of the sieve analyses carried out after each experiment. Each sieve was then weighted and the population density was established according to the procedure described in Chapter III and is plotted in Figure 5.18.

**Table 5.6. Sieving results from runs with a cooling rate of  $-0.20$  °C/min with fines removal**

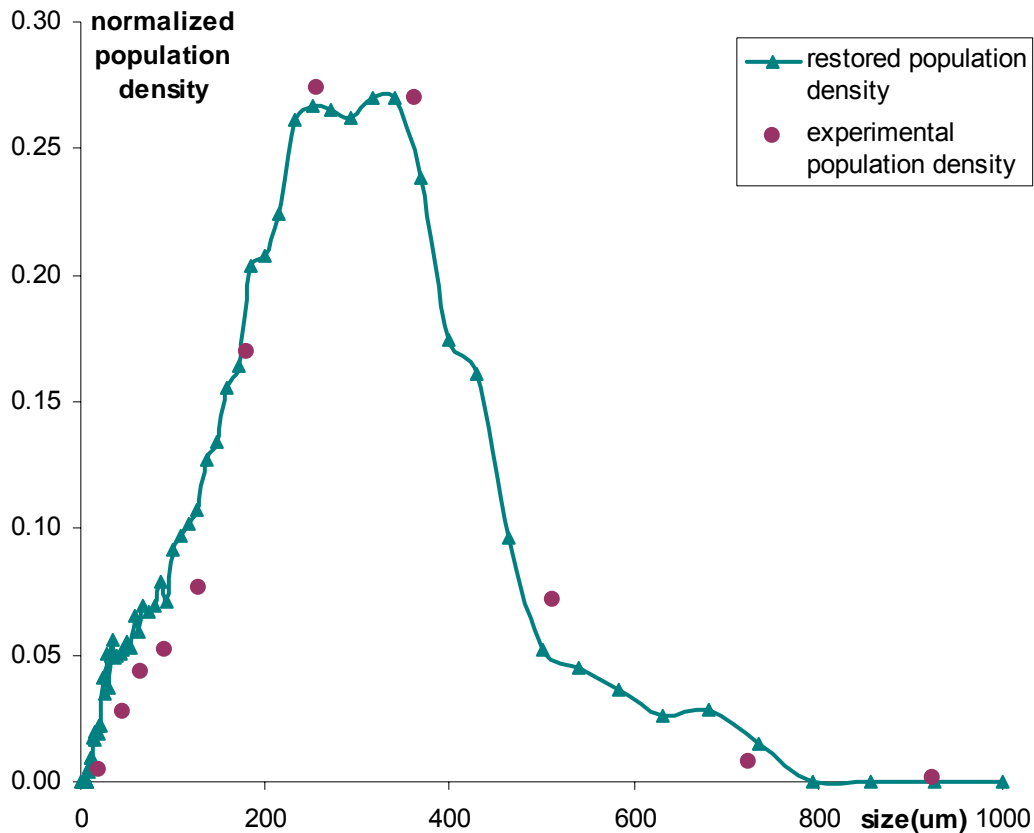
L [ $\mu\text{m}$ ]	$L_{\text{mean}}$ [ $\mu\text{m}$ ]	Run2.4 $\Delta\text{M}$ [g]	Run2.5 $\Delta\text{M}$ [g]	Run2.6 $\Delta\text{M}$ [g]
1000				
850	925	1.76	1.59	1.55
600	725	0.88	6.85	3.13
425	512.5	10.91	7.71	7.50
300	362.5	8.90	7.61	7.90
212	256	2.36	1.87	1.95
150	181	0.33	0.32	0.31
106	128	0.13	0.04	0.03
75	90.5	0.06	0.02	0.01
53	64	0.02	0.01	0
38	45.5	0	0	0
0	19	0	0	0

Figure 5.18 shows a fit of the normalized population density to the sieve data from Runs 2.4, 2.5, and 2.6. The runs were operated with a cooling rate of  $-0.20$  °C/min, but this time with fines removal. The data from the three runs are in agreement with each other, showing a good reproducibility of the experimental measurements. The means and spreads of the distributions were  $312.6 \pm 3.98$   $\mu\text{m}$  and  $136.2 \pm 0.86$   $\mu\text{m}$ , respectively. When compared to runs without fines removal, the mean size increased by a factor of 1.73, in parallel, the width of the distribution also increased by a factor of 1.65.



**Figure 5.18. Sieving data from runs 2.4, 2.5 and 2.6 for a cooling rate of  $-0.20$  °C/min, with fines removal**

The final normalized chord length distribution for the three runs in this set were averaged and used to implement the model previously described in Chapter IV to recover the crystal size distribution, as quantified in normalized population density. A comparison between the recovered and the experimental normalized population density for the three runs is shown in Figure 5.19. Although somewhat noisy over smaller size ranges (smaller bin sizes), agreement is reasonably good.



**Figure 5.19. Restored and Experimental distribution for a cooling rate – 0.20 °C/min, with fines removal**

### 5.2.3 Cooling Rate – 0.35 °C/min

The crystallization of paracetamol from ethanol solution was realized with a cooling rate of – 0.35 °C/min, with fine removal. The evolution of chord counts in Figure 5.20 offers a contrast in several key ways with that for the system without fines removal shown in Figure 5.8. Once more, the onset of nucleation is indicated by a fast augmentation in chord counts after about 4.9 hours of run time. At that point the system temperature had reached 13 °C. After increasing rapidly, the counts for the smaller sizes attained a maximum before steadily decreasing and finally reaching a constant value. The small particles were being dissolved and the larger ones were growing.

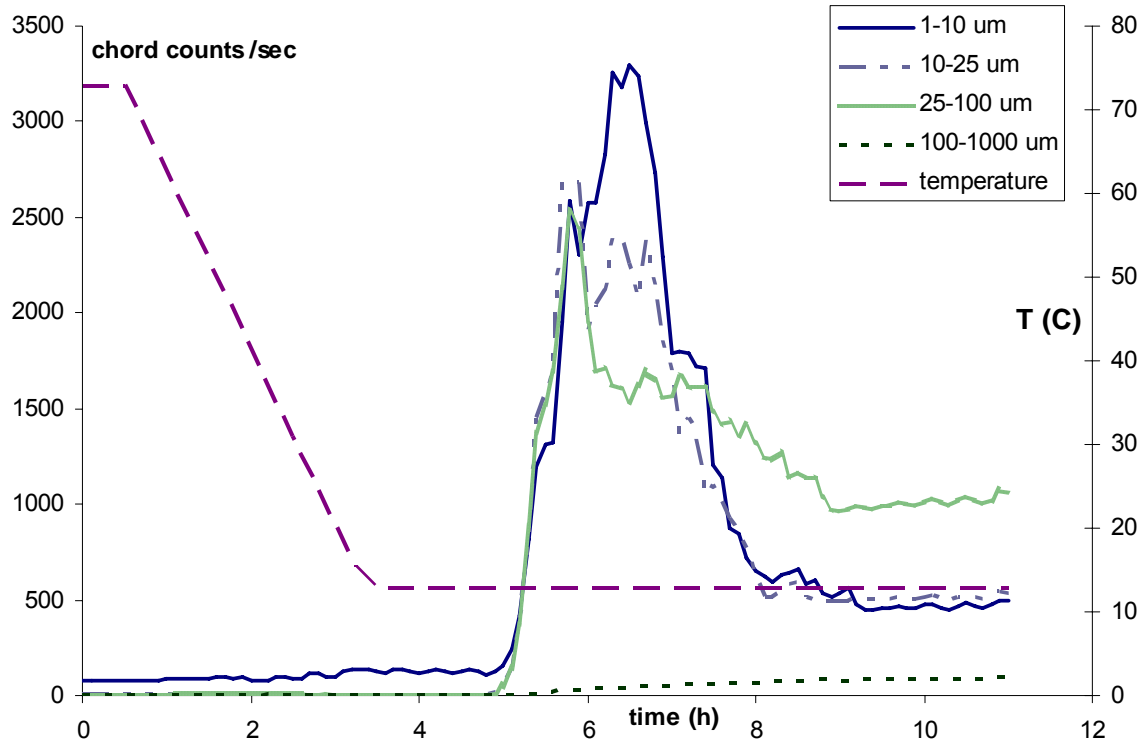


**Figure 5.20. Evolution of the chord counts and the temperature for a cooling rate of  $-0.35\text{ }^{\circ}\text{C}/\text{min}$  with fines removal**

This time again, the crystals were washed and dried according to the procedure previously described. Table 5.7 regroups the results of the size analysis realized on each crystal product. From this analysis, the population distribution was calculated according to the formulas detailed in Chapter III. The resulting population distribution is shown in Figure 5.21.

**Table 5.7. Sieving results from runs with a cooling rate of  $-0.35\text{ }^{\circ}\text{C}/\text{min}$  with fines removal**

L [ $\mu\text{m}$ ]	$L_{\text{mean}}[\mu\text{m}]$	Run3.4 $\Delta\text{M}$ [g]	Run3.5 $\Delta\text{M}$ [g]	Run3.6 $\Delta\text{M}$ [g]
1000				
850	925	2.28	3.06	2.37
600	725	5.16	4.32	3.73
425	512.5	11.56	4.76	4.11
300	362.5	12.73	10.75	10.28
212	256	3.21	11.33	11.08
150	181	1.19	2.12	3.04
106	128	0.25	0.93	0.11
75	90.5	0.04	0.06	0.05
53	64	0.01	0.02	0.01
38	45.5	0	0.01	0
0	19	0	0	0

Figure 5.21 shows a fit of the normalized population density to the sieve data from Runs 3.4, 3.5, and 3.6. The runs were operated with a cooling rate of  $-0.35\text{ }^{\circ}\text{C}/\text{min}$ , with fines removal. The data are reproducible. The means and spreads of the distributions were  $253.6 \pm 3.26\ \mu\text{m}$  and  $111.8 \pm 0.96\ \mu\text{m}$ , respectively. The mean size rose by a factor of 1.65 and the width of the distribution also increased by a factor of 1.74 when the results are contrasted with the runs without fines removal.

In the distribution in Figure 5.21, a small disturbance is observed for the small size most likely due to the breakage of some big particles.

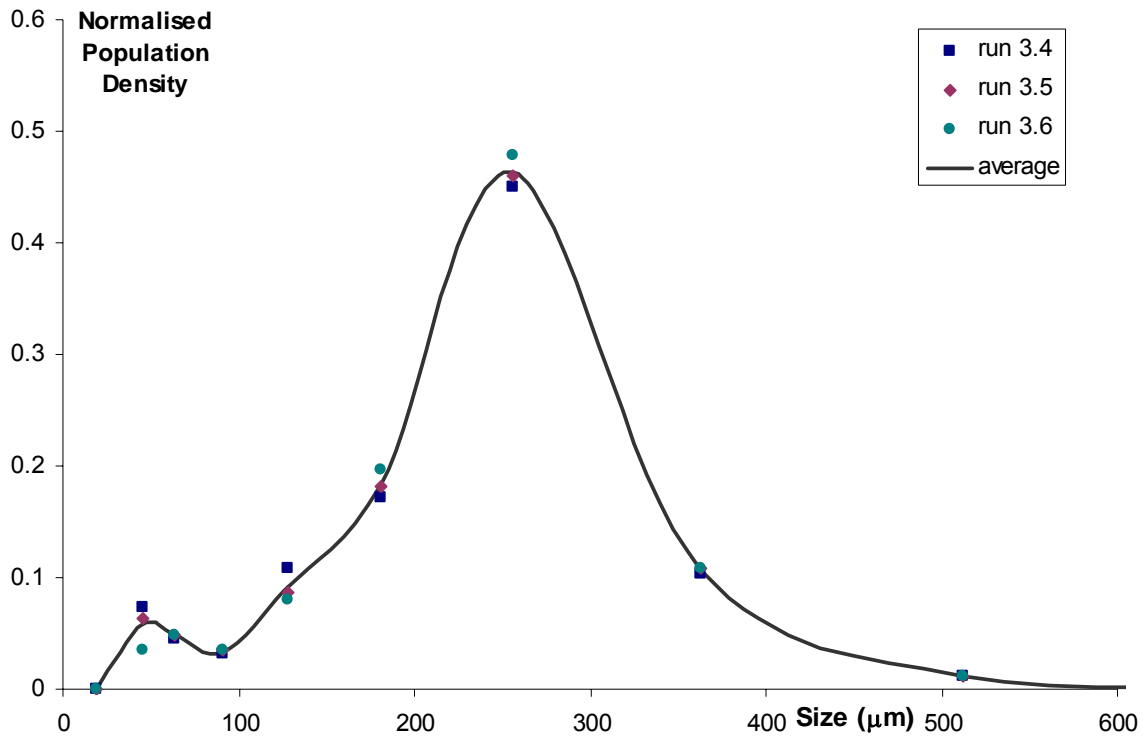


**Figure 5.21. Sieving data from runs 3.4, 3.5 and 3.6 for a cooling rate of  $-0.35\text{ }^{\circ}\text{C}/\text{min}$ , with fines removal**

The final normalized chord length distribution for the three runs in this set were averaged and used according to the method outlined in Chapter IV to recover the crystal size distribution, as quantified in normalized population density. A comparison between the recovered population density and the experimental values for the three runs is shown in Figure 5.22.

Once again, we are faced with a noisy restored CSD, this is due to the fact that the experimental CLD raw data is not “smooth”. The model increases that noise when implementing the calculation for the computation of the restored CSD.

The agreement with the sieving experiments is not as good as in the previous runs. This might have several causes. It might be due to the method of recovery of the crystals (collection from the slurry, washing and drying), which can affect the experimental distribution; it might be also due to the recovery method which introduces

noise in the recovered distribution, thus weakening the accuracy of the restored distribution.

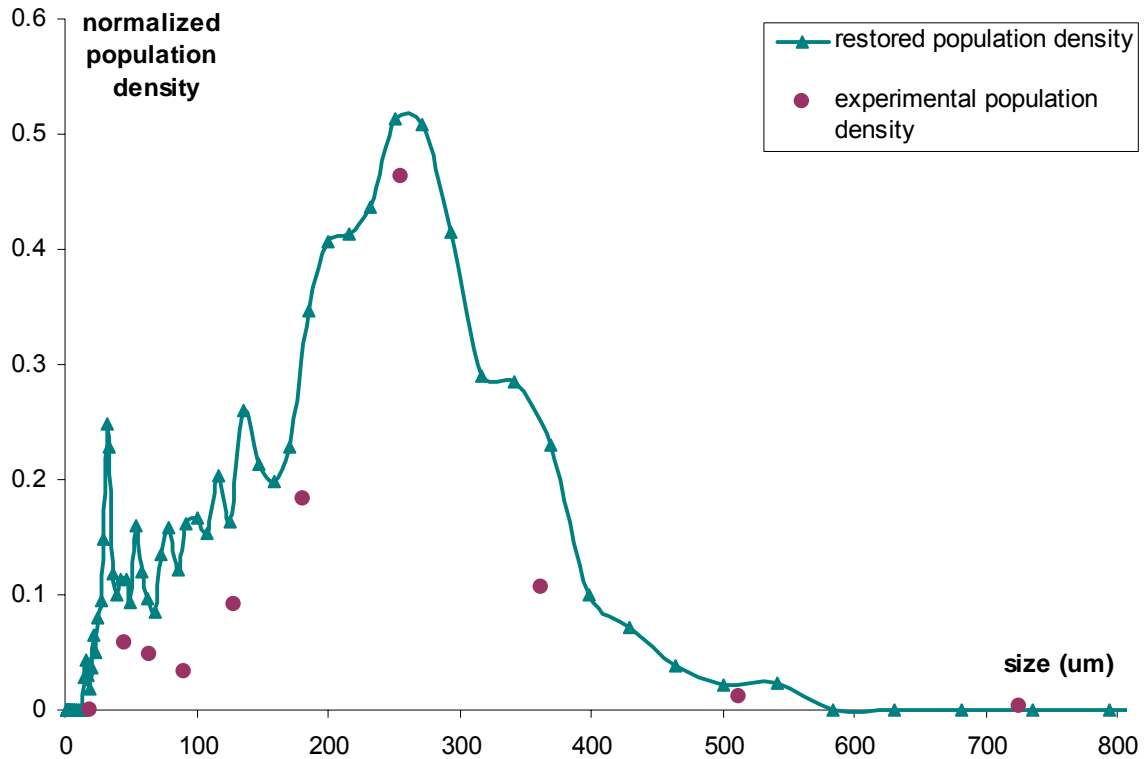
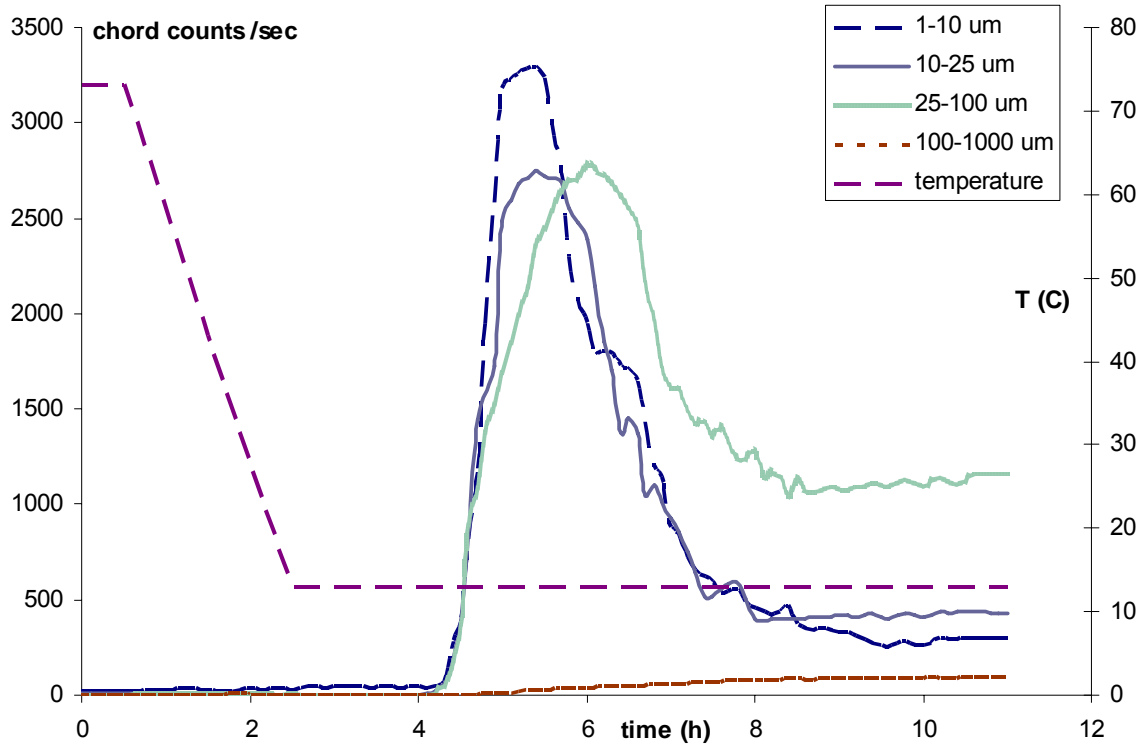


Figure 5.22. Restored and Experimental distribution for a cooling rate – 0.35 °C/min, with fines removal

#### 5.2.4 Cooling Rate – 0.50 °C/min

The crystallization was realized here for a cooling rate of – 0.50 °C/min, with fine removal. This evolution of the chord counts in Figure 5.23 is to be contrasted by the evolution of the system without fines removal shown on Figure 5.11. The onset of nucleation is still noticeable by a sharp increase in the counts; the temperature read is 13 °C. The same behavior is observed in all the runs with fines removal, the counts for

small particles increased then decreased thus allowing bigger particles to grow. A little after 8 hours run time, steady state is completed.



**Figure 5.23. Evolution of the chord counts and the temperature for a cooling rate of  $-0.50\text{ }^{\circ}\text{C}/\text{min}$  with fines removal**

As usual, the crystals obtained were washed and dried before being classified by a sieving process. Table 5.8 shows the results of the sieve analysis performed after each experiment. The population was then determined according to the formula explained in Chapter III and is shown in Figure 5.24. Once again the three populations are clustered together, showing reproducibility of the system.

**Table 5.8. Sieving results from runs with a cooling rate of – 0.50 °C/min with fines removal**

L [ $\mu\text{m}$ ]	L <sub>mean</sub> [ $\mu\text{m}$ ]	Run5.4 $\Delta\text{M}$ [g]	Run5.5 $\Delta\text{M}$ [g]	Run5.6 $\Delta\text{M}$ [g]
1000				
850	925	1.72	0	0
600	725	6.42	6.44	9.05
425	512.5	7.22	7.01	7.33
300	362.5	8.03	11.03	7.53
212	256	7.35	8.72	8.61
150	181	3.89	3.35	3.56
106	128	1.36	0.38	0.67
75	90.5	0.34	0.04	0.03
53	64	0.09	0.02	0.01
38	45.5	0.01	0	0
0	19	0	0	0

Figure 5.24 shows a fit of the normalized population density to the sieve data from Runs 4.4, 4.5, and 4.6. The runs were operated with a cooling rate of – 0.50 °C/min, but with fines removal. The experimental data from the three runs are concurring, thus showing good reproducible measurements. The means and spreads of the distributions were  $227.1 \pm 3.48 \mu\text{m}$  and  $105.8 \pm 0.78 \mu\text{m}$ , respectively. The mean size increased by a factor of 1.60 but as in the other runs, the width of the distribution also rose by a factor of 1.81 when the results for the runs with and without fines removal are put in parallel.

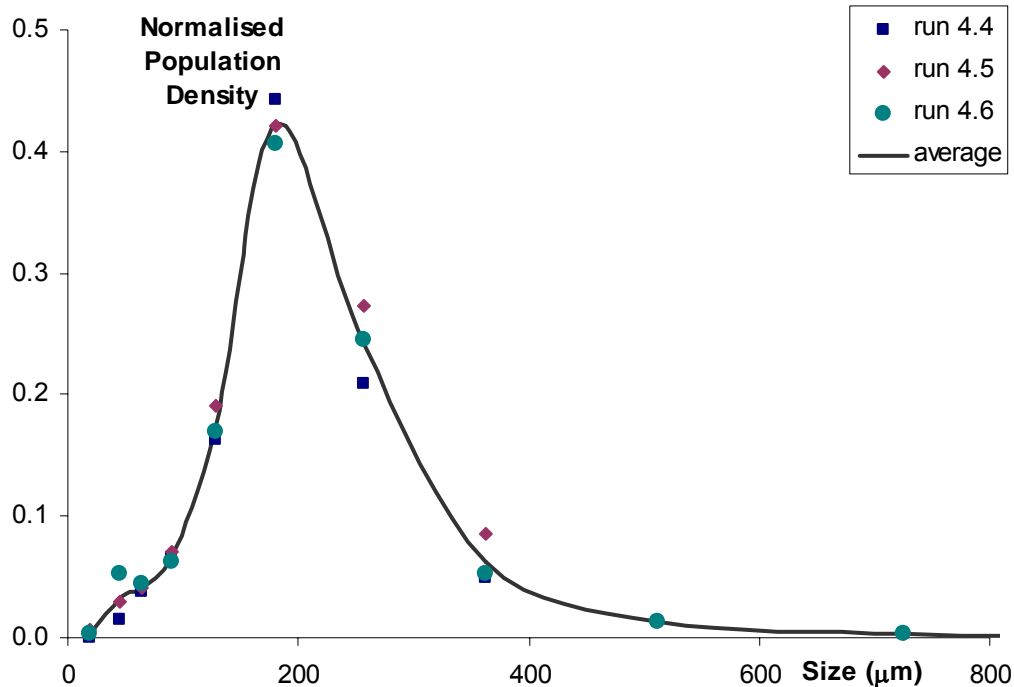


Figure 5.24. Sieving data from runs 4.4, 4.5 and 4.6 for a cooling rate of  $-0.50\text{ }^{\circ}\text{C}/\text{min}$ , with fines removal

The final normalized chord length distribution for the three runs in this set were averaged and used in conjunction with the method outlined in Chapter IV to recover the crystal size distribution, as quantified in normalized population density. A comparison between the recovered population density and the experimental values for the three runs is shown in Figure 5.25. Although somewhat noisy over smaller size ranges, agreement is reasonably good.

It is interesting to note that the experimental CLD obtained when the fines removal system is implemented are noisier than when this system is inactivated.

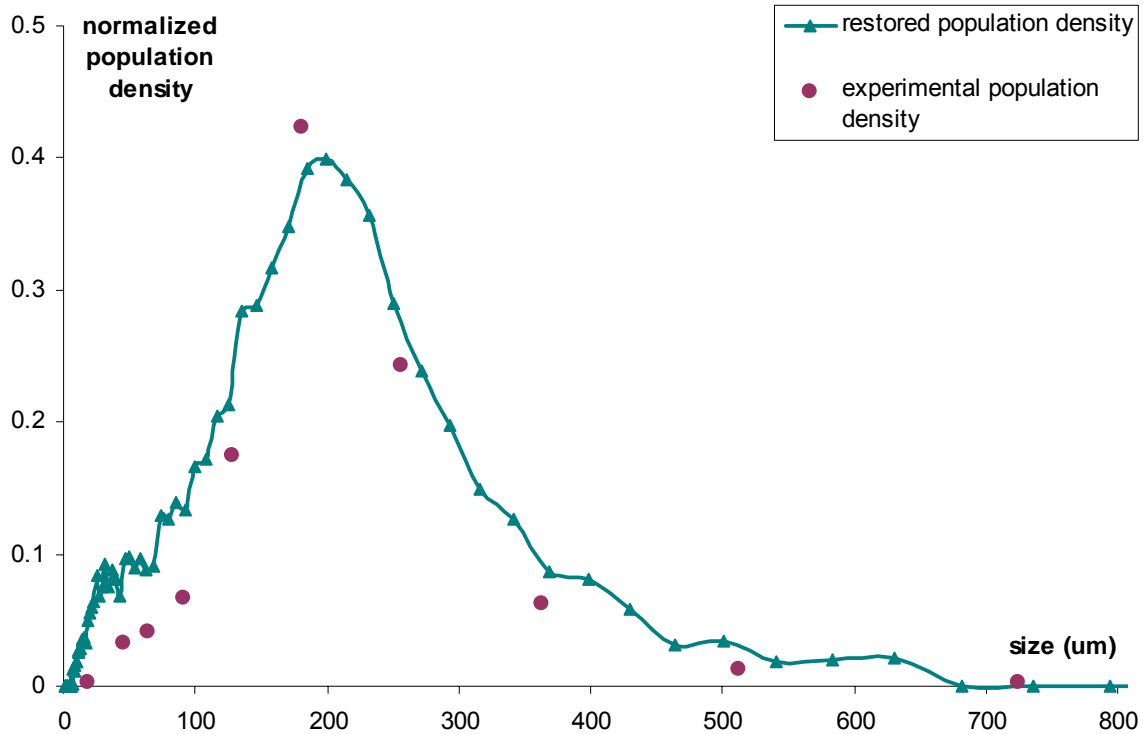


Figure 5.25. Restored and Experimental distribution for a cooling rate – 0.50 °C/min, with fines removal

### 5.3 Analysis of the Product

The purity of the paracetamol crystallized was checked using IR and X-ray diffraction. The results are shown below in Figures 5.26 and 5.27 for X-ray diffraction and Figures 5.28 and 5.29 for IR spectroscopy.

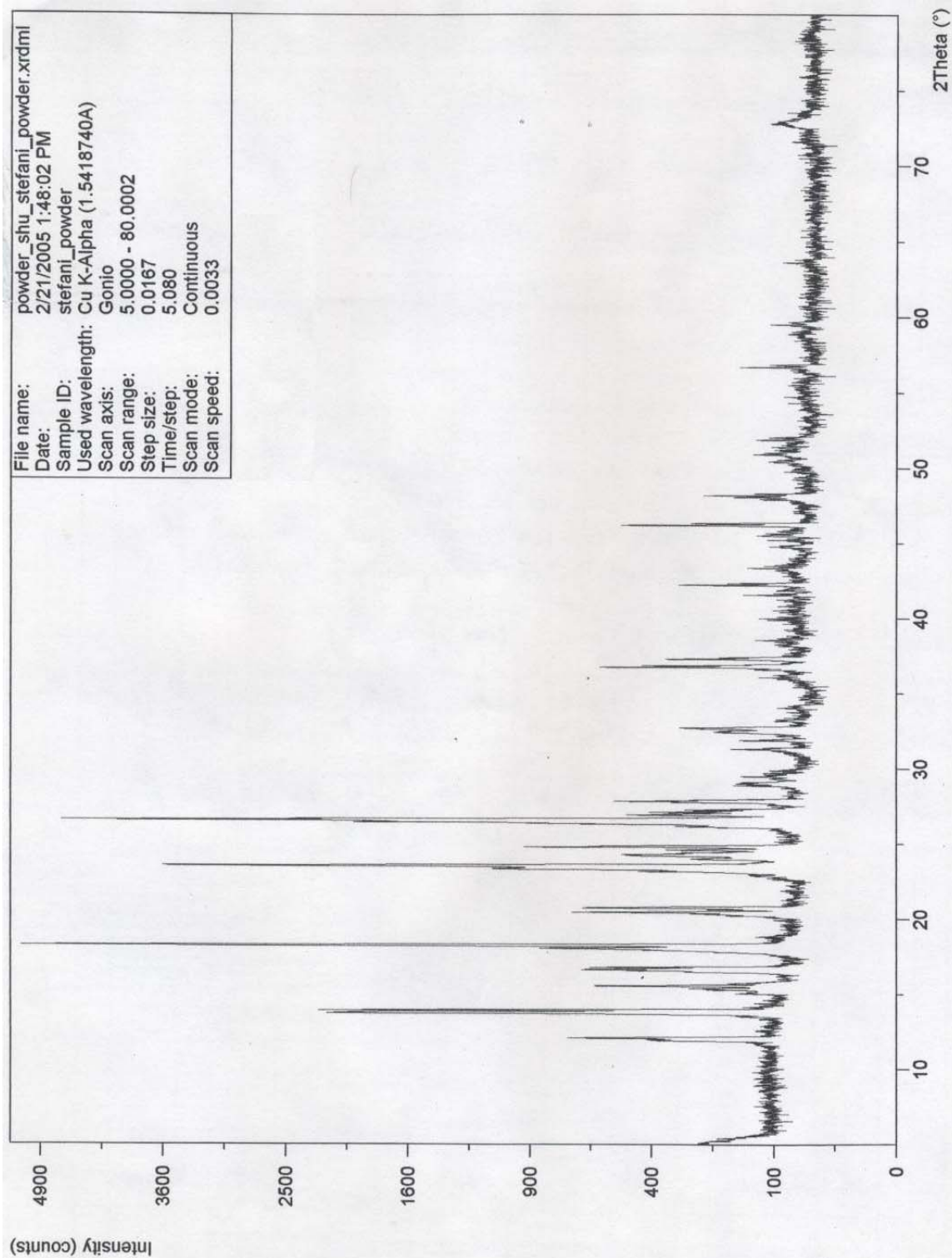
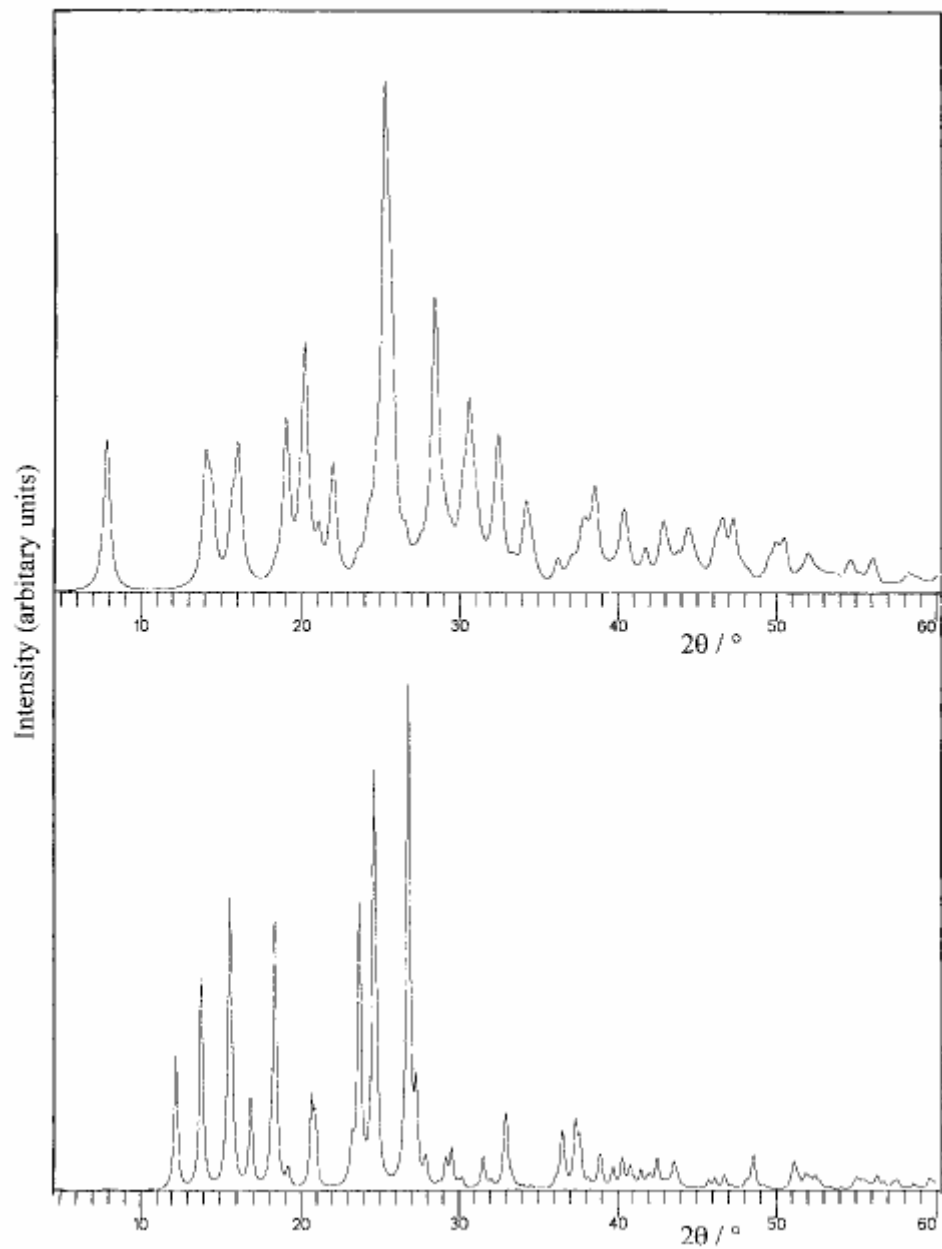


Figure 5.26. X-ray diffraction, experimental result



**Figure 5.27. Powder diffraction pattern obtained for paracetamol trihydrate (upper plot) compared with the one of monoclinic paracetamol (lower plot) (Journal of pharmaceutical sciences, vol 91, no 5, may 2002)**

X-ray diffraction is a technique widely used to obtain information on the lattice of a given crystal. By comparing the experimental XRD spectrum to the spectrum found in the literature, respectively displayed in Figures 5.26 and 5.27, we can see that the paracetamol crystallized is pure and crystallizes in the monoclinic lattice, the peaks are overlapping.

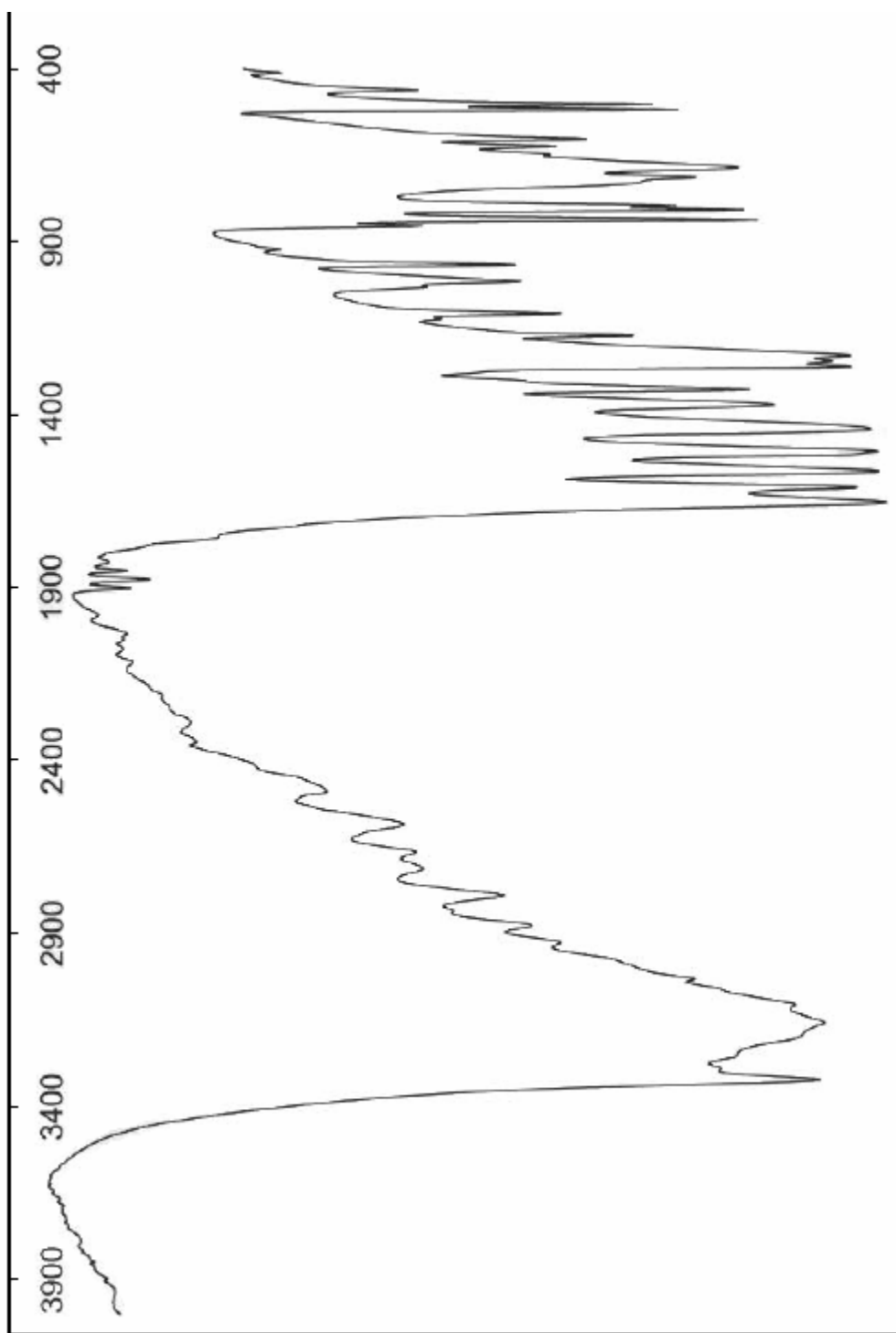
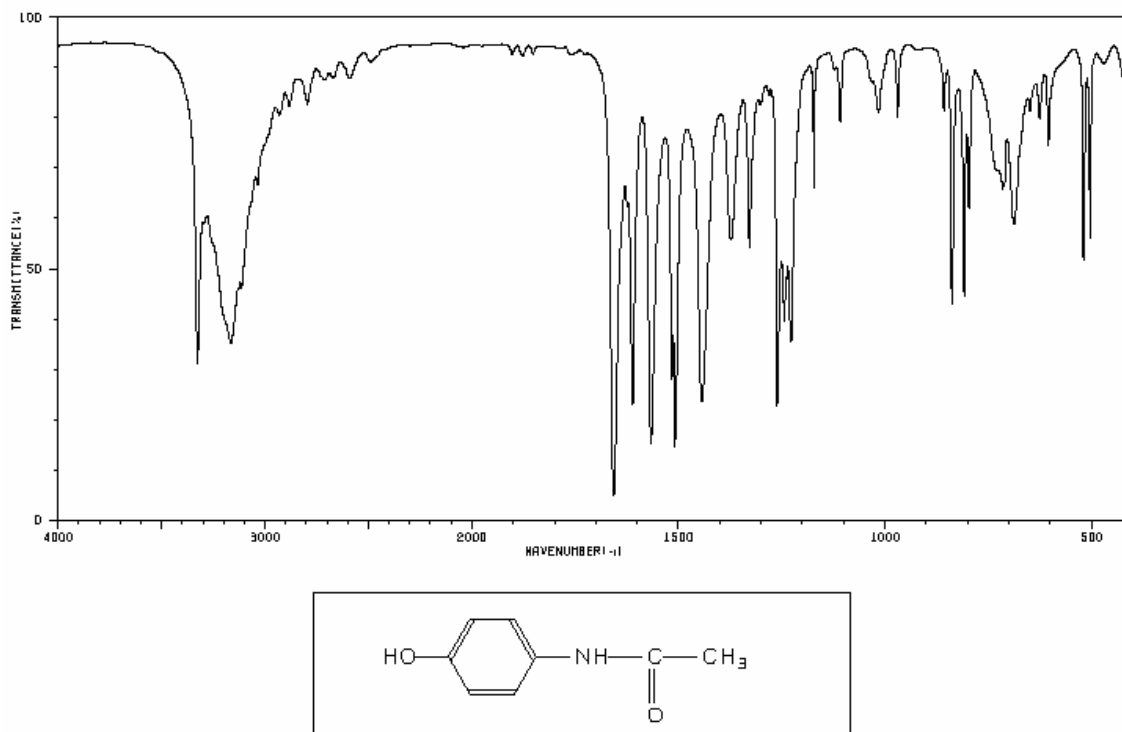


Figure 5.28. IR spectroscopy, experimental spectrum, KBr disc



**Figure 5.29. IR spectroscopy, theoretical spectrum, KBr disc (NIST Webbook)**

IR Spectroscopy is a spectroscopic technique that gives information on the structure of the molecule and can also be used to identify the functional groups of a molecule. The peaks giving information on the structure of the compounds are:

3100  $\text{cm}^{-1}$  OH H-bond linked stretch

1173, 1373  $\text{cm}^{-1}$ : OH bending

3300  $\text{cm}^{-1}$ : NH stretch

1667  $\text{cm}^{-1}$ : NH bending

3030  $\text{cm}^{-1}$ : CH stretch

2000-1667  $\text{cm}^{-1}$  Overtones or band pattern indicative of para-substituted aromatic

1611-1587-1516-1444  $\text{cm}^{-1}$  : benzene ring, stretch C=C aromatic

858  $\text{cm}^{-1}$  : aromatic CH bend para-substituted ring

1624  $\text{cm}^{-1}$ : C=O stretch conjugated

1329  $\text{cm}^{-1}$ : CN stretch

Conjugation in the molecule causes some bonds to vibrate at a lower frequency than expected for so peaks and with an increased intensity. By contrasting the experimental spectrum and the one given in the literature, those spectrum are respectively shown in Figure 5.28 and 5.29, we can see that the characteristics peaks are presents in both spectrum and that the paracetamol crystallized is pure. The peak appearing around 3100  $\text{cm}^{-1}$  would be broader if ethanol was present in the crystal.

A picture of the crystals was also taken under the microscope in order to make sure of the octahedral shape. It is clearly seen on Figures 5.30 and 5.31 that the assumption of an octahedral shape was realistic, thus the geometric shape on which the model detailed in Chapter III was justified.

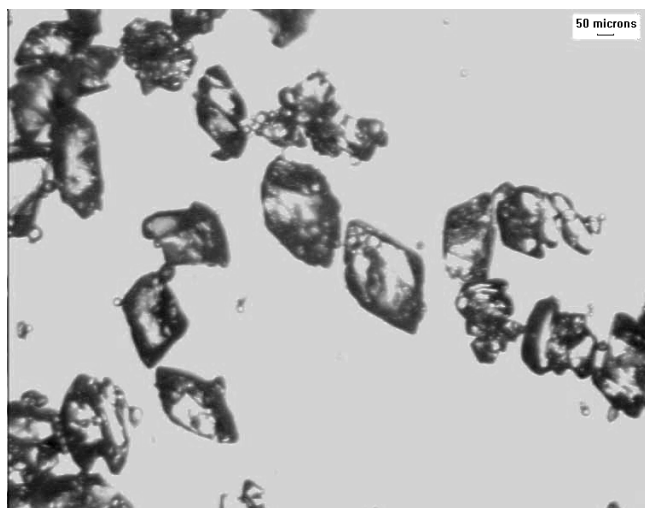


**Figure 5.30. Microscope pictures of paracetamol crystals (\*4)**

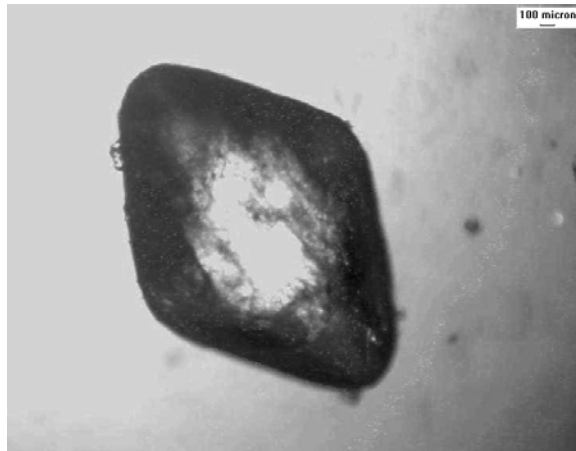


**Figure 5.31. Zoom on a paracetamol crystal (\*10)**

## CHAPTER VI

### DISCUSSION

The spectroscopic study of the crystals obtained confirmed the crystallization of a pure compound in a monoclinic lattice. The microscope confirms the octahedral shape on which the modelization is based.

Three runs were performed at each set of conditions; i.e., at several cooling rates and with or without fines removal. The mean sizes from runs at a set of conditions varied less than 2%, while the spread of the distribution ( $\sigma$ ) varied less than 1%. Such results show that the runs were repeated with good reproducibility. Averaged results for all runs are given in Table 6.1.

Comparison of the sieve analyses from three experiments, as exposed by Figure 6.1., at a cooling rate of  $-0.10^{\circ}\text{C}/\text{min}$  show the impact of fines removal; with fines removal, the mean size was  $414.5\ \mu\text{m}$  and the standard deviation,  $\sigma$ , was  $202.1\ \mu\text{m}$ , while corresponding values without fines removal were  $232.5\ \mu\text{m}$  and  $103.3\ \mu\text{m}$ . In other words, the mean size increased by nearly a factor of two, although this positive result was partially offset by the numerically larger spread in the distribution. Similar observations are drawn from experiments at different cooling rates and with or without fines removal.

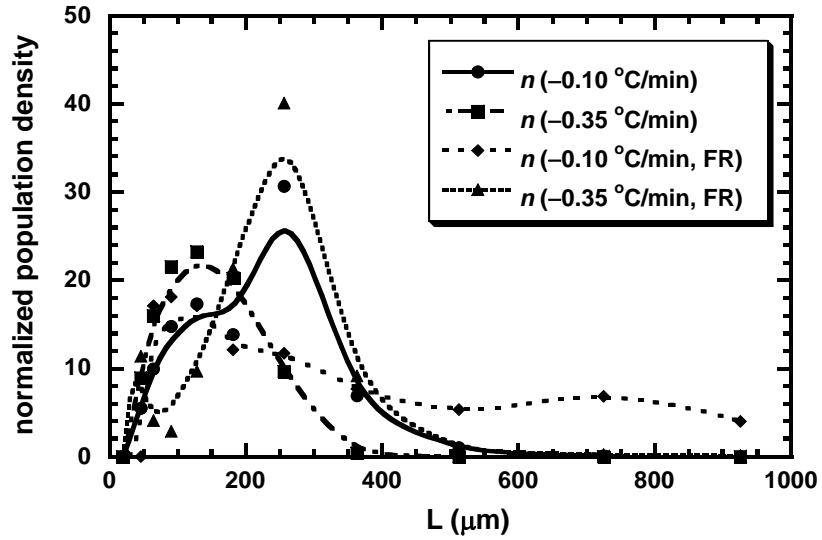


Figure 6.1. Sieve analyses of product size distributions at two cooling rates and no fines removal.

In addition to providing the average size and the spread of the size distribution, Table 6.1 also gives the conditions at which nucleation was indicated by the sudden increase in chord-length counts. The implementation of fines removal increased the time between the observation of nucleation and the time at which the system reached saturation.

**Table 6.5. Summary of the results**

<b>Cooling rate (°C/min)</b>	<b>Fines removal</b>	<b><math>t_{\text{sat}}</math> (min)</b>	<b><math>T_{\text{sat}}</math> (°C)</b>	<b><math>t_{\text{nuc}}</math> (min)</b>	<b><math>T_{\text{nuc}}</math> (°C)</b>	<b><math>t_{\text{run}}</math> (h)</b>	<b><math>L_{\text{avg}}</math> (<math>\mu\text{m}</math>)</b>	<b><math>\sigma</math> (<math>\mu\text{m}</math>)</b>
- 0.10	Yes	259.5	50.05	482	28	11	414.5	202.1
- 0.10	No	259.5	50.05	391	38	11	232.5	103.3
- 0.20	Yes	144.8	50.05	366	13	11	312.6	136.2
- 0.20	No	144.8	50.05	309	18	11	180.8	82.6
- 0.35	Yes	95.6	50.05	333	13	11	253.7	111.8
- 0.35	No	95.6	50.05	221	13	11	155.5	71.2
- 0.50	Yes	75.9	50.05	261	13	11	227.1	105.8
- 0.50	No	75.9	50.05	240	13	11	141.5	58.4

Figure 6.1 shows normalized population densities for runs in which the system was operated with and without fines removal and at two different cooling. It is interesting to note that without fines removal the size distribution was bimodal when the cooling rate was  $- 0.10$  °C/min, but unimodal and exhibiting a smaller mean for a cooling rate of  $- 0.35$  °C/min. The figure also shows that implementation of fines removal led to larger crystal sizes but significantly wider distributions. The bimodal character of the population density was diminished as the cooling rate was increased. This behavior was accompanied by a continued decrease in mean size.

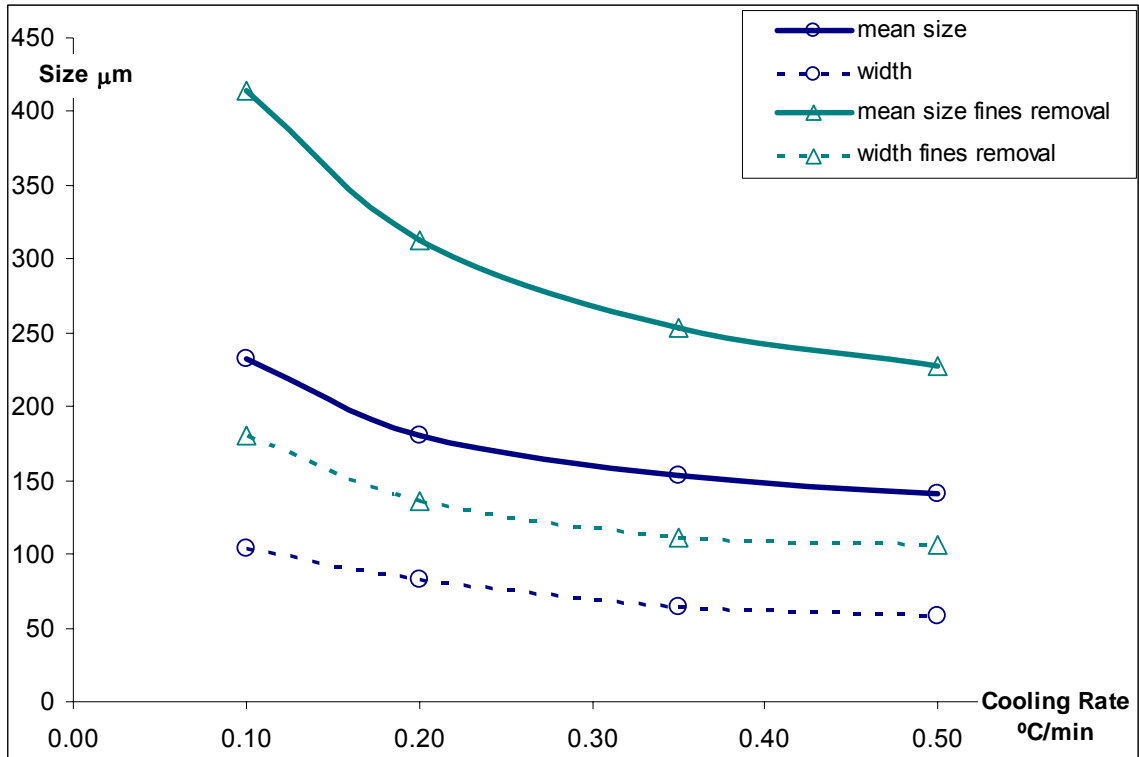


**Figure 6.2. Evolution of the mean and the width in function of the condition of operations**

Figure 6.2 illustrates how the mean size and the width of the distribution varied with the cooling rate used in a run. The behaviors were similar, irrespective of whether or not the system was operated with fines removal. Clearly, the cooling rate had a significant influence on both mean size and spread of the distribution; as the cooling rate decreased, the mean size increased, but unfortunately the width of the distribution increased as well. Although the same dependence on cooling rate was observed with or without fines removal, the use of fines removal increased the mean size, but again with a greater spread in the distribution.

The model seems to give overall a pretty good approximation of the real population but due to the noise of the CLD raw data, the recovered distributions are noisy. We can note that the model increases this character. Nonetheless, the results from the sieving experiments are in agreement with the restored CSD.

Errors might have been introduced in the system during the experiments or during the restoration of the CSD. Considering the fact that the crystals were manipulated several times before the actual sieving, the population might have been altered, for example, some fine crystals might have been lost, some bigger ones might have been broken. Another source of mistake can come from the restoration method, as the matrix cannot be accurately inverted; we use a technique that minimizes the norm of the matrix  $A$ .

## CHAPTER VI

### CONCLUSION

The FBRM is a useful tool in monitoring the progression of crystal size distributions in batch crystallization via the display and the monitoring of the evolution of the chord-length distribution. The results from the experiments in the present study show how the measured CLD evolves during a run, and they illustrate the impacts of preferential fines removal on the product crystal size distribution, which is to increase the mean size and unfortunately also the spread of distribution. It is also noticed that the cooling rate has a large influence on the population distribution; this parameter can be easily used to manipulate at will the mean size of the distribution. By increasing this rate, we observe a diminishing mean size and spread, nucleation occurs earlier. The onset of nucleation is clearly identified by the sudden increase in chord counts for all size ranges measured by the FBRM, but further work is required to convert this information to crystal size distributions which is conveniently convertible into commonly used mass distribution. It is possible to determine the nucleation rate by using the Lasentec technology but complete success would result in an ability to quantify as well crystal growth, thus allowing an easier modelization of the crystallization process via the use of population balances. Most importantly, the methodology has great potential to be the basis for the development of a control scheme that manipulates the crystal size distribution produced from a batch crystallizer based on the information provided in real time by the laser probe.

The use of FBRM can be undermined by the fact that it does not directly provide the crystal size distribution; the CLD monitored does not give a direct information on the CSD as there is no direct link between them. The methodology demonstrated here offers a fairly good but noisy restoration of the CSD. This model can be applied to a wide range of particles and is mostly a function of their geometry. Nonetheless the simulations needed to implement such model are time consuming thus making its application to more complex geometry a long and complex process. A possible development for Mettler Toledo, that distributes the FBRM would be to establish a database regrouping the conversions matrices for the basic crystals shape or even better to add to their software a program which directly converts the CLD onto the CSD.

## APPENDIX A

### CALIBRATION CURVE FOR THE MINI PERISTALTIC METERING PUMP



These small pumps are used for low-flow, low-pressure applications such as liquid chromatography, circulating fluids, and moving corrosive material. The flow varies with the speed control and by using tubing with different Internal Diameters. The pump was used with silicone tubes of 3/16" ID, fittings and nipples are polypropylene.

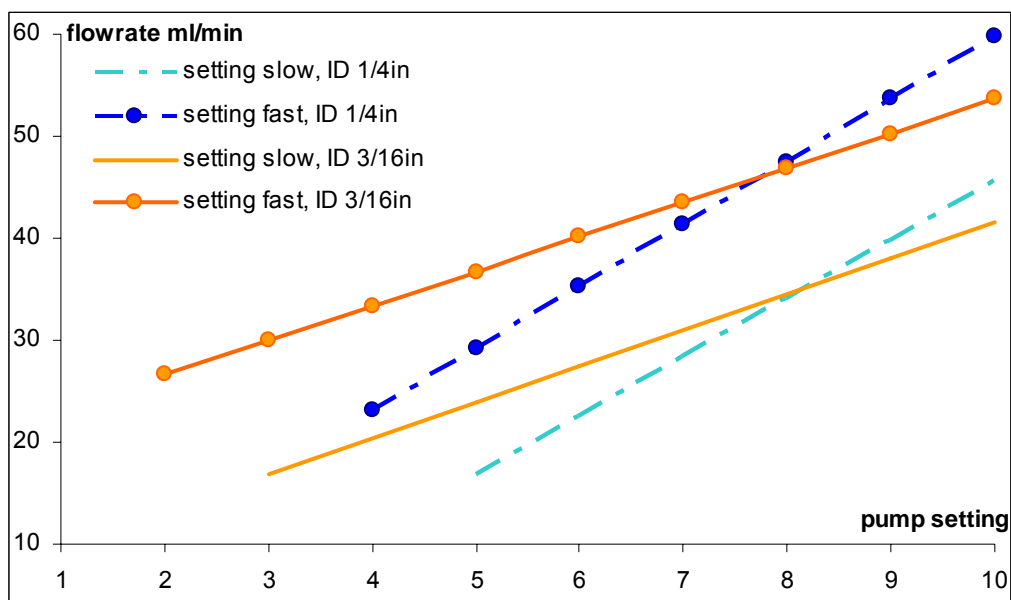


Figure A.1. Calibration curve of the mini peristaltic pump

## APPENDIX B

### IMPLEMENTATION OF THE FINES REMOVAL SYSTEM

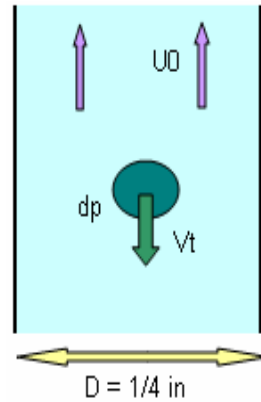


Figure B.1. Modelization of the trap

The flow rate  $Q$  is 20 ml/min, the internal diameter is  $3/16''$ , the density of the solution is  $998.2\text{kg/m}^3$ , and the density of the particle is  $1730\text{kg/m}^3$ . The viscosity of the solution is estimated to be 1.2 cP ( $20^\circ\text{C}$ ), the acceleration due to gravity is  $9.81\text{ m}^2/\text{s}$ .

We can calculate the upward velocity 
$$U_0 = \frac{Q}{\pi(d/2)^2}$$

Then we can calculate  $Re_p$  
$$Re_p = \frac{d_p U_0 \rho}{\mu}$$

And using the Haider-Levenspiel approach, we can determine the coefficient  $C_d$  which is a function of the Reynolds number,  $C_d = f(Re_p)$  :

$$Re_p < 1000 \quad C_d = \frac{24}{Re_p} (1 + 0.51 * Re_p^{0.687})$$

$$Re_p > 1000 \quad C_d = 0.44$$

Thus the speed of settlement  $V_t$  is estimated.

$$V_t = \left( \frac{4d_p(\rho_p - \rho)g}{3\rho C_d} \right)^{1/2}$$

Then the value of  $d_p$  for which  $V_t - U_0 = 0$  is determined. The resulting calculated value is  $L_f = 126 \mu\text{m}$ .

Some approximations were made regarding the data (average values over the temperature range for example), thus this is just an estimation of the dimension of the particles removed. Due to breakage, and slight dissolution of bigger particle, we still observe some smaller crystals but this amount is limited.

## APPENDIX C

### PROGRAM TO RESTORE THE CSD (FORTRAN)

```
C*****  
C* DRIVER PGM, SIMULATION OF CLD FOR A CRYSTAL OF A KNOWN SIZE LMAX  
C*****  
C*INPUT VARIABLES: LMAX SIZE OF CRYSTAL, PMAX, NMAX STEP SIZE, N NUMBER  
C*OF ITERATION FOR THE MONTE CARLO SIMULATION  
C*COMPUTED VARIABLES: ALPHA, BETA, GAMMA1 ROTATION ANGLES, B ROTATION  
C*MATRICE AND C ITS INVERSE, HEIGHT, WEIGHTEDCLD, TOT  
C*OUTPUT: PROBA CLD CORRESPONDING TO A POPULATION OF SIZE LMAX  
C*****
```

C DEFINITION OF VARIABLES, PARAMETERS, INITIALIZATION

```
DOUBLE PRECISION LMAX, PI, PHI1, PHI2, PSI1, PSI2, THETA1  
DOUBLE PRECISION TOT, KK, S, HEIGHT, A0, THETA2, MM, NN  
INTEGER N, PMAX, NMAX, K, I, J, M, R, UPMAX, UP  
PARAMETER (PMAX=20, NMAX=20, N=5000)  
PARAMETER (LMAX=1.166, PI=3.141593)  
DOUBLE PRECISION PROBA(91)  
DOUBLE PRECISION COUNTS(91)  
DOUBLE PRECISION LSOL(1000)  
DOUBLE PRECISION U1(5000)  
DOUBLE PRECISION U2(5000)  
DOUBLE PRECISION U3(5000)  
DOUBLE PRECISION C(3,3)  
DOUBLE PRECISION WEIGHTEDCLD (5000,91)  
DOUBLE PRECISION Z(NMAX)  
DOUBLE PRECISION Y(PMAX)  
DOUBLE PRECISION CHANNEL(91)  
DATA CHANNEL/1, 1.08, 1.166, 1.259, 1.359, 1.468, 1.585, 1.711, 1.848,  
*1.995, 2.154, 2.326, 2.512, 2.712, 2.929, 3.162, 3.415, 3.687, 3.981,  
*4.299, 4.642, 5.012, 5.412, 5.843, 6.31, 6.813, 7.356, 7.943, 8.577, 9.261,  
*10, 10.798, 11.659, 12.589, 13.594, 14.678, 15.849, 17.113, 18.478,  
*19.953, 21.544, 23.263, 25.119, 27.123, 29.286, 31.623, 34.145, 36.  
*869, 39.811, 42.987, 46.416, 50.119, 54.117, 58.434, 63.096, 68.129, 73.  
*564, 79.433, 85.77, 92.612, 100, 107.978, 116.591, 125.893, 135.936,  
*146.78, 158.489, 171.133, 184.785, 199.526, 215.443, 232.631, 251.189,  
*271.227, 292.864,  
*316.228, 341.455, 368.695, 398.107, 429.866, 464.159, 501.187, 541.17  
*, 584.341, 630.957, 681.292, 735.642, 794.328, 857.696, 926.119, 1000/  
DOUBLE PRECISION ALPHA(5000)  
DATA ALPHA/5000*0/  
DOUBLE PRECISION BETA(5000)  
DATA BETA/5000*0/  
DOUBLE PRECISION GAMMA1(5000)  
DATA GAMMA1/5000*0/  
DOUBLE PRECISION B(3,3)  
DATA B/9*0/  
DOUBLE PRECISION X(2)
```

```

C OPEN FILE FOR THE RESULTS
  OPEN(7,FILE='RESULTS.TXT')

CDEFINITION OF Y AND Z ACCORDING TO THE STEP SIZE
  A0=LMAX/2

  DO I=1,PMAX
  Y(I)=-LMAX/2+(I-1)*LMAX/PMAX
  ENDDO

  DO I=1,NMAX
  Z(I)=-LMAX/2+(I-1)*LMAX/NMAX
  ENDDO

C  DEF RANDOM ANGLE ROTATION
  DO I=1,N
  U1(I)=GRND()
  ALPHA(I)=2*PI*U1(I)
  ENDDO
  DO I=1,N
  U2(I)=GRND()
  BETA(I)=PI*U2(I)
  ENDDO
  DO I=1,N
  U3(I)=GRND()
  GAMMA1(I)=2*PI*U3(I)
  ENDDO

C DEF MATRICE ROTATION ET RESOLUTION EQUATION,START OF MONTE CARLO
SIMULATION
  TOT=0
  DO I=1,N
  PSI1=COS(GAMMA1(I))
  PSI2=SIN(GAMMA1(I))
  THETA1=COS(BETA(I))
  THETA2=SIN(BETA(I))
  PHI1=COS(ALPHA(I))
  PHI2=SIN(ALPHA(I))
  B(1,1)=THETA1*PSI1
  B(1,2)=-PSI2*PHI1+PSI1*PHI2*THETA2
  B(1,3)=PSI2*PHI2+PSI1*PHI1*THETA2
  B(2,1)=THETA1*PSI2
  B(2,2)=PSI1*PHI1+PSI2*PHI2*THETA2
  B(2,3)=-PSI1*PHI2+PSI2*PHI1*THETA2
  B(3,1)=-THETA2
  B(3,2)=PHI2*THETA1
  B(3,3)=PHI1*THETA1
  CALL INVERSEM(B,C)

C CALCUL OF THE PROJECTED HEIGHT OF THE CRYSTAL
  HEIGHT=2*A0*MAX(ABS(B(2,3)),ABS(B(2,1)),ABS(B(2,2)))
  UP=0
  DO M=1,PMAX
C INITIALIZATION
  X(1)=3000
  X(2)=3000

```

```

MM=-LMAX
NN=LMAX

C RESOLUTION EQUATION, CALCUL OF CHORD LENGTH
DO R=1,NMAX
CALL SOLVEEQ(LMAX,PMAX,NMAX,C,Y,M,R,Z,X)
MM=MAX(X(1),X(2),MM)
NN=MIN(X(1),X(2),NN)
ENDDO
IF (ABS(MM)<=(A0+1E-7).AND.ABS(NN)<=(A0+1E-7)) THEN
UP=UP+1
LSOL(UP)=ABS(MM-NN)
ENDIF
ENDDO
UPMAX=UP

C CLASSIFICATION OF CHORD LENGTHS INTO BINS
DO J=1,91
KK=0
DO P=1,UPMAX
IF (CHANNEL(J)<LSOL(P) .AND. LSOL(P)<=CHANNEL(J+1))THEN
KK=KK+1
ENDIF
ENDDO
COUNTS(J)=KK
ENDDO

C WEIGHTING OF THE CLDS CALCULATED
C AVERAGE OVER THE 5000 ORIENTATIONS
DO K=1,91
WEIGHTEDCLD(I,K)=(COUNTS(K)/UPMAX)*HEIGHT
ENDDO
TOTHTOTHT=TOTHT+HEIGHT
ENDDO
DO I=1,91
S=0
DO J=1,N
S=S+WEIGHTEDCLD(J,I)
ENDDO
PROBA(I)=S/TOTHT
ENDDO

C NORMALIZATION OF THE RESULTING CLD
S=0
DO I=1,91
S=S+PROBA(I)
ENDDO
DO I=1,91
PROBA(I)=PROBA(I)/S

C WRITE THE RESULT IN FILE
WRITE(7,701) PROBA(I)
ENDDO
701 FORMAT(F12.10)

C PRINT RESULT ON SCREEN
PRINT *,PROBA
STOP
END

```

```

C*****
C* SUBROUTINE INVERSEM
C*****
C* INPUT ROTATION MATRIX B
C*OUTPUT INVERSE C
C*****
  SUBROUTINE INVERSEM (B,C)
C  DEF VARIABLE
  INTEGER I,J
  DOUBLE PRECISION B(3,3)
  DOUBLE PRECISION I1(3,3)
  DOUBLE PRECISION I2(3,3)
  DOUBLE PRECISION C(3,3)
  DOUBLE PRECISION DET
C CALCUL DETERMINANT OF MATRIX
  DET=B(1,1)*(B(2,2)*B(3,3)-B(2,3)*B(3,2))-B(1,2)*(B(2,1)*B(3,3)
    *-B(2,3)*B(3,1))+B(1,3)*(B(2,1)*B(3,2)-B(2,2)*B(3,1))
C CALCUL INVERSE
  C(1,1)=(B(2,2)*B(3,3)-B(2,3)*B(3,2))/(DET)
  C(1,2)=(B(1,3)*B(3,2)-B(3,3)*B(1,2))/(DET)
  C(1,3)=(B(1,2)*B(2,3)-B(2,2)*B(1,3))/(DET)
  C(2,1)=(B(2,3)*B(3,1)-B(3,3)*B(2,1))/(DET)
  C(2,2)=(B(1,1)*B(3,3)-B(3,1)*B(1,3))/(DET)
  C(2,3)=(B(1,3)*B(2,1)-B(2,3)*B(1,1))/(DET)
  C(3,1)=(B(2,1)*B(3,2)-B(3,1)*B(2,2))/(DET)
  C(3,2)=(B(1,2)*B(3,1)-B(3,2)*B(1,1))/(DET)
  C(3,3)=(B(1,1)*B(2,2)-B(1,2)*B(2,1))/(DET)
  RETURN
  END

C*****
C* SUBROUTINE SOLVEEQ
C*****
C* INPUT Y,Z,LMAX,C COEFFICIENTS OF THE EQUATION
C* COMPUTED A1,A2,A3,A0,SOL
C* OUTPUT SOLUTION X
C*****
  SUBROUTINE SOLVEEQ(LMAX, PMAX, NMAX, C, Y, M, R, Z, X, J)
C* DEF VARIABLES
  INTEGER J, I, M, R, PMAX, NMAX
  DOUBLE PRECISION C(3,3)
  DOUBLE PRECISION LMAX, A1, A2, A3, A0
  DOUBLE PRECISION Y(PMAX)
  DOUBLE PRECISION Z(NMAX)
  DOUBLE PRECISION X(2)
  DOUBLE PRECISION SOL(8)
  DATA SOL/8*0/

C CALCUL CONSTANT
  A0=LMAX/2
  A1=-(C(1,2)*Y(M)+C(1,3)*Z(R))/C(1,1)
  A2=-(C(2,2)*Y(M)+C(2,3)*Z(R))/C(2,1)
  A3=-(C(3,2)*Y(M)+C(3,3)*Z(R))/C(3,1)

C CALCUL OF ALL POSSIBLE SOLUTIONS (EQUATION WITHOUT ABS VALUE)

```

$$\text{SOL}(1) = (A0 + (\text{ABS}(C(1,1)) * A1 + \text{ABS}(C(2,1)) * A2 + \text{ABS}(C(3,1)) * A3)) / (\text{ABS}(C(1,1)) + \text{ABS}(C(2,1)) + \text{ABS}(C(3,1)))$$

$$\text{SOL}(2) = (A0 + (\text{ABS}(C(1,1)) * A1 + \text{ABS}(C(2,1)) * A2 - \text{ABS}(C(3,1)) * A3)) / (\text{ABS}(C(1,1)) + \text{ABS}(C(2,1)) - \text{ABS}(C(3,1)))$$

$$\text{SOL}(3) = (A0 + (\text{ABS}(C(1,1)) * A1 - \text{ABS}(C(2,1)) * A2 - \text{ABS}(C(3,1)) * A3)) / (\text{ABS}(C(1,1)) - \text{ABS}(C(2,1)) - \text{ABS}(C(3,1)))$$

$$\text{SOL}(4) = (A0 + (\text{ABS}(C(1,1)) * A1 - \text{ABS}(C(2,1)) * A2 + \text{ABS}(C(3,1)) * A3)) / (\text{ABS}(C(1,1)) - \text{ABS}(C(2,1)) + \text{ABS}(C(3,1)))$$

$$\text{SOL}(5) = (A0 + (-\text{ABS}(C(1,1)) * A1 + \text{ABS}(C(2,1)) * A2 - \text{ABS}(C(3,1)) * A3)) / (-\text{ABS}(C(1,1)) + \text{ABS}(C(2,1)) - \text{ABS}(C(3,1)))$$

$$\text{SOL}(6) = (A0 + (-\text{ABS}(C(1,1)) * A1 + \text{ABS}(C(2,1)) * A2 + \text{ABS}(C(3,1)) * A3)) / (-\text{ABS}(C(1,1)) + \text{ABS}(C(2,1)) + \text{ABS}(C(3,1)))$$

$$\text{SOL}(7) = (A0 + (-\text{ABS}(C(1,1)) * A1 - \text{ABS}(C(2,1)) * A2 - \text{ABS}(C(3,1)) * A3)) / (-\text{ABS}(C(1,1)) - \text{ABS}(C(2,1)) - \text{ABS}(C(3,1)))$$

$$\text{SOL}(8) = (A0 + (-\text{ABS}(C(1,1)) * A1 - \text{ABS}(C(2,1)) * A2 + \text{ABS}(C(3,1)) * A3)) / (-\text{ABS}(C(1,1)) - \text{ABS}(C(2,1)) + \text{ABS}(C(3,1)))$$

C NARROW THE SOLUTIONS TO 0-1-2 DEPENDING ON INTERVAL

```

J=0
IF (SOL(1))>=(MAX(-A0,A1,A2,A3)-1E-7).AND.SOL(1)<=(A0+1E-7) THEN
J=J+1
X(J)=SOL(1)
ENDIF
IF (SOL(2))>=(MAX(-A0,A1,A2)-1E-7).AND.SOL(2)<=(MIN(A0,A3)+1E-7) THEN
J=J+1
X(J)=SOL(2)
ENDIF
IF (SOL(3))>=(MAX(-A0,A1)-1E-7).AND.SOL(3)<=(MIN(A0,A2,A3)+1E-7) THEN
J=J+1
X(J)=SOL(3)
ENDIF
IF (SOL(4))>=(MAX(-A0,A1,A3)-1E-7).AND.SOL(4)<=(MIN(A0,A2)+1E-7) THEN
J=J+1
X(J)=SOL(4)
ENDIF
IF (SOL(5))>=(MAX(-A0,A2)-1E-7).AND.SOL(5)<=(MIN(A0,A1,A3)+1E-7) THEN
J=J+1
X(J)=SOL(5)
ENDIF
IF (SOL(6))>=(MAX(-A0,A2,A3)-1E-7).AND.SOL(6)<=(MIN(A0,A1)+1E-7) THEN
J=J+1
X(J)=SOL(6)
ENDIF
IF (SOL(7))>=(-A0-1E-7).AND.SOL(7)<=(MIN(A0,A1,A2,A3)+1E-7) THEN
J=J+1
X(J)=SOL(7)
ENDIF
IF (SOL(8))>=(MAX(-A0,A3)-1E-7).AND.SOL(8)<=(MIN(A0,A1,A2)+1E-7) THEN
J=J+1
X(J)=SOL(8)
ENDIF

RETURN
END

```

## REFERENCES

- 1 - Abbas, A.; Nobbs, D.; Romagnoli, J. A., "Investigation of on-line optical particle Characterization in reaction, and cooling crystallization systems. Current state of the art", *Measurement Science & Technology*, **2002**, 13, (3), 349-356.
- 2 - Al-Zoubi, N.; Kachrimanis, K.; Malamataris, S., "Effects of harvesting and cooling on crystallization and transformation of orthorhombic paracetamol in ethanolic solution", *European Journal of Pharmaceutical Sciences* **2002**, 17, (1-2), 13-21.
- 3 - Al-Zoubi, N.; Malamataris, S., "Effects of initial concentration and seeding procedure on crystallization of orthorhombic paracetamol from ethanolic solution", *International Journal of Pharmaceutics* **2003**, 260, (1), 123-135.
- 4 - Am Ende, D. J.; Crawford, T. C.; Weston, N. P., "Reactive Crystallization Method to Improve Particle Size". 6,558,435, **2003**.
- 5 - Artioli, G.; Viterbo, D.; Ferraris, G.; Giacomazzo, C.; Giacomazzo, C., "Fundamentals of Crystallography", Oxford University Press, 2nd Bk&Cdr edition, **2002**
- 6 - Barrett, P.; Glennon, B., "In-line FBRM monitoring of particle size in dilute agitated suspensions", *part. part. Syst. Charact.*, **1999**, 16, 207-211
- 7 - Barrett, P.; Glennon, B., "Characterizing the metastable zone width and solubility curve using Lasentec FBRM and PVM", *Chemical Engineering Research & Design*, **2002**, 80, (A7), 799-805.
- 8 - Barrett, P.; Glennon, B.; O'Sullivan, B., "In *Solubility Curve and Metastable Zone Width using Lasentec FBRM & PVM*", Lasentec Users Forum, Charleston, SC, **2002**.
- 9 - Bennett, M. K.; Rohani, S., "Solution of population balance equations with a new combined Lax-Wendroff/Crank-Nicholson method", *chemical engineering science*, **2001**, 56, 6623-6633
- 10 - Bennett, R. C., "Crystallizer selection and design", *Handbook of Industrial Crystallization*, Myerson, A. S., Ed. Butterworth-Heinemann: Boston, **2002**.
- 11 - Beyer, T.; Day, G.M.; Price, S.L., "The prediction, morphology, and mechanical properties of the polymorphs of paracetamol", *Journal of American Chemical Society*, **2001**, 123, (21), 5086-5094.
- 12 - Braatz, R. D., "Advanced control of crystallization processes", *annual reviews in control*, **2002**, 26, 87-99
- 13 - Braun, B.; Groen, H.; Tschernjaew, J., "Production-scale particle design of a pharmaceutical intermediate", *crystal growth & design*, **2004**, 4, (5), 915-920

- 14 - Bravi, M.; Di Cave, S.; Mazzarotta, B.; Verdone, N., "Relating the attrition behavior of crystals in a stirred vessel to their mechanical properties", *chemical engineering journal*, **2003**, 94, 223-229
- 15 - Chen, W.; Liu, D.; Zhang, C.; Wu, L.; Xie, A., "Larger Ba(NO<sub>3</sub>)<sub>2</sub>/Sr(NO<sub>3</sub>)<sub>2</sub> crystal growth and solubility determination", *materials research bulletin*, **2004**, 39, 309-316
- 16 - Choong, K. L.; Smith, R., "Novel strategies for optimization of batch, semi-batch and heating/cooling evaporative crystallization", *chemical engineering science*, **2004**, 59, 329-343
- 17 - Corriou, J.R.; Rohani, S., "Nonlinear control of a batch crystallizer", *chem. Eng. Comm.*, **2002**, 189, 1415-1436
- 18 - Davey, R.; Garside, J., *from molecules to crystallizers*. Oxford University Press: Oxford, **2000**.
- 19 - Doki, N.; Seki, H.; Takano, K.; Asatani, H.; Yokota, M.; Kubota, N., "Process Control of Seeded Batch Cooling Crystallization of the Metastable  $\alpha$ -Form Glycine Using an In-Situ ATR-FTIR Spectrometer and an In-Situ FBRM Particle Counter", *crystal growth & design*, **2004**, 4, (5), 949-953
- 20 - Eek, R.A.; Pouw, H.A.A.; Bosgra, O.H., "Design and experimental evaluation of stabilizing feedback controllers for continuous crystallizers", *Powder technology*, **1995**, 82, 21-35
- 21 - Fachaux, J.M.; Guyot-Hermann, A.M.; Guyot, J.C.; Conflant, P.; Drache, M.; Veessler, S.; Boistelle R., "Pure paracetamol for direct compression - Part I. Development of sintered-like crystals of paracetamol", *Powder technology*, **1995**, 82, 123-128
- 22 - Fachaux, J.M.; Guyot-Hermann, A.M.; Guyot, J.C.; Conflant, P.; Drache, M.; Veessler, S.; Boistelle R., "Pure paracetamol for direct compression - Part II. Study of the physicochemical and mechanical properties of sintered-like crystals of paracetamol", *Powder technology*, **1995**, 82, 129-133
- 23 - Févotte, G., "New perspectives for the on-line monitoring of pharmaceutical crystallization processes using in situ infrared spectroscopy", *international journal of pharmaceuticals*, **2002**, 241, (2), 263-278
- 24 - Fujiwara, M.; Chow, P. S.; Ma, D. L.; Braatz, R. D., "Paracetamol crystallization using laser backscattering and ATR-FTIR spectroscopy: Metastability, agglomeration, and control", *Crystal Growth & Design*, **2002**, 2, (5), 363-370.
- 25 - Garside, J., "Fundamentals of industrial crystallization", *industrial crystallization*, **1984**, 1-6
- 26 - Georgieva, P.; Meireles, M. J.; Feyer de Azevedo, S., "Knowledge-based hybrid modeling of a batch crystallization when accounting for nucleation, growth and agglomeration phenomena", *chemical engineering science*, **2003**, 58, 3699-3713

- 27 - Gerstlauer, A.; Motz, S.; Mitrović, A.; Gilles, E. D., "Development, analysis and validation of population models for continuous and batch crystallizers", *chemical engineering science*, **2002**, 57, 4311-4327
- 28 - Gille, W., "Chord length distributions of infinitely long geometric figures", *Powder technology*, **2002**, 123, 292-298
- 29 - Granberg, R. A.; Rasmuson, A. C., "Solubility of paracetamol in pure solvents", *Journal of Chemical and Engineering Data*, **1999**, 44, (6), 1391-1395.
- 30 - Greenberg, E. F., FDA wants more 'current' good manufacturing practices. *Packaging Digest* **2002**, 39, (10), 28-29.
- 31 - Heath, A.R.; Fawell, P.D.; Bahri, P.A.; Swift, J.D., "Estimating average particle size by focused beam reflectance measurement (FBRM)", *part. part. Syst. Charact.*, **2002**, 19, 84-95
- 32 - Holden, A.; Singer, P.; *Crystals and Crystal Growing*, Anchor Books-Doubleday, New York, **1960**
- 33 - Jančić, S. J.; De Jong, E.J., *Industrial Crystallization*, Elsevier science publishers B.V., Amsterdam, **1984**
- 34 - Jones, A.G.; Chianese, A.; Mullin, J.W., "Effect of fines destruction on batch cooling crystallization of potassium sulfate solutions", *industrial crystallization*, **1984**, 191-195
- 35 - Kashchiev, D., *Nucleation: basic theory with applications*. Butterworth Heinemann: Oxford; Boston, **2000**.
- 36 - Kind, M.; Nieken, U., "On the dynamic simulation of mass crystallization with fines removal", *chemical engineering and processing*, **1995**, 34, 323-328
- 37 - Kubota, N.; Takahashi, H., "A possibility of crystal size distribution control using additives in batch cooling crystallization", *ind. Eng. Chem. Res.*, **1987**, 26,(9), 1936-1939
- 38 - Laudise, R. A.; *The Growth of Single Crystals*, Solid State Physical Electronics Series, Nick Holonyak, Jr. Editor, Prentice-Hall, Inc., **1970**
- 39 - Leubner, I. H., "Balanced nucleation and growth model for controlled crystal size distribution", *journal of dispersion science and technology*, **2002**, 23, (4), 577-590
- 40 - Lewiner, F.; Févotte, G.; Klein, J. P.; Puel, F., "An online strategy to increase the average crystal size during organic batch cooling crystallization", *Ind. Eng. Chem. Res.*, **2002**, 41, (5), 1321-1328
- 41 - Li, M.; Wilkinson, D., "Determination of non-spherical particle size distribution from chord length measurements. Part I: Theoretical analysis", *Chemical Engineering Science*, **2005**, 60, 3251-3265

- 42 - Li, M.; Wilkinson, D.; Patchigolla, K., "Determination of non-spherical particle size distribution from chord length measurements. Part II: Experimental validation", *Chemical Engineering Science*, **2005**, 60, 3251-3265
- 43 - Liotta, V., *Automated Metastable Zones*, Lasentec Users Forum, Barcelona, Spain, **2001**.
- 44 - Liu, C. L.; Hao, H.; Sako, H., "Confidence transformation for combining classifiers", *pattern analysis and applications*, **2004**, 7, (1), 2-17
- 45 - Madras, G.; McCoy, B. J., "Temperature effects for crystal growth: a distribution kinetics approach", *acta materialia*, **2003**, 51, 2031-2040
- 46 - Matz, G., "Crystallization processes", *industrial crystallization*, **1984**, 103-108
- 47 - McPherson, A., "Introduction to Macromolecular Crystallography", Publisher: Wiley-Liss, **2002**.
- 48 - Mersmann, A.; Braun, B.; Löffelmann, M., "Prediction of crystallization coefficients of the population balance", *chemical engineering science*, **2002**, 57, 4267-4275
- 49 - Midler, J. M.; Paul, E. L.; Whittington, E. F.; Futran, M.; Liu, P. D.; Hsu, J.; Pan, S.H., "Crystallization method to improve crystal structure and size". 5,314,506, **1994**.
- 50 - Mingzhong, L.; Wilkinson, D., "Determination of non-spherical particle size distribution from chord length measurements. Part 1: Theoretical analysis", *chemical engineering science*, **2005**, 60, 3251-3265
- 51 - Monnier, O.; Févotte, G.; Hoff, C.; Klein, J. P., "Model identification of batch cooling crystallizations through calorimetry and image analysis", *chemical engineering science*, **1997**, 52, (7), 1125-1139
- 52 - Mullin, J. W., *Crystallization*. 4th ed.; Butterworth-Heinemann: Oxford; Boston, **2001**.
- 53 - Nývlt, J., *Industrial crystallization from solutions*. Butterworth: London, **1971**
- 54 - Nývlt, J.; Söhnel, O.; Matuchová, M.; Broul, M., *The Kinetics of industrial crystallization*. Elsevier Science: Amsterdam; New York, **1985**.
- 55 - Parks, R.M.; Rousseau, R.W., "Experimental feasibility study of CSD control for a KNO<sub>3</sub> crystallizer", *National Conference Publication - Institution of Engineers, Australia*, **1979**, 819-824
- 56 - Qu, H.; Pöllänen, K.; Louhi-Kultanen, M.; Kilpiö, T.; Oinas, P.; Kallas, J., "Batch cooling crystallization study based on in-line measurement of supersaturation and crystal size distribution", *Journal of Crystal Growth*, **2005**, 275, e1857-e1862

- 57 - Randolph, A. D.; Larson, M. A., "Theory of particulate processes", academic press, New York and London, **1971**
- 58 - Randolph, A. D.; Larson, M. A., *Theory of particulate processes: analysis and techniques of continuous crystallization*. 2nd ed.; Academic Press: San Diego, **1988**.
- 59 - Rousseau, RW; Howell TR, "Comparison of simulated crystal size distribution control-systems based on nuclei density and supersaturation", *Industrial & Engineering chemistry process design and development*, **1982**, 21, (4), 606-610
- 60 - Ruf, A.; Worlitschek, J.; Mazzotti, M., "Modeling and experimental analysis of PSD measurements through FBRM". *Particle & Particle Systems Characterization* **2000**, 17, (4), 167-179.
- 61 - Schwartz, A. M.; Myerson, A. S., "Solutions and solution properties", *Handbook of Industrial Crystallization*. Myerson, A. S., Ed. Butterworth-Heinemann: Boston, **2002**.
- 62 - Shan, G.; Igarashi, K.; Noda, H.; Ooshima, H., "Production of large crystals with a narrow crystal size distribution by a novel WWDJ batch crystallizer", *chemical engineering journal*, **2002**, 85, (2-3), 161-167
- 63 - Shi, B.; Rousseau, R.W.; " A method to convert Chord Length Distribution to Particle Size Distribution in Focused Beam Reflectance Measurements", Lasentec Users Forum, Orlando, FL, **2000**
- 64 - Shi, B. "Crystallization of solutes that lead to scale formation in black liquor evaporation", *Doctoral Thesis*, Georgia Institute of Technology, Atlanta, GA, **2002**.
- 65 - Shimizu, K.; Nomura, T.; Takashashi, K., "Crystal size distribution of aluminum potassium sulfate in a batch crystallizer equipped with different types of impeller", *journal of crystal growth*, **1998**, 191, 178-184
- 66 - Sutradhar, B. C.; Randolph, A. D., "Design charts for the fines- dissolving crystallizer", *ind. Eng. Chem. Res.*, **1993**, 32, (11), 2781-2788
- 67 - Tavare, N. S., *Industrial crystallization: process simulation analysis and design*. Plenum Press: New York, **1995**.
- 68 - Vanderhallen, F.; Deriemaeker, L.; Manderick, B.; Finsy, R., "Shape and size determination by laser diffraction: parametric density estimation by neural networks", *part. part. Syst. charact.*, **2002**, 19, 65-72
- 69 - West, R. M.; Cullivan, J. C.; Williams, R. A., "Estimation of particle-size distribution and classifier selectivity", *part. part. Syst. charact.*, **2000**, 17, 139-145
- 70 - White, E. T.; Randolph, A. D., "Optimum fines size for classification in double draw-off crystallizers", *ind. Eng. Chem. Res.*, **1989**, 28, (3), 276-284

- 71 - Worlitschek, J.; Mazzotti, M., "Model-based optimization of particle size distribution in batch-cooling crystallization of paracetamol", *Crystal Growth & Design*, **2004**, 4, (5), 891-903.
- 72 - Wynn, E. J. W., "Relationship between particle-size and chord-length distributions in focused beam reflectance measurement: stability of direct inversion and weighting", *Powder Technology*, **2003**, 133, (1-3), 125-133.
- 73 - Žekić, A. A.; Mitrović, M. M., "Dependence of growth rate on initial crystal size", *journal of crystal growth*, **2003**, 258, 204-210
- 74 - Zelmanov, G.; Semiat, R., "Particle-size analysis in mass crystallization from solutions", *AIChE journal*, **2000**, 46, (7), 1376-1383
- 75 - Zipp, G. L.; Randolph, A. D., "Selective fines destruction in batch crystallization", *ind. Eng. Chem. Res.*, **1989**, 28, (9), 1446-1448